

2011

## Self-assembly and Photophysics of Selected Organic Materials and Two-photon Bioimaging with Profluorescent Nitroxides, Polyelectrolyte Nanoparticles, and Squaraine Probes

Hyo Yang Ahn  
*University of Central Florida*

 Part of the [Chemistry Commons](#)

Find similar works at: <https://stars.library.ucf.edu/etd>

University of Central Florida Libraries <http://library.ucf.edu>

This Doctoral Dissertation (Open Access) is brought to you for free and open access by STARS. It has been accepted for inclusion in Electronic Theses and Dissertations by an authorized administrator of STARS. For more information, please contact [STARS@ucf.edu](mailto:STARS@ucf.edu).

---

### STARS Citation

Ahn, Hyo Yang, "Self-assembly and Photophysics of Selected Organic Materials and Two-photon Bioimaging with Profluorescent Nitroxides, Polyelectrolyte Nanoparticles, and Squaraine Probes" (2011). *Electronic Theses and Dissertations*. 6651.  
<https://stars.library.ucf.edu/etd/6651>

SELF-ASSEMBLY AND PHOTOPHYSICS OF SELECTED ORGANIC MATERIALS AND  
TWO-PHOTON BIOIMAGING WITH PROFLUORESCENT NITROXIDES,  
POLYELECTROLYTE NANOPARTICLES, AND SQUARINE PROBES

by

HYO-YANG AHN

B.S, SeoKyeong University, Seoul, Korea, 2000

M.S. YonSei Univierisity, Seoul, Korea, 2002

A dissertation submitted in partial fulfillment of the requirements  
for the degree of Doctor of Philosophy  
in the Department of Chemistry  
in the College of Sciences  
at the University of Central Florida  
Orlando, Florida

Summer Term  
2011

Major Professor: Kevin D. Belfield

©2011 Hyo-Yang Ahn

## ABSTRACT

Two-photon absorption and upconverted fluorescence has been utilized in a variety of applications in pure science and engineering. Multiphoton-based techniques were used in this research in order to understand photophysical and chemical characteristics of several fluorescent dyes and to demonstrate some of their key applications.

Two-photon fluorescence microscopy (2PFM) has become a powerful technique in biophotonics for non-invasive imaging in the near-infrared (NIR) region (700~1000 nm) that often results in less photobleaching. In Chapter 1, there is a brief introduction to fluorescence, examples of fluorescence materials, and a discussion of the advantages of two-photon absorption. 2PFM imaging was utilized in Chapters 2 to 4 for various applications.

In Chapter 2, a new squaraine dye is introduced and its linear and nonlinear photophysical properties are characterized. This compound has very high two-photon absorption (2PA) cross sections and high photostability both in an organic solvent and when encapsulated in micelles. Based on these properties, this dye was demonstrated as a near-infrared (NIR) probe in *in vitro* 2PFM imaging with excitation over 800 nm wavelength.

In Chapter 3, new profluorescent nitroxides are introduced. Nitroxide radicals are utilized for electron paramagnetic resonance (EPR) spectroscopy and in biological systems as some are known, in some manner, to mimic the behavior of superoxide dismutase (SOD) that detoxifies or mitigates oxidative stress by trapping free radicals. Here, two profluorescent nitroxides investigated for use as a two-photon fluorescent oxidative stress indicator in *in vitro* two-photon fluorescence microscopy (2PFM) imaging.

In Chapter 4, two-photon excited (2PE) fluorescence of a conjugated polyelectrolyte (CPE), PPESO<sub>3</sub>, was studied in methanol and in water. The results of CPE quenching studies were comparable under both one-photon excitation conditions and two-photon excitation. CPE coated silica nanoparticles were incubated in HeLa cells and 2PFM imaging was demonstrated for this new class of fluorescent probe.

Supramolecular structures based on organized assemblies/aggregation of chromophores have attracted widespread interest as molecular devices with potential applications in molecular electronics, artificial light harvesting, and pharmacology. In Chapter 5, J-aggregate formation was investigated for two porphyrin-based dyes, 5,10,15,20-tetrakis(4-sulfonatophenyl)porphyrin (TPPS, **4**) and an amino tris-sulfonate analog (**5**) in water via UV-vis, fluorescence, and lifetime decay studies. The effect of aggregation on two-photon absorption properties was also investigated. A functionalized norbornene-based homopolymer, synthesized by the ring opening metathesis polymerization technique was used as a J-aggregation enhancement template and had a role of polymer-templating to facilitate porphyrin aggregation and modulate 2PA.

In Chapter 6, squaraine dye aggregates templated with single wall carbon nanotubes (SWCNTs) that were atomically clean were studied by using optical absorption spectroscopy, atomic force microscopy (AFM), and photoconductivity measurements. SWCNTs selectively promote the formation of squaraine dye aggregates with a head-to-head stacking arrangement, and these dye aggregates effectively photosensitize SWCNTs, demonstrating that this novel approach can yield highly photosensitized devices.

Special thanks to my mother, Young-Ja Hong, and grandma, Kum-Ryeh Kim

## ACKNOWLEDGMENTS

During four years at UCF towards this point of my academic career, it is very difficult to list all the people who have helped me along the way. First, I would like to express my sincere thanks to Dr. Kevin D. Belfield for providing endless support, constant encouragement, guidance, and optimism over the past four years of my studies. Your passion and enthusiasm guided to me a world of knowledge in fields such as photochemistry, biophotonics, linear and nonlinear characterization, and microfabrication. You also showed me how to focus and dedicate time to my work to allow me to finish this dissertation. I am deeply grateful that I had many opportunities with you during my research work to collaborate with great scholars such as Dr. Kirk Schanze at University of Florida, Dr. Steven Bottle at Queensland University of Technology in Australia, Dr. Kevin Burgess at Texas A&M University, Dr. Masa Ishigami at University of Central Florida, and Dr. Chris Collison at Rochester Institute of Technology. Above all, these experiences made me an independent, developed researcher. Thank you so much from the bottom of my heart, Dr. Belfield.

I deeply appreciate my dissertation committee members: Dr. Delbert Howard Miles, Dr. Robert Igarashi, Dr. Masa Ishigami, and Dr. Andrew Frazer, who have been generous with their time and support. Thank you so much.

I would also like to thank my individual group members (Dr. Belfield's research group) for supporting, inspiring, mentoring me, and making the work environment friendly, calm, and enjoyable like a family: Dr. Mykhailo Bondar, Dr. Alma Morales, Dr. Andrew (Andy) Frazer, Dr. Sheng Yao, Dr. Dao Nguyen, Dr. Sanchita Biswas, Dr. Xuhua Wang, Dr. Lifu Zhang, Dr. Ciceron Yanez, Dr. Carolina Andrade, Bosung Kim, Gheorghe Luchita, Qinglong Ziang,

Yuanwei Zhang, Bill Moreshead, Adam Woodward, Xiling Yue, Mengyuen Wang, Jin Yu, Mohamed Daudi, Yezabel Colon Gomez, Rosemary Victoria, and Casey Haugen. You guys are all AWESOME and I wish you the best.

Also, I am grateful to all my friends at UCF and in Korea. I can't name everybody here, but I hope that my gratitude reaches every individual. Thank you for your support and well wishes.

Finally, most importantly, I would like to thank my family, dad and my 'only' bro Jae. Without your support and love, I wouldn't be here writing this. I sincerely appreciate God for assigning you in my life as my dad and my brother. I love you both so much and thank you for your support in making this happen. And, to my recently extended family, thank you all for your support, especially, mom. Lastly, Todd who is my half, my light, my life. I can't say more than thanks to you for your support and love. I hope that you know all my gratefulness and feel all my love (finally, we can be together~ hopefully happily ever after). I thank you and love you so much.

Love you all!!!

Hyo-Yang Ahn

## TABLE OF CONTENTS

LIST OF FIGURES .....	xii
LIST OF TABLES .....	xviii
LIST OF SCHEMES.....	xix
LIST OF ACRONYMS / ABBREVIATIONS .....	xx
CHAPTER 1: INTRODUCTION .....	1
1-1. Background and Significance.....	1
1-2. Dissertation Statement.....	5
1-3. Dissertation Outline.....	6
CHAPTER 2: NEAR-INFRARED EMITTING SQUARINE DYES WITH HIGH 2PA CROSS SECTIONS FOR MULTIPHOTON FLUORESCENCE IMAGING .....	7
2-1. Abstract.....	7
2-2. Introduction .....	8
2-3. Experimental Materials and Methods.....	10
Synthesis .....	10
Methods.....	12
2-4. Results and Discussion .....	16
2-5. Conclusions .....	31
References .....	32

## CHAPTER 3: PROFLUORESCENT NITROXIDES: LINEAR AND NONLINEAR

### PHYTOPHYSICAL CHARACTERIZATION AND USE FOR OXIDATIVE STRESS PROBE

.....	36
3-1. Abstract.....	36
3-2. Introduction .....	37
3-3. Experimental Materials and Methods.....	38
Synthesis .....	38
Methods.....	38
Cell Assay .....	40
3-4. Results and discussion .....	43
Linear Photophysical Properties .....	43
Nonlinear Optical Properties.....	48
Cytotoxicity.....	52
1PFM and 2PFM Images .....	54
3-5. Conclusion .....	60
References .....	61

## CHAPTER 4: TWO-PHOTON EXCITED FLUORESCENCE OF A CONJUGATED



### POLYELECTROLYTE AND ITS APPLICATION IN CELL IMAGING .....

4-1. Abstract.....	65
4-2. Introduction .....	65

4-3. Experimental Materials and Methods.....	67
Materials. ....	67
Methods.....	67
4-4. Results and Discussion .....	68
4-5. Conclusion .....	76
References.....	76
CHAPTER 5: ENHANCEMENT OF J-AGGREGATION OF POLYMER-TEMPLATED SELF ASSEMBLED PORPHYRIN-BASED DYES .....	80
5-1. Abstract.....	80
5-2. Introduction .....	81
5-3. Experimental Materials and Methods.....	84
Materials .....	84
Synthesis .....	84
Methods.....	86
5-4. Results and discussion.....	87
5-5. Conclusion .....	102
References.....	102
CHAPTER 6: PHOTSENSITIZATION OF CARBON NANOTUES USING DYE AGGREGATES.....	105
6-1. Abstract.....	105

6-2. Introduction .....	105
6-3. Experimental Materials and Methods.....	107
Synthesis .....	107
6-4. Results and discussion .....	107
6-5. Conclusion .....	112
References .....	112
CHAPTER 7: CONCLUSIONS .....	118
APPENDIX A: PUBLICATIONS TO DATE FROM DISSERTATION WORK.....	120
APPENDIX B: SUPPORTING INFORMATION OF CHAPTER 2 .....	123
APPENDIX C: SUPPORTING INFORMATION OF CHAPTER 3 .....	137
APPENDIX D: SUPPORTING INFORMATION OF CHAPTER 4.....	149
APPENDIX E: SUPPORTING INFORMATION OF CHAPTER 5 .....	156
APPENDIX F: SUPPORTING INFORMATION OF CHAPTER 6 .....	161

## LIST OF FIGURES

<b>Figure 1.</b> Jablonski diagram ( <a href="http://web.uvic.ca/ail/techniques/epi-fluorescence.html">http://web.uvic.ca/ail/techniques/epi-fluorescence.html</a> ) .....	1
<b>Figure 2.</b> Linear and non-linear optical spectra of dye <b>1</b> (1 GM (Göppert Meyer) = $10^{-50}$ cm <sup>4</sup> s/photon <sup>-1</sup> , uncertainty of the 2PA value = 15 % ).....	21
<b>Figure 3.</b> Linear and nonlinear optical spectra of squaraine <b>2</b> (1 GM (Göppert Meyer) = 10-50 cm <sup>4</sup> s/photon <sup>-1</sup> , uncertainty of the 2PA value = 15 % ).....	23
<b>Figure 4.</b> Kinetic changes in the absorption spectra of corresponding dyes by excited at 650 nm argon degas of micelles (a) Cy 5, (b) dye <b>1</b> , (c) dye <b>2</b> , and (d) the percentage of the absorption comparison over three dyes.....	25
<b>Figure 5.</b> Cell Viable test in  HCT 116 and  COS 7 of (a) squaraine <b>1</b> and (b) squaraine <b>2</b> (error bar = $\pm 7$ %). .....	28
<b>Figure 6.</b> HCT 116 of 20 $\mu$ M squaraine <b>1</b> (a) DIC, (b) 1PA image with Fluo out (Ex 377/50, DM 409, Em 525/40), (c) 1PA image with Cy 5 filter (Ex 630/50, DM 660, Em 690/40), (d) 1PA overlaid fluorescence image, (e) 1PA overlaid image (a) to (c) (scale bar = 10 $\mu$ m). .....	29
<b>Figure 7.</b> HCT 116 of 20 $\mu$ M squaraine <b>2</b> (a) DIC, (b) 1PA image with Fluo out (Ex 377/50, DM 409, Em 525/40), (c) 1PA image with Cy 5 filter (Ex 630/50, DM 660, Em 690/40), (d) 1PA overlaid fluorescence image, (e) 1PA overlaid image (a) to (c) (scale bar = 10 $\mu$ m). .....	29
<b>Figure 8.</b> COS 7 of 20 $\mu$ M squaraine <b>1</b> (a) DIC, (b) 1PA image with Fluo out (Ex 377/50, DM 409, Em 525/40), (c) 1PA image with Cy 5 filter (Ex 630/50, DM 660, Em 690/40), (d)	

1PA overlaid fluorescence image, (e) 1PA overlaid image (a) to (c) (scale bar = 10 $\mu$ m).	30
.....	
<b>Figure 9</b> COS 7 of 20 $\mu$ M squaraine <b>2</b> (a) DIC, (b) 1PA image with Fluo out (Ex 377/50, DM 409, Em 525/40), (c) 1PA image with Cy 5 filter (Ex 630/50, DM 660, Em 690/40), (d) 1PA overlaid fluorescence image, (e) 1PA overlaid image (a) to (c) (scale bar = 10 $\mu$ m).	30
.....	
<b>Figure 10.</b> HCT 116 images of squaraine <b>1</b> (a) DIC, (b) 2PFM (c) 2PFM 3D reconstruction, and HCT 116 images of squaraine <b>2</b> (a) DIC, (b) 2PFM (c) 2PFM 3D reconstruction (scale bar = 10 $\mu$ m).	31
.....	
<b>Figure 11.</b> Fluorescence lifetime setup (1) 100% reflection mirror, (2) beam splitter, (3) spectrometer, (4) neutral density filter, (5) APD beam trigger, (6) Glan-Thomson polarizer, (7) focusing lens, (8) sample holder, and (9) broad band-pass filter.	39
.....	
<b>Figure 12.</b> Two-photon absorption (2PA) induced fluorescence setup, (1) 100% reflection mirror, (2) focusing mirror, (3) pin hole, (4) Glan-Thomson polarizer, and (5) half wave plate.	40
.....	
<b>Figure 13.</b> Possible reactions of nitroxides in biological systems. <sup>1</sup>	48
.....	
<b>Figure 14.</b> Linear and nonlinear optical spectra of (a) compound <b>20</b> and (b) <b>4BM-66</b> . In each graph, the absorption spectrum is a black line, the emission spectrum is a blue line, anisotropy is green, and two-photon absorption (2PA) cross section showed as half-filled red circle, respectively.	51
.....	
<b>Figure 15.</b> Cell viability evaluation as a function of H <sub>2</sub> O <sub>2</sub> concentration.	52
.....	
<b>Figure 16.</b> Comparative cell viability of (a) nitroxide <b>19</b> , <b>19</b> + 100 $\mu$ M of H <sub>2</sub> O <sub>2</sub> , and NOME analog <b>20</b> , and (b) nitroxide <b>47</b> , <b>47</b> + 100 $\mu$ M of H <sub>2</sub> O <sub>2</sub> , and NOME analog <b>66</b> .	54
.....	

<b>Figure 17.</b> 1PFM image using nitroxide <b>19</b> and CHO cells (a) control (0 $\mu\text{M}$ of <b>19</b> and 0 $\mu\text{M}$ $\text{H}_2\text{O}_2$ ), (b) 5 $\mu\text{M}$ of <b>19</b> , (c) 10 $\mu\text{M}$ of <b>19</b> , (d) 5 $\mu\text{M}$ <b>19</b> + 100 $\mu\text{M}$ of $\text{H}_2\text{O}_2$ , (e) 5 $\mu\text{M}$ of <b>19</b> + 200 $\mu\text{M}$ of $\text{H}_2\text{O}_2$ , (f) 10 $\mu\text{M}$ of <b>19</b> + 100 $\mu\text{M}$ of $\text{H}_2\text{O}_2$ , (g) 10 $\mu\text{M}$ of <b>19</b> + 200 $\mu\text{M}$ of $\text{H}_2\text{O}_2$ . .....	56
<b>Figure 18.</b> 1PFM imaging with nitroxide <b>47</b> and CHO cells (a) control (0 $\mu\text{M}$ of <b>19</b> and 0 $\mu\text{M}$ $\text{H}_2\text{O}_2$ ), (b) 5 $\mu\text{M}$ of <b>47</b> , (c) 10 $\mu\text{M}$ of <b>47</b> , (d) 5 $\mu\text{M}$ of <b>47</b> + 100 $\mu\text{M}$ of $\text{H}_2\text{O}_2$ , (e) 5 $\mu\text{M}$ of <b>47</b> + 200 $\mu\text{M}$ of $\text{H}_2\text{O}_2$ , (f) 10 $\mu\text{M}$ of <b>47</b> + 100 $\mu\text{M}$ of $\text{H}_2\text{O}_2$ , (g) 10 $\mu\text{M}$ of <b>47</b> + 200 $\mu\text{M}$ $\text{H}_2\text{O}_2$ . .....	57
<b>Figure 19.</b> Colocalization study in CHO cells using probe <b>19</b> with commercial oxidative stress probe CelROX Deep Red (NOR analogs of <b>19</b> : Ex. 458 nm/Em. 500–600 nm, CellROX Deep Red: Ex. 561/Em. 580-650 nm), (a) DIC, (b) cells incubated with 10 $\mu\text{M}$ of <b>19</b> , (c) cells then incubated with 5 $\mu\text{M}$ of CellROX Deep Red, and (d) overlaid images of (a), (b), and (c). .....	58
<b>Figure 20.</b> Colocalization study of nitroxide <b>47</b> in CHO cells with commercial oxidative stress probe CellROX Deep Red (Sample: Ex. 458 nm /Em. 500–600 nm, CellROX Deep Red: Ex. 561/Em. 580-650 nm), (a) DIC, (b) incubated with 20 $\mu\text{M}$ of <b>47</b> , (c) then incubated with 5 $\mu\text{M}$ of CellROX Deep Red, and (d) overlaid image of (a), (b), and (c). .....	59
<b>Figure 21.</b> 2PFM images with fs excitation at 900 nm of CHO cells incubated with 10 $\mu\text{M}$ of <b>19</b> and 200 $\mu\text{M}$ $\text{H}_2\text{O}_2$ of (a) DIC, (b) one 2PFM XY optical slice, (c) 2PFM 3D reconstructed image, with 20 $\mu\text{M}$ of <b>47</b> and 200 $\mu\text{M}$ $\text{H}_2\text{O}_2$ (d) DIC, (e) one 2PFM XY optical slice, (f) and (g) 2PFM 3D reconstructed image. ....	60

<b>Figure 22.</b> Linear and two-photon photophysical properties of PPESO <sub>3</sub> polymer in methanol (Normalized absorption spectrum (green line), normalized emission spectrum (red line), and 2PA spectrum (blue line and circle symbol)).....	70
<b>Figure 23.</b> Fluorescence spectra of 10 $\mu$ M PPESO <sub>3</sub> in varying proportions of methanol and water at (a) $\lambda_{\text{ex}} = 740$ nm and (b) $\lambda_{\text{ex}} = 380$ nm (bottom). ....	72
<b>Figure 24.</b> Fluorescence quenching of PPESO <sub>3</sub> (10 $\mu$ M in methanol) by DODC [0.1 – 10 $\mu$ M] at (a) $\lambda_{\text{ex}} = 740$ nm and (b) $\lambda_{\text{ex}} = 380$ nm.....	74
<b>Figure 25.</b> Images of HeLa cells incubated with PPESO <sub>3</sub> silica nanoparticle (20 $\mu$ g/mL, 2 h). (a) DIC, exposure time 20 ms, (b) 1PFM image, 130 ms (filter cube Ex: 377/50 DM: 409 Em: 525/40), and (c) one layer of 2PFM image (Ex: 750 nm; Power: 30 mW). ....	75
<b>Figure 26.</b> (a) UV-vis absorption spectra of ( <b>4</b> ) solution (black line is <b>4</b> in water, red is <b>4</b> in acidic condition (0.2 M HCl), green is <b>4</b> in pH 1 buffer, and blue is <b>4</b> templated with polymer in pH 1 buffer); (b) formation of J-aggregates of ( <b>4</b> ) at different pH (HCl/KCl aqueous buffer). ....	90
<b>Figure 27.</b> (a) Kinetic study of J-band of <b>4</b> at pH 1.0 at different time intervals (a 1.0 cm path length cuvette cell was used with ( <b>4</b> = 40 $\mu$ M) at room temperature), (b) Formation of stable J-aggregates of <b>4</b> in the presence of polymer <b>3</b> in aqueous buffer (pH = 1.0) at different time intervals. ....	91
<b>Figure 28.</b> UV-vis absorption spectra of <b>5</b> (a) at different pH in HCl/KCl aqueous buffer and formation of J- aggregates of <b>5</b> , (b) in presence of polymer <b>3</b> at pH 1.0 (HCl/KCl buffer), (c) dependence of J-aggregation on concentration of <b>5</b> without polymer; (d) J-aggregation	

as a function of varying concentration of <b>5</b> in presence of polymer <b>3</b> . All experiments are done with $[4] = 10^{-5}$ M in 1 cm cuvette at room temperature. ....	93
<b>Figure 29.</b> Steady state fluorescence spectra of (a) <b>4</b> (black line is <b>4</b> in water, red is <b>4</b> in acidic condition (0.2 M HCl), orange is <b>4</b> in pH 1 buffer, and blue is <b>4</b> templated with polymer in pH 1 buffer) and (b) <b>5</b> (black line is <b>5</b> in water, red is <b>5</b> in acidic condition (0.2 M HCl), green is <b>5</b> in pH 1 buffer, and blue is <b>5</b> templated with polymer in pH 1 buffer).....	95
<b>Figure 30.</b> Fluorescence decays of TPPS monomer <b>4</b> (free base in water (a) and dianion in 0.2 M HCl (b)) and a J-aggregated species without (c) or with polymer (d) templates (both in pH 1), measured with time correlated singlephoton counting methods (compared with Instrument response function (IRF) in each case). ....	96
<b>Figure 31.</b> Fluorescence decays of monomer <b>5</b> (free base in water and dianion in 0.2 M HCl (a)) an J-aggregated species without or with polymer (b) templates, measured with time correlated singlephoton counting methods (compared with Instrument response function (IRF) in each case). ....	98
<b>Figure 32.</b> Z scan experiment setup, (1) 100% reflection mirrors, (2) focusing lens, (3) pinhole, (4) neutral density filter, and (5) beam splitter. ....	100
<b>Figure 33.</b> Normalized absorption spectra and 2PA cross sections of <b>4</b> in water, TPPS in pH 1 solution, and <b>4</b> with polymer in pH 1 solution. <b>4</b> (black line is the absorption spectrum of <b>4</b> in water, blue line is the absorption spectrum of <b>4</b> in pH 1 buffer solution, red line is the absorption spectrum of <b>4</b> templated with polymer in pH 1 buffer, black half-filled square dots are nonlinear optical spectrum of <b>4</b> in water, blue half-filled circle dots are nonlinear optical spectrum of <b>4</b> in pH 1 buffer solution, and red half-filled triangle dots are nonlinear optical spectrum of <b>4</b> templated with polymer in pH 1 buffer). ....	101

<b>Figure 34.</b> (a Optical absorption spectrum of SQ44OH in DCE (1 % by weight). (b) Optical absorption spectra of a nanotube network on quartz (red), SQ44OH on quartz (green) and SQ44OH on a nanotube network (blue).....	110
--	-----

<b>Figure 35.</b> $5 \times 5 \mu\text{m}^2$ AFM images of (a) SQ44OH on quartz, (b) SQ44OH on nanotubes, and (c) as-grown nanotubes. ....	111
--	-----

## LIST OF TABLES

<b>Table 1.</b> Example of fluorophores along with their absorption and emission maximum wavelengths and the observed fluorescence color (abcam.com). .....	3
<b>Table 2.</b> Linear photophysical property data for dye <b>1</b> , <b>2</b> , and Cy 5 in different solvents.....	19
<b>Table 3.</b> Photochemical decomposition quantum yields ( $\eta$ ) and figure of merits ( $F_M$ ) of dye <b>1</b> and <b>2</b> in DMSO and micelles encapsulated dye.....	27
<b>Table 4.</b> Linear photophysical properties of the nitroxide and NOME derivatives.....	47
<b>Table 5.</b> Photophysical properties of the TPPS ( <b>4</b> , free base and dianion) and related J-aggregations with or without polymer templates.....	97
<b>Table 6.</b> Photophysical properties of the <b>5</b> (free base and anion) and related J-aggregations with or without polymer templates. ....	98

## LIST OF SCHEMES

<b>Scheme 1.</b> Synthesis of squaraine dye <b>1</b> .....	16
<b>Scheme 2.</b> Molecular structures of nitroxide and NOME derivatives. ....	46
<b>Scheme 3.</b> Chemical structures of CPEs and quenchers .....	69
<b>Scheme 4.</b> Synthesis of monomers and homopolymer.....	87
<b>Scheme 5.</b> Scheme for dye aggregation with the polymeric template. ....	89
<b>Scheme 6.</b> Molecular structure of SQ44OH.....	107

## LIST OF ACRONYMS / ABBREVIATIONS

ACN	Acetonitrile
ATCC	America Type Culture Collections
AFM	Atomic force microscopy
APD	Avalanche photodiode detector
DODC	Cationic cyanine dye energy transfer quencher
(MV2+)	Cationic electron transfer quencher methylviologen
CHO	Chinese hamster ovary
CPE	Conjugated polyelectrolyte
$\chi^2$	Correlation coefficient
CDC <sub>13</sub>	Deuterated chloroform
CHX	Cyclohexane
DCM	1, 2-dichloromethane
DCE	1,2-dichloroethane
DM	Dichroic mirror
DIC	Differential interference contrast
DSC	Differential scanning calorimetry

DMSO	Dimethyl Sulfoxide
EPR	Electron paramagnetic resonance
Em	Emission
Ex	Excitation
fs	Femtosecond ( $10^{-15}$ s)
metMb	Ferric myoglobin
$F_M$	Figure of merit
$\tau$	Fluorescence lifetime
$\phi_{FL}$	Fluorescence quantum yield
FTIR	Fourier transform infrared
FWHM	Full width at half maximum
GPC	Gel permeation chromatography
GM	Goppert-Mayer unit for the 2PA cross-section ( $1 \times 10^{-50} \text{ cm}^4 \text{ s photon}^{-1} \text{ molecule}^{-1}$ )
HR-MS	High resolution mass spectrometry
$\lambda_{\text{max}}^{\text{Abs}}$	Maxima of absorption
$\lambda_{\text{max}}^{\text{Em}}$	Maxima of fluorescence
MeOH	Methanol

μL	Microliter ( $10^{-6}$ L)
μm	Micrometer ( $10^{-6}$ m)
μW	Microwatt ( $10^{-6}$ W)
μM	Micromolarity ( $10^{-6}$ M)
mL	Milliliter ( $10^{-3}$ L)
mM	Millimolarity ( $10^{-3}$ M)
ε	Molar absorptivity coefficient
nm	Nanometer ( $10^{-9}$ m)
NOMe	Nitroxide methoxy
NMR	Nuclear magnetic resonance
NIR	Near-infrared
1PA	One-photon absorption
1PFM	One-photon fluorescence microscopy
OD	Optical density
η	Photochemical decomposition quantum yield
PDT	Photodynamic therapy
PMT	Photomultiplier tube

ROMP	Ring opening metathesis polymerization
PDDA	Poly(dimethyldiallylammonium)chloride
PEG	Polyethylene glycol
rpm	Rotation per minute
SEM	Scanning electron microscopy
SWNTs	Single wall carbon nanotubes
SQ	Squaraine
cm <sup>2</sup>	Square centimeter
PPESO <sub>3</sub>	Sulfonated poly( <i>para</i> -phenylene ethynylene)
SV	Stern-Volmer
SOD	Superoxide dismutase
TPPS	5,10,15,20-tetrakis(4-sulfonatophenyl)porphyrin
THF	Tetrahydrofuran
Td	Thermal decomposition temperature
TGA	Thermogravimetric analysis
3D	Three dimensions
TEM	Transmission electron microscopy

TNT	Trinitrotoluene
2PA	Two-photon absorption
2PE	Two-photon excitation
2PFM	Two-photon fluorescence microscopy
$\delta_{2PA}$	Two-photon absorption cross-section
UV-vis	Ultraviolet -Visible
$\lambda_{\max}$	Wavelength of absorption maxima
wt%	Weight percent

## CHAPTER 1: INTRODUCTION

### 1-1. Background and Significance

Luminescence has been fascinating people for centuries by natural phenomena such as jellyfish, Arizona bark scorpions, red and white wheat, and so on. An early described observation of fluorescence was in 1565 by Nicolás Monardes in the infusion of a certain type of wood (*Lignum nephriticum*). The principle of luminescence is that when an electron of a molecule is excited from ground state to higher level energy states by light or heat, it goes down to ground state again by emitting the light energy, called a photon.

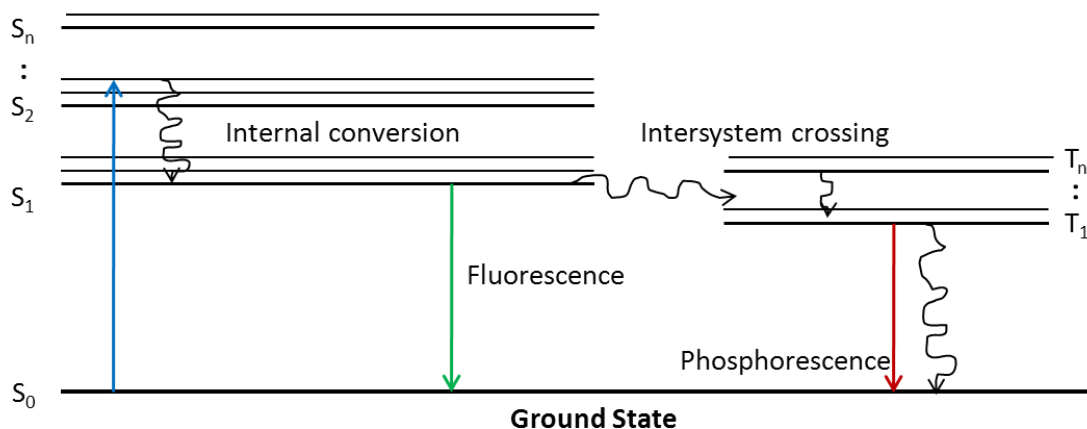


**Figure 1.** Jablonski diagram (<http://web.uvic.ca/ail/techniques/epi-fluorescence.html>)

The Jablonski diagram illustrates the electronic states of a molecule and the transitions between them as shown in Figure 1. State  $S_0$  is called the singlet ground state of the fluorophore

(fluorescent molecule) and higher singlet excited states are  $S_1$ ,  $S_2$ , and  $S_3$ . A molecule in its higher excited state,  $S_2$  or  $S_3$ , can undergo relaxation to  $S_1$  by “non-radiative relaxation” in which the excitation energy is dissipated as heat. When the electron relaxes from  $S_1$  to  $S_0$ , it can emit light (fluorescence) or relax nonradiatively. Transitions between electronic states of the same spin multiplicity ( $S_1 \rightarrow S_0$ ) are allowed. Transitions between states with different spin multiplicity ( $S_1 \rightarrow T_1$ ) are formally forbidden, but may occur due to a process called spin-orbit coupling (intersystem crossing). When the electron relaxes from  $T_1$  to  $S_0$ , a secondary radiative relaxation may occur called phosphorescence. These processes are very important to understanding luminescent phenomena and including that found in nature.

Early applications of fluorescence were fluorescent lamps, fluorescence analysis, and fluorescent tracers. With more discoveries of natural fluorescent materials and the new development of fluorescent materials, fluorescence techniques were explored for many practical applications, including mineralogy, gemology, physics, chemistry, and biology. In particular, the use of fluorescent materials in biological applications has provided a versatile, and nearly indispensable toolset due to great sensitivity and selectivity (see in Table 1). In addition, the absorption and emission of fluorescent materials can be tuned since absorption and emission are based on their structures and environment. The sophisticated manipulation of synthetic methods has progressed to a level where hundreds of light-emitting molecules have been commercialized. For example, fluorescein derivatives have an absorption max of ca. 480 nm and an emission max of ca. 520 nm, and, depending on the  $\pi$ - $\pi$  conjugated system, the absorption max can be shorter or longer, and the Stokes shifts lesser or greater.

**Table 1.** Example of fluorophores along with their absorption and emission maximum wavelengths and the observed fluorescence color (abcam.com).

Dye	Absorbance wavelength	Emission Wavelength	Visible color
Hydroxycoumarin	352	386	Blue
Methoxycoumarin	360	410	Blue
Alexa fluor	345	442	Blue
Aminocoumarin	350	445	Blue
Cy 2	490	510	Green (dark)
FAM	495	516	Green (dark)
Fluorescein FITC	495	518	Green (light)
Alexa fluor 532	530	555	Green (light)
HEX	535	556	Green (light)
Cy 3	550	570	Yellow
TRITC	547	572	Yellow
Alexa fluor 546	556	573	Yellow
Rhodamine Red-X	560	580	Orange
Tamara	565	580	Red
Rox	575	602	Red
Alexa fluor 568	578	603	Red
Texas Red	615	615	Red
Cy 5	650	670	Red
TruRed	675	695	Red
Cy 7	743	770	Red

However, many fluorescent materials undergo photobleaching upon irradiation (typically in the ultraviolet or visible range), causing them to lose their ability to fluoresce. This means that molecules accumulate chemical damage during photoexcitation. During imaging, cells are also susceptible to phototoxicity. Furthermore fluorescent molecules have a tendency to generate

reactive chemical species under illumination that enhances the so-called phototoxic effect. Two-photon absorption (2PA) is often desirable because of its advantage to overcome some existing shortcomings of one-photon absorption. 2PA takes place when a molecule absorbs two photons simultaneously (often these are near-IR photons). The molecule absorbs enough energy to be raised into an excited state but the relaxation procedure is essentially the same as 1PA, though the initial excited state may vary. The main difference of 2PA over 1PA is the dependence of the rate of formation of excited state molecules on the incident light intensity; 2PA exhibits a quadratic dependence with the incident excitation, while 1PA exhibits a linear relationship to the incident light intensity. 2PA often employs near-infrared (NIR) excitation wavelengths, typically in the 700 and 1000 nm range, for practical reasons, although it may occur at any wavelength, depending on the molecule. This excitation range is known as an “optical window” as it coincides particularly well with the decreasing absorption of biological materials at in this wavelength range. This nonlinearity of absorption often affords less photobleaching, reduced phototoxicity, a highly localized focal spot, and deeper penetration, in bioimaging. These characteristics provided compelling motivation in this study to find fluorescent compounds that possess enhanced optical nonlinearities for advancing the utility of 2PA processes in the biological sciences. Here, a new squaraine dye, profluorescent nitroxides, and a conjugated polyelectrolyte (CPE), PPESO<sub>3</sub>, were characterized by 2PA and their potential application in two-photon fluorescence microscopy (2PFM) bioimaging.

Certain dye molecules aggregate in solution or at a solid interface under various conditions, sometimes resulting in narrow and sharp absorption bands compared to unaggregated monomers. This is referred to as aggregation or, more recently, supramolecular assembly. J-

aggregates have side-by-side molecular arrangements, resulting in a red-shifted absorption band. Meanwhile, H-aggregates have head-to-head molecular arrangements, affording a blue shifted absorption band (J-Aggregates, T Kobayashi, 1996). These occurrences are appealing in molecular devices in a number of technologies such as molecular optical switches, micro or nano electronic devices, artificial light harvesting, and communication, since the absorptivity can be modulated via aggregation. Herein, porphyrin and squaraine derivatives were studied for aggregation enhancement with a polymer template and a single wall carbon nanotubes template, respectively. 2PA characterization of supramolecular porphyrin J-aggregates was conducted to determine if molecular aggregation, and in the case of H- and J-aggregates, intermolecular electron delocation can form a more polarizable system and lead to increased 2PA.

## **1-2. Dissertation Statement**

The purpose of this dissertation is to illustrate many advantages using two-photon absorption and fluorescence methods with  $\pi$ -conjugated chromophores for nonlinear applications.  $\pi$ -Conjugated organic derivatives are in high demand in various fields to “visualize” desirable objects and attempt to mark higher brightness, and also control the absorption and emission tuning ability. When the absorbed radiation is in the ultraviolet (UV) and visible range, there are limitations such as photobleaching of fluorescent probes due to their high energy and restricted penetration depth due to their linear dependence for incident light. Simultaneous 2PA is proportional to the square of the incident light intensity. Therefore, 2PA occurs at a highly localized optical spatial focal spot, where there is sufficiently high photon density. This intrinsic property of 2PA leads to numerous applications. The benefit of using organic materials is the

high probability of manipulating the desirable structures and properties of a molecule. Here, several different types of fluorophores were utilized and characterized by two-photon excitation. These molecules sometimes formed particles, micelles, or aggregates, depending on the material and application. Biophotonics and optoelectronics were the main focus of applications.

### **1-3. Dissertation Outline**

This work is structured as follows: The introduction of fluorescence and two-photon absorption is in Chapter 1. In Chapter 2, a new squaraine dye is presented, and its linear and nonlinear photophysical properties were characterized. The use of this new dye as a NIR fluorescent probe in 2PFM was demonstrated. Ten pairs of profluorescent nitroxides were introduced in Chapter 3 along with comprehensive linear photophysical characterization and 2PA measurements. Two promising compounds were chosen for use as a two-photon fluorescent oxidative stress indicator in conventional and 2PFM imaging. In Chapter 4, one- and two-photon absorption-induced fluorescence quenching properties of a conjugated polyelectrolyte (CPE), PPESO<sub>3</sub>, in methanol and in water was conducted to better understand the properties and behavior of this interesting class of materials. The utility of the CPE as a fluorescent probe in 2PFM cell imaging was demonstrated.

For optoelectronic approaches, templated aggregation enhancement was addressed. In Chapter 5, a functionalized norbornene-based homopolymer was introduced to template J-aggregation of two porphyrin-based dyes, 5,10,15,20-tetrakis(4-sulfonatophenyl)porphyrin (TPPS, **4**) and an amino tris-sulfonate analog (**5**). In Chapter 6, squaraine dye aggregates templated with single wall carbon nanotubes (SWCNTs) were investigated.

## CHAPTER 2: NEAR-INFRARED EMITTING SQUARINE DYES WITH HIGH 2PA CROSS SECTIONS FOR MULTIPHOTON FLUORESCENCE IMAGING

### 2-1. Abstract

Designed to achieve high two-photon absorptivity, a new NIR squaraine dye, (E)-2-(1-(2-(2-methoxyethoxy)ethyl)-5-(3,4,5-trimethoxystyryl)-1H-pyrrol-2-yl)-4-(1-(2-(2-methoxyethoxy)ethyl)-5-(3,4,5-trimethoxystyryl)-2H-pyrrolium-2-ylidene)-3-oxocyclobut-1-enolate (**1**) and (Z)-2-(4-(dibutylamino)-2-hydroxyphenyl)-4-(4-(dibutyliminio)-2-hydroxycyclohexa-2,5-dienylidene)-3-oxocyclobut-1-enolate (**2**) were synthesized and characterized. Their linear photophysical properties were investigated using UV-visible absorption spectroscopy and fluorescence spectroscopy in various solvents while their nonlinear photophysical properties were investigated using a combination of two-photon induced fluorescence and open aperture z-scan methods. Squaraine **1** exhibited a high two-photon absorption (2PA) cross section ( $\delta_{2PA}$ ),  $\sim 20,000$  GM at 800 nm. Squaraine **1** also displayed high photostability with the photochemical decomposition quantum yields one order of magnitude lower than Cy 5, a commercially available pentamethine cyanine NIR dye. The cytotoxicity of the squaraine dyes were evaluated in HCT 116 and COS 7 cell lines to assess the potential of these probes for biomedical applications. The viability of both cell lines was maintained above 80% at dye concentrations up to 30  $\mu$ M, indicating good biocompatibility of the probes. Finally,

one-photon fluorescence microscopy (1PFM) and two-photon fluorescence microscopy (2PFM) cell imaging was demonstrated after incubation with the squaraine probes.

## **2-2. Introduction**

Squaraine dyes were developed in the 1950's<sup>1</sup> and reported in the 1960's.<sup>2</sup> Researchers have been interested in squaraine compounds because of their unique properties that include a relatively narrow absorption band and emission in near-infrared (NIR) range. NIR emitting dyes have great potential for applications in photonics and biomedical fields such as photoconductivity,<sup>3</sup> solar energy conversion,<sup>4</sup> optical data storage,<sup>5</sup> light emitting field-effect transistors,<sup>6</sup> nonlinear optics,<sup>7</sup> NIR-emitting fluorescent probes,<sup>8</sup> and sensitizers for photodynamic therapy.<sup>9</sup> In biophotonics research, NIR fluorescent dyes are desirable for noninvasive quantization and visualization via optical imaging in the window between 700 nm and 1000 nm range where a number of biological materials have high transparency. This window of wavelength is very critical in order to obtain deeper penetration in tissue with high resolution because most tissues absorb below 700 nm. Additionally, due to the use of lower energy excitation, photobleaching may be reduced with NIR excitation.

For bioimaging, an ideal NIR probe needs to have high photophysical and chemical stability, low toxicity, high fluorescence quantum yield, and insensitivity to intermolecular quenching.<sup>10</sup> Conjugated cyanine dyes have been studied as NIR fluorescent dyes.<sup>9, 11</sup> However, the more  $\pi$ -conjugated a cyanine dye is, generally the less photostable it is.<sup>12</sup> On the other hand, squaraine dyes generally fulfill these conditions as a NIR fluorescence probe.<sup>13</sup> Two-photon absorbing probes can be more applicable as a NIR fluorescent probe regarding NIR range

absorbing capability for noninvasive detection in biological tissues.<sup>1</sup> Also, two-photon fluorescence microscopy (2PFM) imaging can provide better contrast, brighter images, and greater detail relative to conventional or one-photon fluorescence microscopy (1PFM). In combination with a two-photon laser scanning microscope, a suitable squaraine-based probe provides a unique toolset for three-dimensional (3D) bioimaging. Recently, a few of cyanine dyes and squaraine dyes were found to have very high 2PA cross sections.<sup>14</sup> However, their potential as two-photon fluorescence probes has not been fully explored. In this work, a new two-photon absorbing NIR squaraine dye, (E)-2-(1-(2-(2-Methoxyethoxy)ethyl)-5-(3,4,5-trimethoxystyryl)-1H-pyrrol-2-yl)-4-(1-(2-(2-methoxyethoxy)ethyl)-5-(3,4,5-trimethoxystyryl)-2H-pyrrolium-2-ylidene)-3-oxocyclobut-1-enolate (**1**) synthesized, characterized, and its application as a 2PFM probe was evaluated. In addition, (Z)-2-(4-(Dibutylamino)-2-hydroxyphenyl)-4-(4-(dibutyliminio)-2-hydroxycyclohexa-2,5-dienylidene)-3-oxocyclobut-1-enolate (**2**) which showed a high 2PA cross section in our previous work<sup>15</sup> was also evaluated as a 2PFM probe. The commercially available pentamethine cyanine dye, Cy 5, was studied for comparison.

Most squaraine dyes are not soluble in water, a major obstacle for bioimaging, necessitating strategies to enhance their biocompatibility.<sup>10</sup> To address the solubility problem, we utilized an amphiphilic copolymer to form micelle encapsulated squaraine dyes **1** and **2**.

## **2-3. Experimental Materials and Methods**

### **Synthesis**

*General.* All reagents and solvents were used as received from commercial suppliers. Reactions were conducted under N<sub>2</sub> or Ar atmospheres. Melting points are uncorrected. <sup>1</sup>H and <sup>13</sup>C NMR spectra were recorded on a NMR spectrometer at 300 and 75 MHz, respectively. MS analyses were performed at the University of Florida. (Z)-2-(4-(Dibutylamino)-2-hydroxyphenyl)-4-(4-(dibutyliminio)-2-hydroxycyclohexa-2,5-dienylidene)-3-oxocyclobut-1-enolate (**2**) was prepared as reported previously.<sup>15</sup>

**1-(2-(2-Methoxyethoxy)ethyl)-1H-pyrrole-2-carbaldehyde 3.** A mixture of 1H-pyrrole-2-carbaldehyde (0.476 g, 5.0 mmol), KOH (0.28 g, 5.0 mmol), and 18-crown-6 (0.04 g, 0.15 mmol) in C<sub>6</sub>H<sub>6</sub> was refluxed for 2 h, then BrCH<sub>2</sub>CH<sub>2</sub>OCH<sub>2</sub>CH<sub>2</sub>OCH<sub>3</sub> (1.14 g, 6.25 mmol) in C<sub>6</sub>H<sub>6</sub> was added and the mixture was refluxed for 4 h. Upon cooling, water was added and the organic phase was separated, washed with water and dried by MgSO<sub>4</sub>. Concentration and purification by column chromatography using CH<sub>2</sub>Cl<sub>2</sub>/MeOH (100/1) as eluent gave 0.78 g product **3** as a liquid (yield 79%). <sup>1</sup>H NMR (300 MHz, CDCl<sub>3</sub>) δ 9.49 (s, 1H), 7.04 (m, 1H), 6.91 (m, 1H), 6.18 (m, 1H), 4.48 (t, *J* = 6.0 Hz, 2H), 3.73 (t, *J* = 4.5 Hz, 2H), 3.46 (m, 2H), 3.42 (m, 2H), 3.31 (s, 3H). <sup>13</sup>C NMR (75 MHz, CDCl<sub>3</sub>) δ 179.4, 132.8, 125.1, 110.0, 109.5, 71.8, 70.7, 70.5, 59.0, 48.8. HRMS (APCI) theoretical [M+Na]<sup>+</sup> = 220.0944, found [M+Na]<sup>+</sup> = 220.0941.

**1-(2-(2-Methoxyethoxy)ethyl)-2-(3,4,5-trimethoxystyryl)-1H-pyrrole 4.** 5-(Chloromethyl)-1, 2, 3-trimethoxybenzene (0.86 g, 4.0 mmol) was refluxed with triethyl phosphite (1.5 mL) for 2 h, the excess triethyl phosphite was distilled off and the residue was dried under vacuum. The

product was then mixed with compound **3** in dry DMF (3 mL) under Ar. NaH (0.48 g, 20.0 mmol) was added and the mixture was stirred at room temperature for 20 h. The mixture was diluted with water and the product was extracted with ethyl acetate. Purified by column chromatography using ethyl acetate as eluent gave 0.7 g of product **4** (yield 48%) as a liquid.  $^1\text{H}$  NMR (300 MHz,  $\text{CDCl}_3$ )  $\delta$  6.91 (d,  $J = 9.0$  Hz, 1H), 6.82 (d,  $J = 9.0$  Hz, 1H), 6.75 (m, 1H), 6.68 (s, 2H), 6.48 (m, 1H), 6.18 (m, 1H), 4.20 (t,  $J = 4.5$  Hz, 2H), 3.93 (s, 6H), 3.87 (s, 3H), 3.76 ( $J = 4.5$  Hz, 2H), 3.56 (m, 2H), 3.51 (m, 2H), 3.36 (s, 3H).  $^{13}\text{C}$  NMR (75 MHz,  $\text{CDCl}_3$ )  $\delta$  153.4, 137.5, 133.7, 131.6, 123.7, 123.1, 122.9, 108.8, 108.6, 106.7, 106.5, 103.1, 71.9, 71.1, 70.7, 61.0, 59.1, 56.3, 56.1, 46.7. HRMS (APCI) theoretical  $[\text{M}+\text{H}]^+ = 362.1962$ , found  $[\text{M}+\text{H}]^+ = 362.1971$ .

**(E)-2-(1-(2-(2-Methoxyethoxy)ethyl)-5-(3,4,5-trimethoxystyryl)-1H-pyrrol-2-yl)-4-(1-(2-(2-methoxyethoxy)ethyl)-5-(3,4,5-trimethoxystyryl)-2H-pyrrol-2-ylidene)-3-oxocyclobut-1-enolate (1).** Compound **4** (0.70g, 2.00 mmol) and squaric acid (0.11 g, 0.97 mmol) in a BuOH/toluene mixture (2/1 v/v, 60 ml) were refluxed with a Dean-Stark apparatus for 6 h. The precipitated product was collected by filtration giving 0.31 g product **1**. (40% yield) m. p. 203-204 °C.  $^1\text{H}$  NMR (300 MHz,  $\text{CDCl}_3$ )  $\delta$  7.84 (d,  $J = 3.0$  Hz, 1H), 7.24 (d,  $J = 9.0$  Hz, 1H), 7.16 (d,  $J = 9.0$  Hz), 6.89 (d,  $J = 3.0$  Hz, 1H), 6.77 (s, 4H), 4.96 (m, 4H), 3.94 (s, 12H), 3.89 (m, 6H+4H), 3.53 (m, 4H), 3.41 (m, 4H), 3.20 (s, 3H).  $^{13}\text{C}$  NMR (75 MHz,  $\text{CDCl}_3$ )  $\delta$  177.0, 167.2, 153.5, 147.8, 139.2, 135.4, 134.9, 132.1, 129.9, 124.2, 116.2, 115.7, 113.9, 105.0, 104.3, 103.7, 72.08, 71.9, 70.7, 61.1, 58.8, 56.3, 56.2, 47.1. HRMS (ESI-TOF) theoretical  $[\text{M}+\text{Na}]^+ = 823.3412$ , found  $[\text{M}+\text{Na}]^+ = 823.3356$ .

## Methods

### Linear optical property studies

Steady-state linear absorption was measured with an Agilent 8453 UV-vis spectrophotometer. Fluorescence emission and fluorescence excitation spectra were measured using a PTI Quantamaster Spectrofluorimeter equipped with a Hamamatsu R928 photomultiplier tube (PMT) in solvents of varying polarity. Fluorescence quantum yields were determined by relative fluorescence emission comparison with cresyl violet as a reference. Excitation anisotropy spectra were measured using a PTI Quantamaster Spectrofluorimeter coupled with two Thomson polarizers for an L-format method in high viscosity solvent (glycerol, Acros) to avoid reorientation, and in low concentration solutions ( $C \sim 10^{-6}$  M) to avoid reabsorption.<sup>16</sup>

Lifetime measurement were performed using a tunable Ti:sapphire laser system (Coherent Verdi-V10 and MIRA 900, pulse duration  $\sim 200$  fs/pulse (FWHM), and repetition rate 76 MHz). The polarization of the excitation beam was linear and oriented by the magic angle to avoid molecular reorientation effects.<sup>17</sup> A broad band-pass filter (FF01-694/SP-25, Semrock) was placed in front of the avalanche photodiode detector (APD, PicoQuant GmbH, LSM\_SPAD). Data was acquired with a PicoQuant time-correlated single photon counting system, PicoHarp300.

The optical density of all the solutions did not exceed 0.12 at the excitation wavelength to avoid reabsorption. Measurements were conducted in 10 mm path length quartz cuvettes at room temperature. Linear photophysical properties of squaraines **1** and **2** were measured in acetonitrile (ACN), 1, 2-dichloromethane (DCM), dimethyl sulfoxide (DMSO), methanol

(MeOH), tetrahydrofuran (THF), and micelles that encapsulated the squaraine dye. All solvents were spectroscopic grade.

#### Nonlinear optical property studies

The open aperture Z-scan method was performed using linear polarized excitation from a Clark-MXR, CPA2010, Ti:sapphire amplified system followed by an optical parametric generator/amplifier (model TOPAS 4/ 800, Light Conversion) providing laser pulses of 140 fs (FWHM) duration with 1 kHz repetition rate.<sup>18</sup> The tuning range was 520–2100 nm while  $10^{-3}\text{M} \leq C \leq 10^{-2}\text{M}$  concentration solutions were used in a 1 mm quartz cuvette at room temperature between 780 and 860 nm. In case of squaraine **1**, the same laser system coupled with a PTI Quantamaster Spectrofluorimeter was used for two-photon absorption (2PA) spectrum measurements of upconverted fluorescence under two-photon excitation over a broad spectral region from 840 nm to 1140 nm with  $10^{-5}\text{M} \leq C \leq 10^{-3}\text{M}$  concentration DMSO solution in a 10 mm quartz cuvette at room temperature.<sup>16</sup> The 2PA spectrum of squaraine **1** was calibrated with ZnSe as a standard of spectral region from 780 nm to 860nm.

#### Photo- and thermo-stability

The photochemical stability was evaluated for squaraines **1**, **2**, and Cy 5 (DiD oil, D 307, Invitrogen, Carlsbad, CA 92008) in DMSO and aqueous micelle media by irradiating the solution in a 10 mm path length quartz cuvette using a 650 nm diode laser.<sup>19</sup> Irradiation time-dependent absorption spectra were obtained with an Agilent 8453 UV/Vis spectrophotometer and photodecomposition quantum yields were determined.

Thermostability study was conducted by thermogravimetric analysis (TGA, Q 5000 TA Instruments) and differential scanning calorimetry (DSC, Q1000 TA Instruments).

#### Micell encapsulation

In order to make the concentrated micelle stock solution, 1 mg/mL of the dye was prepared by adding a small amount of 1,2-dichloromethane (Acros organics) to dissolve the dye. Water was added with 2 wt% of surfactant (Pluronic F 127 Prill, BASF Corporation) and stirred overnight. The crude solution was filtered before. The concentration of the micelle-encapsulated probe stock solution was determined using the molar absorptivity, dye **1**  $\epsilon_{853} = 0.6 \times 10^5 \text{ M}^{-1} \text{ cm}^{-1}$  and dye **2**  $\epsilon_{601} = 1.0 \times 10^5 \text{ M}^{-1} \text{ cm}^{-1}$ .

#### Cell lines

HCT116 and COS 7 were purchased from America Type Culture Collection (ATCC, Manssas, VA, USA). All cells were incubated at 37 °C in a 95% humidified atmosphere containing 5% CO<sub>2</sub> in cell media (RPMI-1640, Invitrogen, Carlsbad, CA, USA), supplemented with 10% fetal bovine serum (FBS, Atlanta Biologicals, Lawrenceville, GA, USA), and 1% penicillin-streptomycin (Atlanta Biologicals, Lawrenceville, GA, USA). 0.25% Trypsin-EDTA (Invitrogen, Carlsbad, CA, USA) was used for cell splitting.

#### Cytotoxicity Assay

HCT116 and COS 7 were placed in 96 well plates  $3 \times 10^3$  cells per well in 90  $\mu\text{L}$  and waited until it reached  $6 \times 10^3$  cells per well for the cytotoxicity test. The cells were incubated for additional 20 h with dye encapsulated in micelles in different concentrations. Subsequently, 10  $\mu\text{L}$  of CellTiter 96® Aqueous One Solution reagent (MTS assay) was added into each well,

followed by further incubation for 4 h at 37 °C. The relative viability of the cells incubated with dyes to untreated cells was determined by measuring the MTS-formazan absorbance on a microplate reader (Spectra Max M5, Molecular Devices) at 490 nm with subtraction of the absorbance of the cell-free blank volume at 490 nm. The results from the three individual experiments were averaged.

#### Cell culture and Incubation

HCT116 and COS 7 cells were placed onto poly-D-lysine coated glass cover slips (12 mm, #1) in 24-well plates  $3 \times 10^4$  cells per well, and the cells were incubated for 48 h before incubating with the encapsulated dyes. The filtered stock solution was diluted with complete growth medium, RPMI-1640, and then incubated for 1.5 h. 20  $\mu$ L of 5  $\mu$ g/mL Hoechst was with incubation following for another 30 min. After incubation, the cells were washed with PBS (x 5) and fixed using 3.7% formaldehyde solution for 15 min at 37 °C. Then freshly prepared  $\text{NaBH}_4$  (1 mg/mL, prepared by adding a couple of drops of 0.1 M NaOH) solution in PBS (pH = 8.0) was added to each well (0.5 mL/well) for 15 min. The plates were then washed with PBS (x 2) and water (x 1). Finally, the glass cover slips were mounted using Prolong Gold mounting media (Invitrogen) for microscopy.

#### One- and Two-photon Fluorescence Microscopy (1PFM) and (2PFM) Imaging

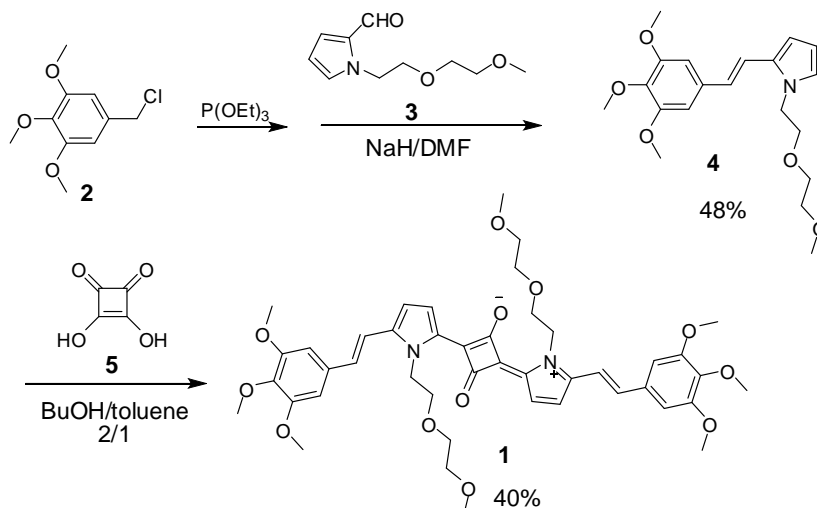
Conventional single-photon fluorescence images were obtained using an inverted microscope (Olympus IX70) equipped with a QImaging cooled CCD (Model Retiga EXi) and mercury lamp 100 W. In order to improve the fluorescence background-to-image ratios, customized filter cubes were used for the one-photon fluorescence images (1PFM). The

specifications of the filter cube were tailored to match the excitation wavelength of the probe, and to capture most of the probe's emission profile.

Two-photon fluorescence microscopic (2PFM) images were obtained with a modified Olympus Fluoview FV300 microscope system combined with a tunable Coherent Mira 900F Ti:sapphire laser, pumped by a 9 W Coherent Verdi 10 frequency doubled Nd:YAG laser. The femtosecond NIR laser beam (with ~200 fs pulse width and 76 MHz repetition rate) was tuned ~850 nm as required and used as the two-photon excitation source. The two-photon induced fluorescence was collected by a 60× microscopic objective (UPlanSApo 60×, NA = 1.35, Olympus). A high-transmittance broad short-pass filter (FF01-694/SP-25, Semrock) was placed in front of the PMT detector of the FV300 scanhead in order to filter out background radiation from the laser source.

## **2-4. Results and Discussion**

**Scheme 1.** Synthesis of squaraine dye **1**.



Squaraine dye **1** was synthesized by condensation of squaric acid with pyrrole intermediate **4** in a 2:1 mixture of butanol and toluene using a Dean-Stark trap to azeotropely remove water (Scheme 1). Intermediate **4** was prepared by Horner-Emmons reaction of 1-(2-(2-Methoxyethoxy)ethyl)-1H-pyrrole-2-carbaldehyde **3** with phosphonated 5-(chloromethyl)-1,2,3-trimethoxybenzene **2** in 48% yield. The dye structure was confirmed by  $^1\text{H}$  NMR,  $^{13}\text{C}$  NMR, and HRMS.

Linear photophysical properties of dye **1** and **2** are shown in Table 2. Cy 5 was characterized in DMSO and encapsulated micelles for comparison purposes as a commercially available NIR dye. Both squaraines **1** and **2** had good solubility in most of the organic solvents used. The absorption and fluorescence emission spectra are narrow and sharp as is the case with a typical squaraine dye peak (see the spectra in SI). Squaraine **1** exhibited absorption maxima in the range from 688 nm to 706 nm and fluorescence emission maxima from 706 nm to 719 nm and squaraine **2** has absorption maxima in the range from 645 to 659 and fluorescence emission maxima from 657 nm to 675 nm in organic solvents. Squaraine **1** showed about 50 nm longer absorption and fluorescence emission maxima than squaraines **2** and even the maxima of Cy 5. Stokes shift is relatively small, up to 18 nm, a common attribute of squaraine dye. After forming dye encapsulated micelles as a consequence of their poor solubility in water, both exhibited a blue shift of about 50 nm from their original maximum peak, as a result of specific  $\pi$ -conjugated formation, so called, *H*-aggregation.<sup>20</sup>

Emission spectra were used for the relative fluorescence quantum yield,  $\Phi_{\text{FL}}$ , calculation. All spectra were corrected by the spectral sensitivity of the PMT. The formula is as follows;

$$\Phi_{FL} = \Phi_R \frac{I}{I_R} \frac{OD_R}{OD} \frac{n^2}{n_R^2} \frac{RP_R}{RP} \quad (1)$$

where the subscript *R* refers to the reference.  $\Phi$  is the quantum yield, *OD* is the optical density, namely, absorption at the exciting wavelength, *n* is the refractive index of the solvent, *RP* is the relative power of the source beam of the fluoremeter of the excitation wavelength. Cresyl violet in methanol was used as a reference ( $\Phi_{FL} = 0.54$ ).<sup>17</sup>  $\Phi_{FL}$  of squaraine **1** and squaraine **2** was a maximum 0.15 and 0.90 in an organic solvent, respectively.  $\Phi_{FL}$  of the dyes in water forming micelles decreased. Generally, fluorescence is significantly reduced in polar solvents such as water. In addition, when dye encapsulated micelles form aggregates, fluorescence quenching typically increases<sup>21</sup>. Generally,  $\Phi_{FL}$  and lifetime are strongly dependent upon each other and correlate well, consistent with our results.<sup>22</sup> Since squaraine **1** had a lower  $\Phi_{FL}$ , it has correspondingly shorter lifetime between 0.16 and 0.51 ns, while the lifetime of squaraine **2** was between 2.3 and 2.5 ns. Both probes exhibited a single exponential fluorescence decay process in the organic solvents studied.

**Table 2.** Linear photophysical property data for dye **1**, **2**, and Cy 5 in different solvents.

<i>Dye</i>	<i>Solvent</i>	<i>Polarity</i>	$\lambda_{max}^{Abs.}$	$\lambda_{max}^{Em.}$	<i>Stokes Shift</i>	$\Phi_{FL}$	$\tau_{FL} (ns) (700nm)$	$\chi^2$	
Dye 1	DCM	1.6	696 ± 1	711 ± 1	15 ± 2	0.07 ± 0.05	0.37 ± 0.07	0.99	
	Aprotic	THF	1.75	699 ± 1	713 ± 1	14 ± 2	0.15 ± 0.03	0.53 ± 0.07	0.99
		ACN	3.92	688 ± 1	705 ± 1	17 ± 2	0.05 ± 0.01	0.24 ± 0.07	0.99
		DMSO	3.96	706 ± 1	719 ± 1	13 ± 2	0.11 ± 0.03	0.51 ± 0.07	0.99
	Protic	MeOH	1.7	688 ± 1	706 ± 1	18 ± 2	0.03 ± 0.02	0.16 ± 0.07	0.99
		Micelle	water 1.85	647 ± 1	656 ± 1	9 ± 2	0.005 ± 0.001	1.8 ± 0.1	0.97
Dye 2	DCM	1.6	648 ± 1	657 ± 1	9 ± 2	0.75 ± 0.05	2.4 ± 0.1	0.99	
	Aprotic	THF	1.75	647 ± 1	657 ± 1	10 ± 2	0.80 ± 0.05	2.4 ± 0.1	0.98
		ACN	3.92	645 ± 1	660 ± 1	15 ± 2	0.75 ± 0.05	2.5 ± 0.1	0.99
		DMSO	3.96	659 ± 1	675 ± 1	16 ± 1	0.62 ± 0.05	2.3 ± 0.1	0.99
	Protic	MeOH	1.7	644 ± 1	658 ± 1	14 ± 2	0.90 ± 0.05	2.3 ± 0.1	0.98
		Micelle	water 1.85	606 ± 1	746 ± 1	40 ± 2	0.004 ± 0.001	2.7 ± 0.1	0.96
Cy 5	Aprotic	DMSO	3.96	651 ± 1	670 ± 1	19 ± 2	0.45 ± 0.05	1.7 ± 0.1	0.99
	Protic	Micelle	water 1.85	650 ± 1	669 ± 1	19 ± 2	0.017 ± 0.005	2.2 ± 0.1 0.61 ± 0.07	0.99

Maxima of absorption,  $\lambda^{Abs}_{max}$ , fluorescence,  $\lambda^{Em}_{max}$ , fluorescence quantum yield,  $\Phi_{FL}$ , lifetimes,  $\tau$ , and correlation coefficient,  $\chi^2$ .

Fluorescence anisotropy spectra were obtained using previously reported methods, using the equation:

$$r = \frac{I_{VV} - GI_{VH}}{I_{VV} + 2GI_{VH}}, \quad (G = \frac{I_{HV}}{I_{HH}}) \quad (2)$$

where  $G$  is a factor that is the ratio of the sensitivities of the detection system for vertically and horizontally polarized light.<sup>20</sup> The subscripts  $V$  and  $H$  refer to vertically and horizontally polarized light, respectively. Excitation anisotropy is correlated with the spectral position of electronic transitions that can be useful to estimate 2PA allowed transitions. The position of the excitation anisotropy is different for different electronic transitions in a fluorescent dye and is based on the estimated angle between the absorption and emission dipole moments.<sup>29</sup> Anisotropy values can theoretically range from -0.2 to +0.4 due to the angles between transition dipole moments.<sup>30</sup> Dye solutions were prepared in glycerol, a solvent with a high viscosity in order to avoid molecular reorientation. The dye was dissolved in methanol at high concentration and one drop was added into glycerol. The plateau above 560 nm in the anisotropy spectrum for dye **1**, as shown in Figure 2, is associated with the high energy electronic transition ( $S_0 \rightarrow S_1$ ) that is a one-photon allowed and, formally, a two-photon forbidden transition. The value of anisotropy decreased from 560 to 510 nm, suggesting a different electronic transition and increased until approximately 470 nm, creating a small valley. A similar trend was observed again from 440 to 350 nm. The specific valley regions, about 520 and 400 nm, respectively, suggest  $S_0 \rightarrow S_n$  electronic transitions that are two-photon allowed transitions. The analysis of the excitation anisotropy electron transitions correlates well with the observed 2PA cross section values. The two minima in the anisotropy spectrum correspond to higher 2PA values than other wavelengths

and the 2PA value at 800 nm (one-photon excitation wavelength of 400 nm) was  $\sim 20,000$  GM, approaching one of the highest values for squaraines reported previously.<sup>18</sup> Even at 1040 nm, a 2PA cross section of 1500 GM was recorded, indicating the potential use of this NIR probe in bioimaging since a large 2PA cross section is currently of considerable interest since the laser power to excite the molecule can be reduced, minimizing photodamage, an aspect that is particularly important for deep tissue penetration and live cell imaging.

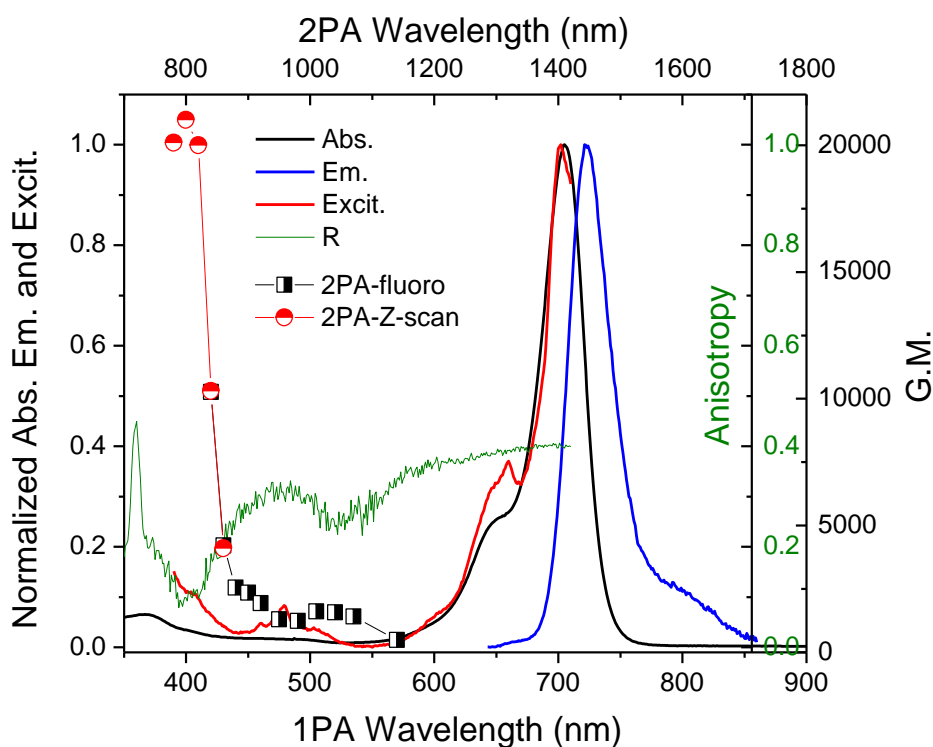


**Figure 2.** Linear and non-linear optical spectra of dye **1** (1 GM (Göppert Meyer) =  $10^{-50}$  cm<sup>4</sup> s/photon<sup>-1</sup>, uncertainty of the 2PA value = 15 %).

Squaraine **2** was investigated and the 2PA cross section value was reported in one of our previous studies<sup>18</sup> (~13,000 GM at 730 nm in acetone). Since the 2PA cross sections of squaraine **1** and Cy 5 were measured in DMSO, we measured the 2PA cross section of squaraine **2** in DMSO as well for comparison. This measurement was performed by using a fs Ti:sapphire laser system (Coherent, Legend seeded by MIRA 900) that pumped an optical parametric amplifier (Coherent, OPerA Solo, FWHM ~ 100 fs, repetition rate = 1 kHz) using a PTI Quantamaster Spectrofluorimeter and a 10 mm quartz cuvette at room temperature. The tuning range was between 760 nm to 1030 nm for this specific measurement, with concentration in the range of  $10^{-5} \text{ M} \leq C \leq 10^{-3} \text{ M}$ . Rhodamine B was used as a reference. The two-photon absorption cross section was calculated as follows;

$$\delta_{2PA-s} = \delta_{2PA-r} \frac{\Phi_r C_r \langle F \rangle_s n_s \langle P_r \rangle^2}{\Phi_s C_s \langle F \rangle_r n_r \langle P_s \rangle^2} \quad (3)$$

where subscripts *R* and *S* refer to the reference and sample, respectively,  $\Phi$  is fluorescence quantum yield, *C* is the concentration, *F* is the integrated area, *n* is the refractive index of the solvent, and *P* is the incident power of the laser. The experimental fluorescence excitation and detection conditions were measured with negligible reabsorption..<sup>23</sup> The quadratic dependence of two-photon induced fluorescence intensity on the excitation power was verified for each excitation wavelength.

Excitation anisotropy and 2PA cross section values are shown in Figure 3. Even though the highest value of the 2PA cross section does not exactly coincide with the anisotropy minimum, it is close (400 to 600 nm, indicating possible  $S_0 \rightarrow S_n$  electronic transitions. The

highest value of the 2PA cross section for squaraine **2** was ~6000 GM at 860 nm over two orders of magnitude higher than the commercially available Cy 5 (~500 GM at 820 nm, see SI).

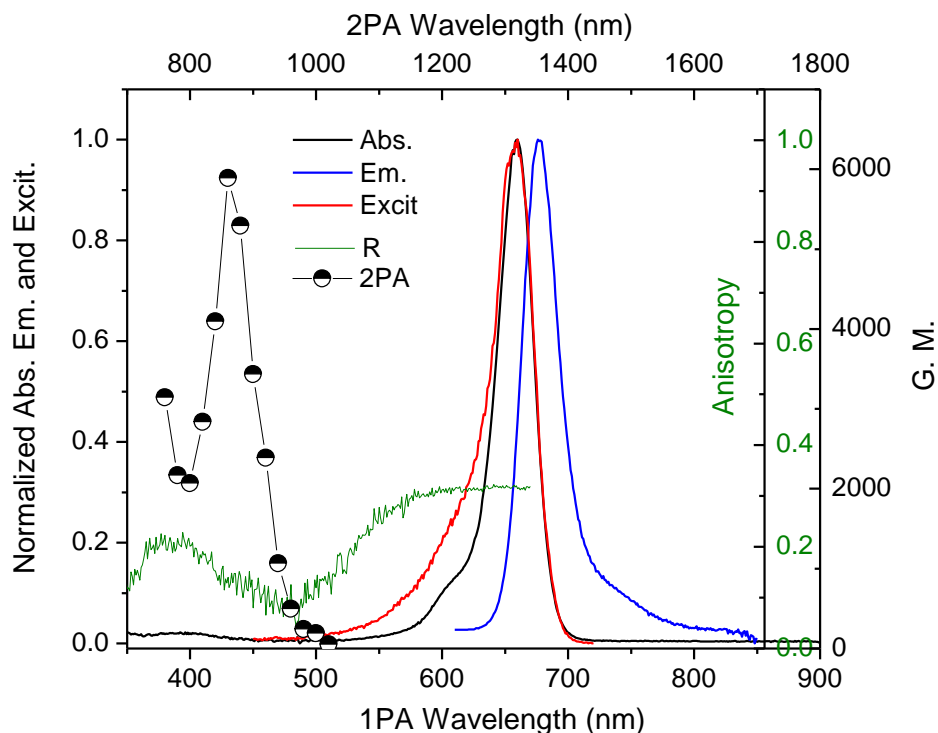


**Figure 3.** Linear and nonlinear optical spectra of squaraine **2** (1 GM (Göppert Meyer) =  $10^{-50}$  cm<sup>4</sup> s/photon<sup>-1</sup>, uncertainty of the 2PA value = 15 %).

2PA cross sections of the squaraine dyes were measured in aqueous micelle media. Squaraine **1** exhibited a 2PA cross section up to ~3500 GM while the 2PA cross section of squaraine **2** was up to ~2,000 GM. The 2PA of Cy 5 was ~100 GM under these conditions. The data indicates the nonlinear absorption of the compounds decreased when they were

encapsulated in micelles, yet squaraines **1** and **2** exhibited two-photon absorptivity up to 35 times greater than the commercially available NIR dye Cy 5.

Photostability is an important attribute for the application of fluorescent dye in fluorescence microscopy due to prolonged or repeated irradiation of the compound.<sup>31</sup> The photochemical stability of the dyes was investigated in DMSO (see in the Supporting Information) and in aqueous micelle media to obtain a deeper insight into the relationship between the structure and photostability of the squaraine dyes. Commercial Cy 5 dye was studied as well for comparison. Measurements were obtained by irradiating the sample in a 10 mm path length quartz cuvette using a 650 nm diode laser (60 mW) and recording the differences between absorbencies as a function of time as shown in Figure 4. The results indicated that the squaraine dyes **1** and **2** were more photostable than commercial Cy 5 in aqueous micelles. Photostability is defined by time-dependent variation in absorption maxima ( $A/A_0$ ) of three dyes in Figure 4 (d), a parameter that can be quantified by calculating the photochemical decomposition quantum yield ( $\eta$ ).<sup>22</sup>

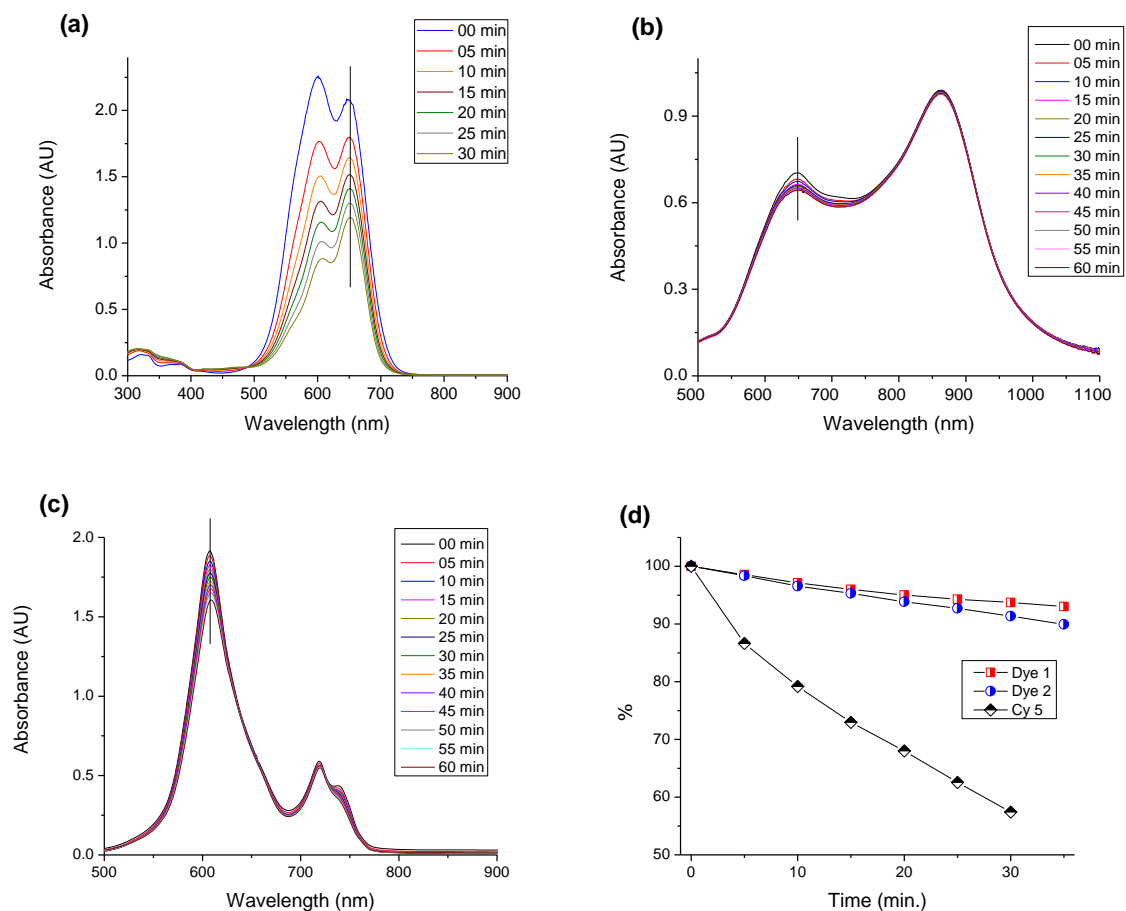


**Figure 4.** Kinetic changes in the absorption spectra of corresponding dyes by excited at 650 nm argon degas of micelles (a) Cy 5, (b) dye **1**, (c) dye **2**, and (d) the percentage of the absorption comparison over three dyes.

Photodecomposition quantum yields,  $\eta$ , were calculated as follows,

$$\eta = \frac{(A_1 - A_0)N_A}{\epsilon I \left(1 - 10^{\frac{A_1 + A_0}{2}}\right)(t_1 - t_0)} \quad (4)$$

where  $\eta$  is the photochemical decomposition quantum yield,  $A_I$  is absorbance maxim at  $t_I$ ,  $A_0$  is absorbance max at  $t_0$ ,  $N_A$  is Avogadro's number,  $\varepsilon$  is molar absorbance in  $M^{-1}\cdot cm^{-1}$ ,  $(t_I-t_0)$  is time exposed (s), and  $I$  is the intensity of laser in  $photon\cdot cm^{-2}\cdot s^{-1}$ . The results shown in Table 3 are averages of seven to ten pairs of adjacent maximum absorption values. Squaraine **1** was twice as stable than Cy 5 in DMSO while the photostability of the squaraine dyes was one order of magnitude higher than Cy 5 in aqueous micelle media.

The two-photon action cross section is means for estimating the relative efficiency of a fluorescence probe.<sup>32</sup> The two-photon action cross section is the product of the fluorescence quantum yield and the 2PA cross section (the highest value of 2PA spectrum of each dye), i.e.,  $\Phi_{FL}\cdot\delta_{2PA}$ . The results indicate that the two-photon action cross section of our squaraine dyes is two orders of magnitude greater than Cy 5. Given the  $\eta$  value, a figure of merit ( $F_M$ ) can be defined for the dye.<sup>33</sup> This is a measure of not only the efficiency of the probe but also its photostability and stability, and can be derived from the action cross section normalized by  $\eta$ , i.e.,  $F_M = \Phi_{FL}\cdot\delta_{2PA} / \Phi_{decomp}$  as shown in Table 3.

**Table 3.** Photochemical decomposition quantum yields ( $\eta$ ) and figure of merits ( $F_M$ ) of dye **1** and **2** in DMSO and micelles encapsulated dye.

<i>Solvent</i>	<i>Dye</i>	$\varepsilon$	$\Phi_{FL}$	$\delta_{2PA}$	$\eta$	$\Phi_{FL} \cdot \delta_{2PA}$	$F_M$
DMSO	Dye 1	3.10E+05	0.11	20000	1.84E-06	2200	1.20E+09
	Dye 2	2.90E+05	0.62	6000	2.74E-05	3720	1.36E+08
	Cy 5	4.00E+05	0.45	500	2.37E-06	225	9.49E+07
Micelle	Dye 1	5.50E+04	0.005	3500	4.60E-05	17.5	3.80E+05
	Dye 2	1.00E+05	0.004	2000	6.50E-05	8	1.23E+05
	Cy 5	1.50E+05	0.017	100	4.38E-04	1.7	3.88E+03

Molar absorptivity,  $\varepsilon = \text{M}^{-1} \cdot \text{cm}^{-1}$ ) fluorescence quantum yield,  $\Phi_{FL}$ , the highest two-photon cross section,  $\delta_{2PA}$ , photochemical decomposition quantum yield,  $\eta$ , action cross section,  $\Phi_{FL} \cdot \delta_{2PA}$ , figure of merit,  $F_M$

In addition to photostability, thermal stability is also a key attribute of a compound, because even though temperatures that a probe may be exposed to are not typically very high, it will often be heated, e.g., in an incubator. Thermostability testing of squaraine dyes were performed using thermogravimetric analysis (TGA) and differential scanning calorimetry (DSC) (see Supporting Information). The thermal decomposition temperature,  $T_d$ , is determined by using TGA from the measurement of the change in mass of the sample with varying temperature. Thermostability can be determined by DSC which measures the heat flow in the sample by the function of temperature.  $T_d$  of squaraine **1** was ca. 400 °C that shows very high thermostability and it has very stable thermal heating and cooling scanning cycles.  $T_d$  of squaraine **2** was ca. 230 °C. The data indicates that both dyes have ample thermostability properties required for biological research.

Since we are considering squaraines **1** and **2** for potential bioimaging applications, biocompatibility is very important, yet, not much is known for squaraine dyes. Cytotoxicity tests were performed using HCT 116 and COS 7 cell lines, two commonly employed cell lines (Figure 5). HCT 116 is one of the human colorectal cancer cells. COS 7 is a kidney cell line from African green monkeys modified with SV40 virus. The concentrations of squaraine **1** ranged from 0.1  $\mu\text{M}$  to 20.0  $\mu\text{M}$ . The percent of viable cells remained above 80%. The viability of squaraine **2** was above 80% until 30  $\mu\text{M}$ .

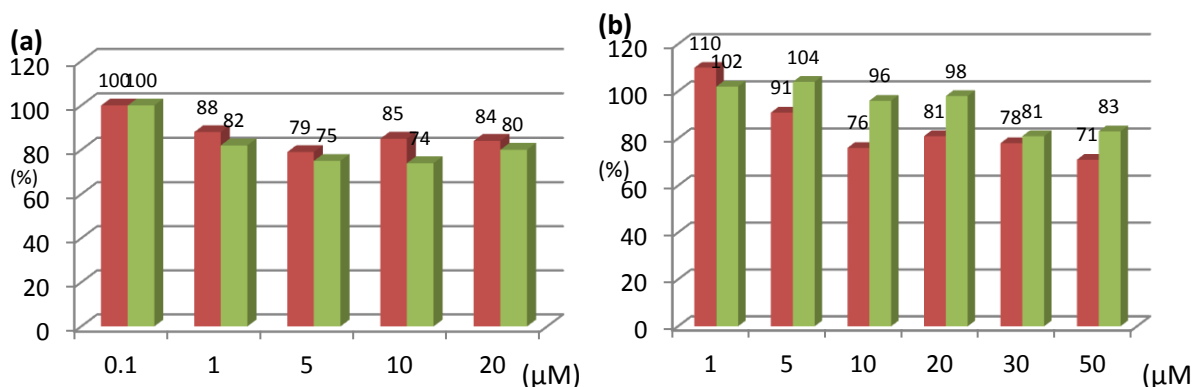


**Figure 5.** Cell Viable test in ■ HCT 116 and ■ COS 7 of (a) squaraine **1** and (b) squaraine **2** (error bar =  $\pm 7\%$ ).

Based on the cell viability test results, all concentrations studied were appropriate for imaging. Concentrations of 20 and 50  $\mu\text{M}$  were employed for 1PFM and 2PFM imaging in HCT 116 and COS 7 cells. A concentration of 20  $\mu\text{M}$  was selected for 1PFM imaging, as shown in Figures 6 to 9. Customized filter cubes, fluo out (Ex 377/50, DM 409, Em 525/40) and Cy 5 filter (Ex 630/50, DM 660, Em 690/40), were used for Hoechst and our squaraine dye channels,

respectively. Even though HCT 116 and COS 7 cell lines are quite different, our analysis shows that the probes appear to be uptaken, perhaps into endosomes, as it was clearly not colocalized with the nuclear stain Hoechst.

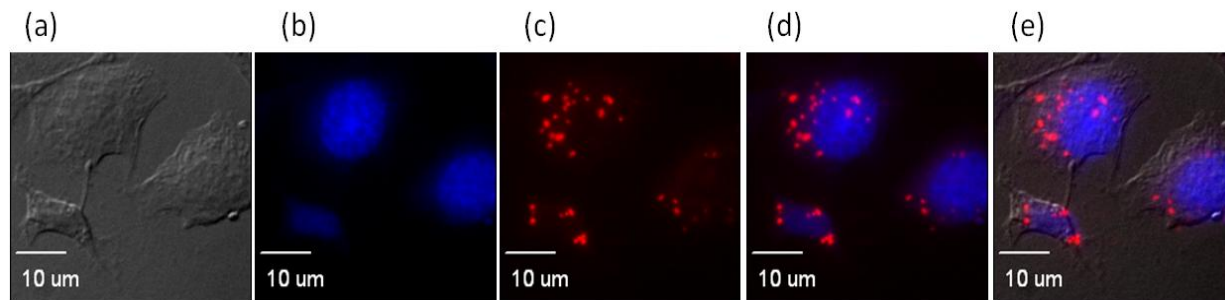


**Figure 6.** HCT 116 of 20  $\mu$ M squaraine **1** (a) DIC, (b) 1PA image with Fluo out (Ex 377/50, DM 409, Em 525/40), (c) 1PA image with Cy 5 filter (Ex 630/50, DM 660, Em 690/40), (d) 1PA overlaid fluorescence image, (e) 1PA overlaid image (a) to (c) (scale bar = 10  $\mu$ m).

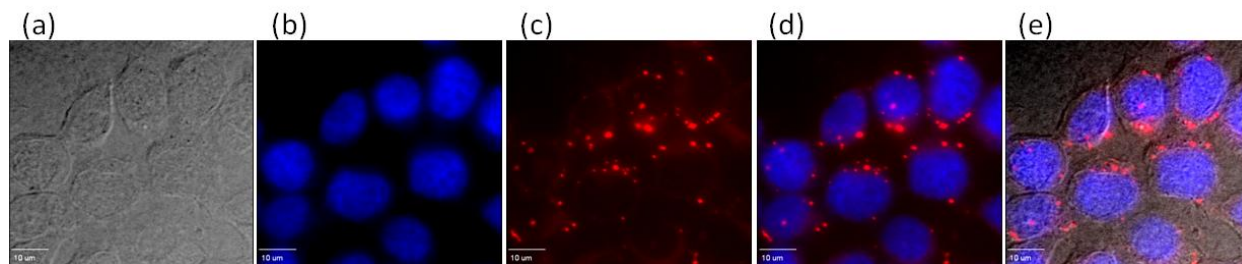


**Figure 7.** HCT 116 of 20  $\mu$ M squaraine **2** (a) DIC, (b) 1PA image with Fluo out (Ex 377/50, DM 409, Em 525/40), (c) 1PA image with Cy 5 filter (Ex 630/50, DM 660, Em 690/40), (d) 1PA overlaid fluorescence image, (e) 1PA overlaid image (a) to (c) (scale bar = 10  $\mu$ m).

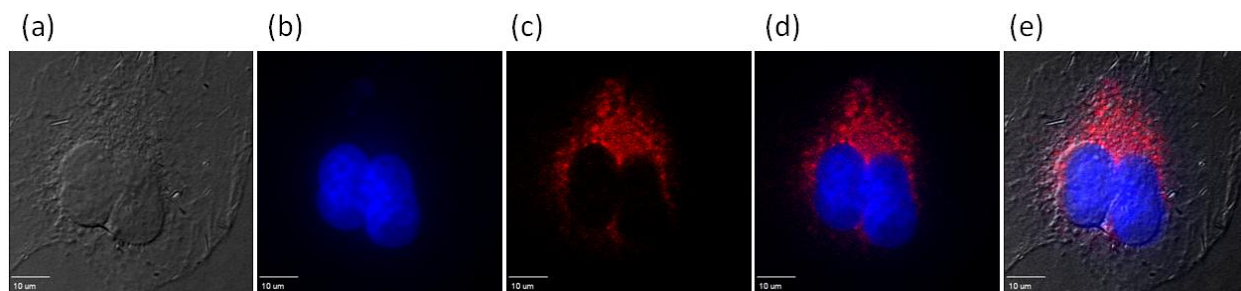


**Figure 8.** COS 7 of 20  $\mu\text{M}$  squaraine **1** (a) DIC, (b) 1PA image with Fluo out (Ex 377/50, DM 409, Em 525/40), (c) 1PA image with Cy 5 filter (Ex 630/50, DM 660, Em 690/40), (d) 1PA overlaid fluorescence image, (e) 1PA overlaid image (a) to (c) (scale bar = 10  $\mu\text{m}$ ).

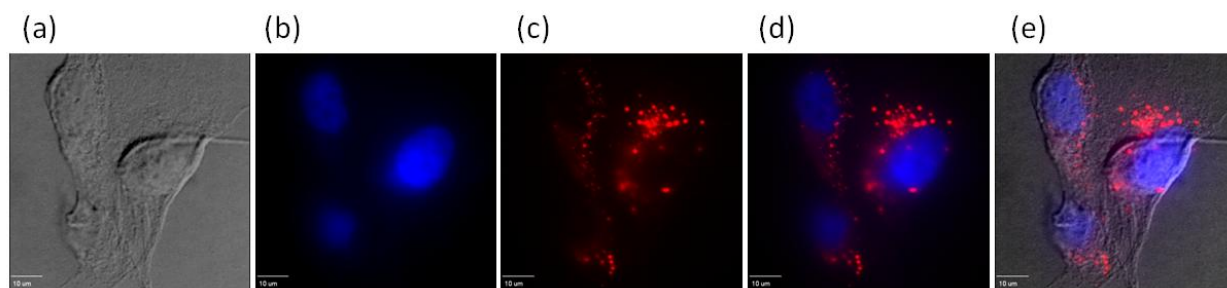


**Figure 9** COS 7 of 20  $\mu\text{M}$  squaraine **2** (a) DIC, (b) 1PA image with Fluo out (Ex 377/50, DM 409, Em 525/40), (c) 1PA image with Cy 5 filter (Ex 630/50, DM 660, Em 690/40), (d) 1PA overlaid fluorescence image, (e) 1PA overlaid image (a) to (c) (scale bar = 10  $\mu\text{m}$ ).

2PMF images were obtained using a fs Ti:sapphire Mira 900 laser tuned to 850 nm (70 mW, 694 nm short pass cutoff filter) as shown in Figure 10. Since the  $F_M$  value of both dyes is very high, the 2PFM images were very bright, suggesting the potential of these squaraine dyes for other bioimaging applications such as *ex vivo* and *in vivo* imaging.

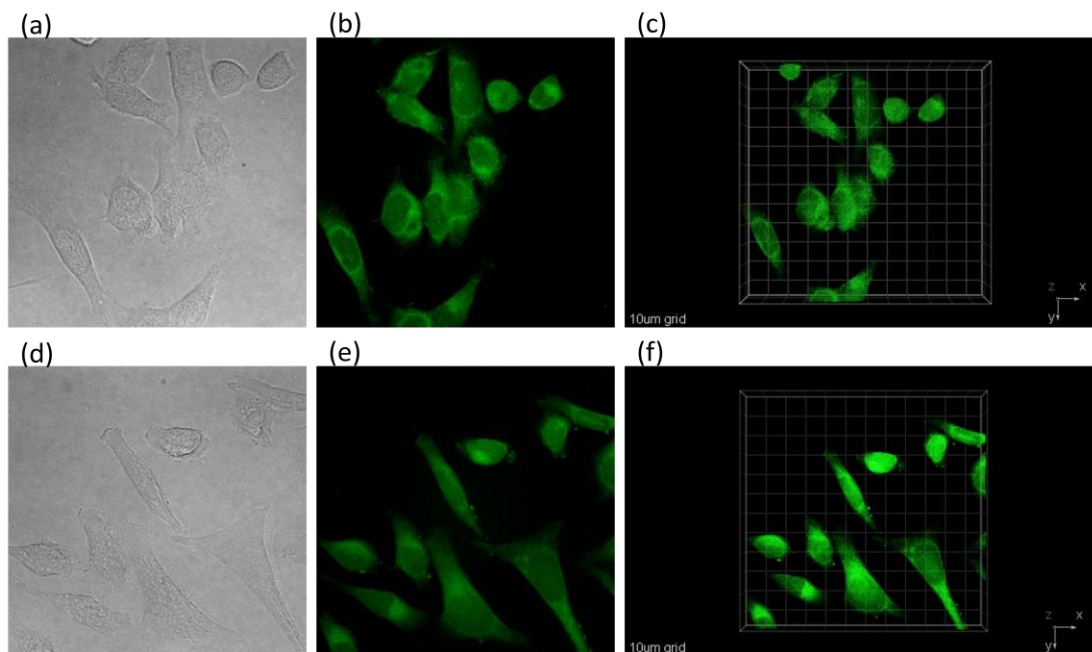


**Figure 10.** HCT 116 images of squaraine **1** (a) DIC, (b) 2PFM (c) 2PFM 3D reconstruction, and HCT 116 images of squaraine **2** (a) DIC, (b) 2PFM (c) 2PFM 3D reconstruction (scale bar = 10  $\mu\text{m}$ ).

## **2-5. Conclusions**

We report the linear and nonlinear photophysical properties of squaraine dyes **1** and **2** in several organic solvents and aqueous media via encapsulated dye micelles. The relative quantum yields of both probes were reasonable and, not surprisingly, both exhibited somewhat reduced fluorescence quantum yields in aqueous micelle media. Squaraine **1** exhibited an impressive 2PA cross section of ca. 20,000 GM at 800 nm and ca. 1,000 GM at wavelengths just over 1,000 nm, creating several possibilities for two-photon excitation wavelengths. The photostability of the new dyes was compared with commercially available NIR dye Cy 5. The photostability of the

new squaraine probes were one order of magnitude higher than Cy 5, an important finding in the development of probes for bioimaging. The squaraine dyes were rather benign to HCT 116 and COS 7 cell lines with cell viability percent of both cell lines above ca. 80% even though the concentration of the dye was up to 50  $\mu$ M, an indication of good biocompatibility. One-photon fluorescence microscopy (1PFM) and two-photon fluorescence microscopy (2PFM) imaging was demonstrated for squaraine probes **1** and **2** in both cell lines. These results suggest the potential utility of the probes for both conventional and two-photon based *ex vivo* and *in vivo* bioimaging.

### References

- (1) Beverina, L.; Salice, P. *Euro. J. Organic Chem.* **2010**, 1207-1225.
- (2) Treibs, A. J., K. *Angew. Chem., Int. Ed.* **1965**, 77, 680-1.
- (3) Sprenger, H. E., Ziegenbein, Willi *Angew. Chem., Int. Ed.* **1966**, 78, 937-8.
- (4) Law, K.-y. *J. Phys. Chem.* **1988**, 92, 4226-4231.
- (5) Yum, J.-h.; Walter, P.; Huber, S.; Rentsch, D.; Geiger, T.; Nu, F.; Angelis, F. D.; Gra, M.; Nazeeruddin, M. K. *Langmuir* **2007**, 129, 10320-10321.
- (6) Corredor, B. C. C.; Huang, Z.-l.; Belfield, K. D. *Adv. Mater.* **2006**, 18, 2910-2914.
- (7) Smits, E. b.; Setayesh, S.; Anthopoulos, T. D.; Buechel, M.; Nijssen, W.; Coehoorn, R.; Blom, P. W. M.; de Boer, B.; de Leeuw, D. M. *Adv. Mater.* **2007**, 19, 734-8.
- (8) Chen, C.-T.; Marder, S. R.; Cheng, L.-t. *J. Am. Chem. Soc.* **1994**, 116, 3117-3118.

- (9) Song, B.; Zhang, Q.; Ma, W.-H.; Peng, X.-J.; Fu, X.-M.; Wang, B.-S. *Dyes Pigm.* **2009**, *82*, 396-400.
- (10) Santos, P. F.; Reis, L. V.; Almeida, P.; Serrano, J. P.; Oliveira, A. S.; Ferreira, L. F. V. *J. Photochem. Photobiol., A* **2004**, *163*, 267-269.
- (11) Arunkumar, E.; Fu, N.; Smith, B. D. *Chemistry; A European Journal* **2006**, *12*, 4684-4690.
- (12) Kopainsky, B.; Qiu, P.; Kaiser, W. *Appl. Phys. B: Lasers Opt.* **1982**, *29*, 15-18.
- (13) Pham, W.; Lai, W.-F.; Weissleder, R.; Tung, C.-H. *Bioconjugate Chem.* **2003**, *14*, 1048-51.
- (14) Patonay, G.; Salon, J.; Sowell, J.; Strekowski, L. *Molecules* **2004**, *9*, 40-9.
- (15) Chung, S.-J.; Zheng, S.; Odani, T.; Beverina, L.; Fu, J.; Padilha, L. A.; Biesso, A.; Hales, J. M.; Zhan, X.; Schmidt, K.; Ye, A.; Zojer, E.; Barlow, S.; Hagan, D. J.; Van Stryland, E. W.; Yi, Y.; Shuai, Z.; Pagani, G. A.; Bredas, J.-L.; Perry, J. W.; Marder, S. R. *J. Am. Chem. Soc.* **2006**, *128*, 14444-5.
- (16) Odom, S. A.; Webster, S.; Padilha, L. A.; Peceli, D.; Hu, H.; Nootz, G.; Chung, S.-J.; Ohira, S.; Matichak, J. D.; Przhonska, O. V.; Kachkovski, A. D.; Barlow, S.; Bredas, J.-L.; Anderson, H. L.; Hagan, D. J.; Van Stryland, E. W.; Marder, S. R. *J. Am. Chem. Soc. Comm.* **2009**, *131*, 7510–7511.

- (17) Hu, H.; Gerasov, A. O.; Padilha, L. A.; Przhonska, O. V.; Webster, S.; Shandura, M. P.; Kovtun, Y. P.; Masunov, A. E.; Hagan, D. J.; Stryland, E. W. V. *IEEE CLEO* **2010**.
- (18) Toro, C.; De Boni, L.; Yao, S.; Ritchie, J. P.; Masunov, A. E.; Belfield, K. D.; Hernandez, F. E. *J.Chem. Phys.* **2009**, *130*, 1-6.
- (19) Fu, J.; Przhonska, O. V.; Padilha, L. A.; Hagan, D. J.; Van Stryland, E. W.; Belfield, K. D.; Bondar, M. V.; Slominsky, Y. L.; Kachkovski, A. D. *Chem. Phys.* **2006**, *321*, 257-268.
- (20) Lakowicz, J. R. *Principles of Fluorescence Spectroscopy* **2006**, Springer.
- (21) Sheik-bahae, M.; Said, A. A.; Wei, T.-h.; Hagan, D. J.; Van Stryland, E. W. *IEEE J. Quantum Electron.* **1990**, *26*, 760-769.
- (22) Corredor, C. C.; Belfield, K. D.; Bondar, M. V.; Przhonska, O. V.; Yao, S. *J. Photochem. Photobiol., A* **2006**, *184*, 105-112.
- (23) Tristani-Kendra, M.; Eckhardt, C. J. *J. Chem. Phys.* **1984**, *81*, 1160-1173.
- (24) Chen, H.; Farahat, M. S.; Law, K.-y.; Whitten, D. G. *J. Am. Chem. Soc.* **1996**, *118*, 2584-2594.
- (25) Tatikolov, A. S.; Panova, I. G.; Ishchenko, A. A.; Kudinova, M. A. *Biophysics* **2010**, *55*, 35-40.
- (26) Muino, P. L.; Callis, P. R. *J. Phys. Chem. B* **2009**, *113*, 2572-7.

- (27) Belfield, K. D.; Bondar, M. V.; Przhonska, O. V.; Schafer, K. J. *J. Fluoresc.* **2002**, *12*, 449-454.
- (28) Scheblykin, I. G.; Drobizhev, M. A.; Varnavsky, O. P.; M.; Vitukhnovsky, A. G. *Chem. Phys. Lett.* **1996**, *261*, 181-190.
- (29) Belfield, K. D.; Bondar, M. V.; Hernandez, F. E.; Przhonskac, O. V.; Yao, S. *Chemical Physics* **2006**, *320*, 118-124.
- (30) Wang, X.; Yao, S.; Ahn, H.-Y.; Zhang, Y.; Bondar, M. V.; Torres, J. A.; Belfield, K. D. *Biomed. Opt. Express* **2010**, *1*, 11539-11544.
- (31) Song, F. *J. Photochem. Photobiol., A* **2004**, *168*, 53-57.
- (32) Mulligan, S. J.; Macvicar, B. A. *Modern Reaserch an Educational Topics in Microsc.* **2007**, 881-889.
- (33) Wang, X.; Nguyen, D. M.; Yanez, C. O.; Rodriguez, L.; Ahn, H.-Y.; Bondar, M. V.; Belfield, K. D. *Journal of the American Chemical Society* **2010**, *132*, 12237-9.

## **CHAPTER 3: PROFLUORESCENT NITROXIDES: LINEAR AND NONLINEAR PHYTOPHYSICAL CHARACTERIZATION AND USE FOR OXIDATIVE STRESS PROBE**

### **3-1. Abstract**

Chromophore-functionalized nitroxides and their methylated analogs were synthesized and their linear photophysical properties were determined. The NOME analogs had characteristically high fluorescence quantum yields, approaching unity. Two-photon absorption (2PA) cross sections were measured with two compounds exhibiting 2PA cross sections ca. ~400 G.M. when excited at wavelengths greater than 800 nm. The combination of high fluorescence quantum yield of the NOME derivatives, low fluorescent quantum yield of the corresponding nitroxides (profluorescent nitroxide), and reasonable 2PA cross section suggests the potential for use of the profluorescent nitroxide as oxidative stress indicators visualized by two-photon fluorescence microscopy. The cytotoxicity of selected profluorescent nitroxides was examined in Chinese Hamster Ovary (CHO) cells, indicating low toxicity while colocalization with commercially available CellMask Deep Red oxidative stress detecting probe, after inducing oxidative stress with H<sub>2</sub>O<sub>2</sub>, indicated good localization (up to 96%) of the new probes. One-photon and two-photon fluorescence microscopy imaging demonstrated the ability of the nitroxide probes for indication of oxidative stress *in vitro*.

### **3-2. Introduction**

Since the 1960s, nitroxides, a stable free radical group, have been investigated due to their unique physical and chemical properties.<sup>1</sup> Nitroxide radicals are utilized for electron paramagnetic resonance (EPR) spectroscopy, such as spin trapping and spin labeling<sup>2</sup> exploiting their paramagnetic properties, and for monitoring cellular redox processes using their redox changes.<sup>3</sup> The first observation of a nitroxide in a biological system was the mimetic behavior of superoxide dismutase (SOD).<sup>4</sup> SOD is one of the enzymes used to catalyze the dismutation of superoxide into oxygen and hydrogen peroxide. Superoxide, one of the main reactive oxygen species in the cell, produces oxidative stress, which is an unbalanced redox state in a normal biological system. This unbalanced condition leads to cellular damage due to the creation of peroxides and free radicals. This oxidative stress is a causal factor in cellular mutative diseases such as cardiovascular aging,<sup>5</sup> Parkinson's disease,<sup>6</sup> and Alzheimer's disease.<sup>7</sup> SOD is used as an antioxidant to reduce oxidative stress in the cell. As a result of the relatively large size of SOD (which reduces membrane permeability), nitroxides (having similar characteristics as SOD) have been studied as potential antioxidants<sup>8</sup> in mammalian cells.

Another area that was explored with nitroxides was tethering a fluorophore moiety,<sup>9</sup> known as profluorescent nitroxides or dual chromophores-nitroxides. This technique is used in other applications such as optical sensors<sup>10</sup> or bio-probes. A profluorescent nitroxide is a species with very low fluorescence quantum yield, and, once the nitroxide spin is removed, the fluorophore can emit photons.<sup>11</sup> Depending on the chromophore moiety of the profluorescent nitroxide species, one can tune the absorption and emission wavelength through modification of the molecular structure for different applications, such as molecular probes or modeling

intramolecular photochemical and photophysical processes. Here, we report new profluorescent nitroxides for use as a two-photon fluorescent oxidative stress indicator in a two-photon fluorescence microscopy (2PFM) imaging.

### **3-3. Experimental Materials and Methods**

#### **Synthesis**

Ten nitroxide (profluorescent) and the corresponding NOME (fluorescent) pairs were provided by Dr. Steven Bottle's research group for this study.

#### **Methods**

##### *Linear optical properties*

Linear absorption was measured with an Agilent 8453 UV-vis spectrophotometer. Fluorescence emission and excitation spectra were measured using by a PTI Quantamaster Spectrofluorimeter equipped with a Hamamatsu R928 photomultiplier tube (PMT). Emission spectra were measured in cyclohexane, CH<sub>2</sub>Cl<sub>2</sub>, or water depending on the solubility of a compound. Excitation anisotropy spectra were measured with two Glan-Thomson polarizers in an L-format method in high viscosity solvent (glycerol, Acros) to avoid reorientation, and in low concentration solutions ( $C \sim 10^{-6}$  M) to avoid reabsorption.<sup>12</sup>

Lifetime measurements were performed using a tunable Ti: sapphire laser system (Coherent Verdi-V10 and MIRA 900, pulse duration ~200 fs/pulse (FWHM), and repetition rate 76 MHz) coupled with second harmonic generator. The polarization of the excitation beam was linear and oriented by the magic angle to avoid molecular reorientation effects. A broad band-

pass filter (400 to 600 nm, or 500 to 700 nm, depending on the emission range of a compound) was placed in front of an avalanche photodiode detector (APD, PicoQuant GmbH, LSM\_SPAD). Data was acquired with a PicoQuant time-correlated single photon counting system, PicoHarp300 (Figure 11). The optical density of all the solutions did not exceed 0.12 at the excitation wavelength to avoid reabsorption. Measurements were conducted in 10 mm path length quartz cuvettes at room temperature.

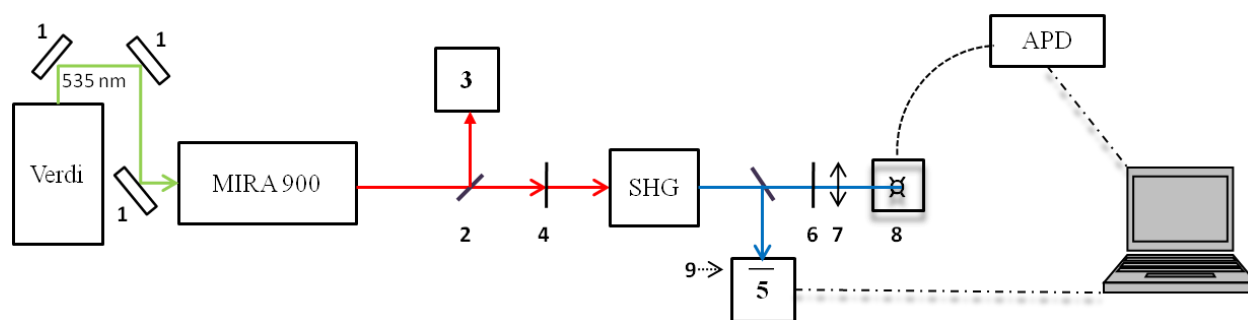


**Figure 11.** Fluorescence lifetime setup (1) 100% reflection mirror, (2) beam splitter, (3) spectrometer, (4) neutral density filter, (5) APD beam trigger, (6) Glan-Thomson polarizer, (7) focusing lens, (8) sample holder, and (9) broad band-pass filter.

### Nonlinear optical spectra measurements

Two-photon absorption (2PA) measurements were performed using a Coherent Legend Elite system (amplified Ti:sapphire system) that pumped an optical parametric generator/amplifier (Coherent OPerA Solo), providing laser pulses of 100 fs (FWHM) duration with 1 kHz repetition rate (Figure 12). The system was coupled with a PTI Quantamaster

Spectrofluorimeter and R928 PMT. The 2PA spectrum was determined over a broad spectral region from 580 to 1020 nm by the two-photon induced fluorescence method with  $10^{-5}\text{M} \leq C \leq 10^{-3}\text{M}$  concentration solutions were in a 10 mm quartz cuvette at room temperature relative to Rhodamine B.<sup>13</sup> All linear and nonlinear measurements were carried out in spectroscopic grade solvents.

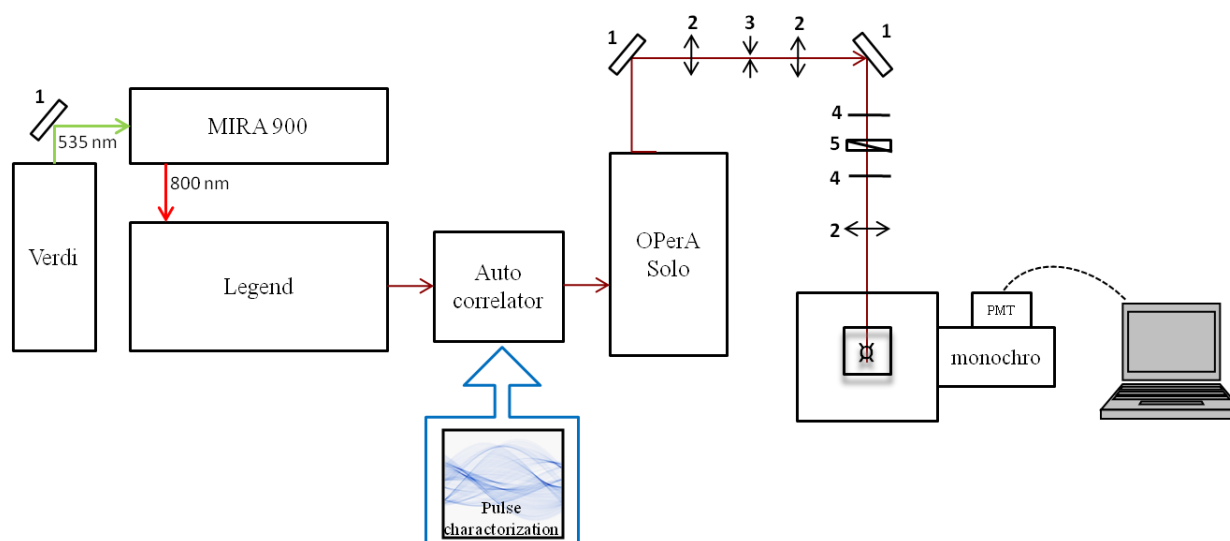


**Figure 12.** Two-photon absorption (2PA) induced fluorescence setup, (1) 100% reflection mirror, (2) focusing mirror, (3) pin hole, (4) Glan-Thomson polarizer, and (5) half wave plate.

## Cell Assay

### Micelle Encapsulation

A concentrated micelle stock solution was prepared using 1 mg/mL of the dye by using a small amount of  $\text{CH}_2\text{Cl}_2$  to dissolve the dye. Water was added with 2 wt% of surfactant (Pluronic

F 127 Prill, BASF Corporation) and stirred overnight. The crude solution was filtered before using. The concentration of the micelle-encapsulated probe stock solution was determined via UV-vis spectrophotometry using the molar absorptivity.

### Cell lines

Chinese Hamster Ovary (CHO) cells were purchased from America Type Culture Collection (ATCC, Manassas, VA, USA). All cells were incubated at 37 °C in a 95% humidified atmosphere containing 5% CO<sub>2</sub> in cell media (RPMI medium with 10 % fetal bovine serum, 1% Pen Strep (penicillin streptomycin, Invitrogen, Carlsbad, CA, USA), and 0.75 g of sodium bicarbonate).

### Cytotoxicity Assay

CHO cells were prepared for cell viability studies in 96-well plates ( $4 \times 10^3$  cells per well that were incubated in 90  $\mu$ L). The cells were incubated for an additional 20 h with dyes encapsulated in micelles (**19** and **20**) and aqueous solution (4BM47 and 4BM66) in different concentrations. Subsequently, 10  $\mu$ L of MTS assay (CellTiter 96® Aqueous One Solution reagent) was added into each well, followed by further incubation for 4 h at 37 °C. The relative viability of the cells incubated with dyes to untreated cells was determined by measuring the MTS-formazan absorbance on a microplate reader (Spectra Max M5, Molecular Devices) at 538 nm with subtraction of the absorbance of the cell-free blank volume at 538 nm.<sup>14</sup> The results from the three individual experiments were averaged.

### Cell Culture and Fixing

CHO cells were placed onto poly-D-lysine coated glass cover slips (12 mm, #1) in 24-well plates,  $3 \times 10^4$  cells per well, and the cells were incubated for 48 h before incubating with the prepared dyes. Diluted hydrogen peroxide (6% solution, Fisher Science) was added for inducing oxidative stress, and the cells were incubated for 1 h. The filtered stock solution was then diluted with complete growth medium, RPMI-1640, and then incubated for 1.5 h. The cells were incubated for additional 30 min for staining with commercial dyes individually. The stains used were 5  $\mu\text{g/mL}$  of Hoechst and 5  $\mu\text{M}$  of CellROX Deep Red reagent. After incubation, the cells were washed with PBS (x 5) and fixed using 3.7% formaldehyde solution for 15 min at 37 °C. Then freshly prepared  $\text{NaBH}_4$  (1 mg/mL, prepared by adding a couple of drops of 0.1 M NaOH) solution in PBS (PBS pH = 7.4, with 0.1 M NaOH = pH 8) was added to each well (0.5 mL/well) for 15 min. The plates were then washed with PBS (x 2) and water (x 1). Finally, the glass cover slips were mounted using Prolong Gold mounting media (Invitrogen) for microscopy.

### One- and Two-Photon Fluorescence Microscopic (1PFM and 2PFM) Images

A Leica TCS SP5 MP confocal microscope system coupled to Coherent Chameleon Vision S Ti:sapphire laser (~ 70 fs (FWHM), 90 MHz repetition rate) was used for one-phootn fluorescence microscopy (1PFM) and 2PFM imaging with a 63x wtare immersion objective (Leica 506279). Visible lasers in the TCS SP5 system were employed for 1PFM while the Coherent Chameleon system was used for 2PFM imaging. Leica LAS AF software was used for capturing and processing images. The excitation wavelength for nitroxides **19** and **47** was 458 nm, Argon laser while emission was collected from 500 to 600 nm. The Hoechst nuclear dye was excited with a 405 nm diode laser with emission collected between 420 and 460 nm. A HeNe

laser (633 nm) was used for exciting the commercial CellROX Deep Red probe while collecting the emission between 650 and 750 nm. Each image was obtained frame by frame at different wavelengths.

### **3-4. Results and discussion**

#### **Linear Photophysical Properties**

In this paper, a relatively comprehensive investigation of the linear photophysical properties of ten pairs of nitroxyl radical and their corresponding methoxy analogs (Scheme 2) is reported. Most compounds were soluble in cyclohexane (CHX) and CH<sub>2</sub>Cl<sub>2</sub>. Perylene derivatives were insoluble in CHX. Hence, spectroscopic studies for the perylenes were conducted in CH<sub>2</sub>Cl<sub>2</sub> as shown in Table 4. Finally, due to their water solubility, measurements of fluorescein derivatives were carried out in water. The synthesis and photophysical properties for diphenylanthracene derivatives (**5**, **6**, **11**, and **12**) and bis(phenylethynyl) derivatives (**16**, **17**, **19**, and **20**) were previously reported.<sup>15</sup> Herein, further investigation was performed to determine their feasibility as probes for bioimaging. Diphenylanthracene derivatives exhibited that the absorption maximum was ca. 375 nm in both CHX and CH<sub>2</sub>Cl<sub>2</sub>. The emission maxima were ca. 410 and 430 nm in CHX and CH<sub>2</sub>Cl<sub>2</sub>, respectively (see Supporting Information for absorption and emission spectra). As expected, there was a larger Stokes (up to 55 nm) in more polar solvent. Bis(phenylethynyl) derivatives had an absorption maximum of 452 and 465 nm in CHX and CH<sub>2</sub>Cl<sub>2</sub>, respectively. Emission maxima were 475 and 480 nm CHX and CH<sub>2</sub>Cl<sub>2</sub>, respectively. Two types of dansyl derivatives were prepared; dansyl sulfonamides (DS-N-3, DS-N-4, DS-N-7, and DS-N-8) and dansyl sulfonates (DS-O-3, DS-O-4, DS-O-7, and DS-O-8). The

main absorption and emission maxima for both types were ca., 340 and 470 nm, respectively, in CHX, and 350 and 510nm, respectively, CH<sub>2</sub>Cl<sub>2</sub>. The absorption and emission maxima of the perylene derivatives (nitroxide and NOME) were 526 and 534 nm in CH<sub>2</sub>Cl<sub>2</sub>, respectively, while those for the fluorescein derivatives (4BM-47 and 4BM-66) were at 490 and ca. 520 nm, respectively.

The trends for the pair of nitroxyl radical and NOME derivatives are: 1) fluorescence quantum yield of NOME were up to two orders of magnitude higher than the corresponding nitroxide, 2) fluorescence lifetimes correlated well with fluorescence quantum yield, i.e., the lifetime of the NOME was up to two orders magnitude greater than the nitroxide, due likely to electron exchange interactions. Paramagnetic species are known fluorescence quenchers, resulting in excited-state relaxation from changes in the spin multiplicity of the electronic states.<sup>16</sup> Therefore, the fluorophore moiety was quenched by the nitroxide. However, once the paramagnetic property was lost, i.e., conversion to the NOME derivative, high fluorescence efficiency was realized.

Diphenylanthracene and dansyl derivatives had not only short wavelength absorption bands but also exhibited low two-photon absorptivity.<sup>17</sup> Perylene derivatives possess a longer wavelength absorption maximum. However, the fluorescence quantum yield of NOME derivative was lower than other NOME derivatives' fluorescence. Of the bis(phenylethynyl) derivatives, compounds **16** and **19** are promising candidates. Nitroxide **19** was selected since the monofunctionality simplifies analyses relative to difunctional **16**. Therefore, due to the absorption and emission spectra range, fluorescence quantum yields, and fluorescence lifetime,

bis(phenylethynyl) derivative **19** and the fluorescein derivative **4BM-47** were good candidates as two-photon fluorescence bioimaging probes. Thus, these two compounds were investigated further for their nonlinear absorption and 2PFM bioimaging applications.

**Scheme 2.** Molecular structures of nitroxide and NOME derivatives.

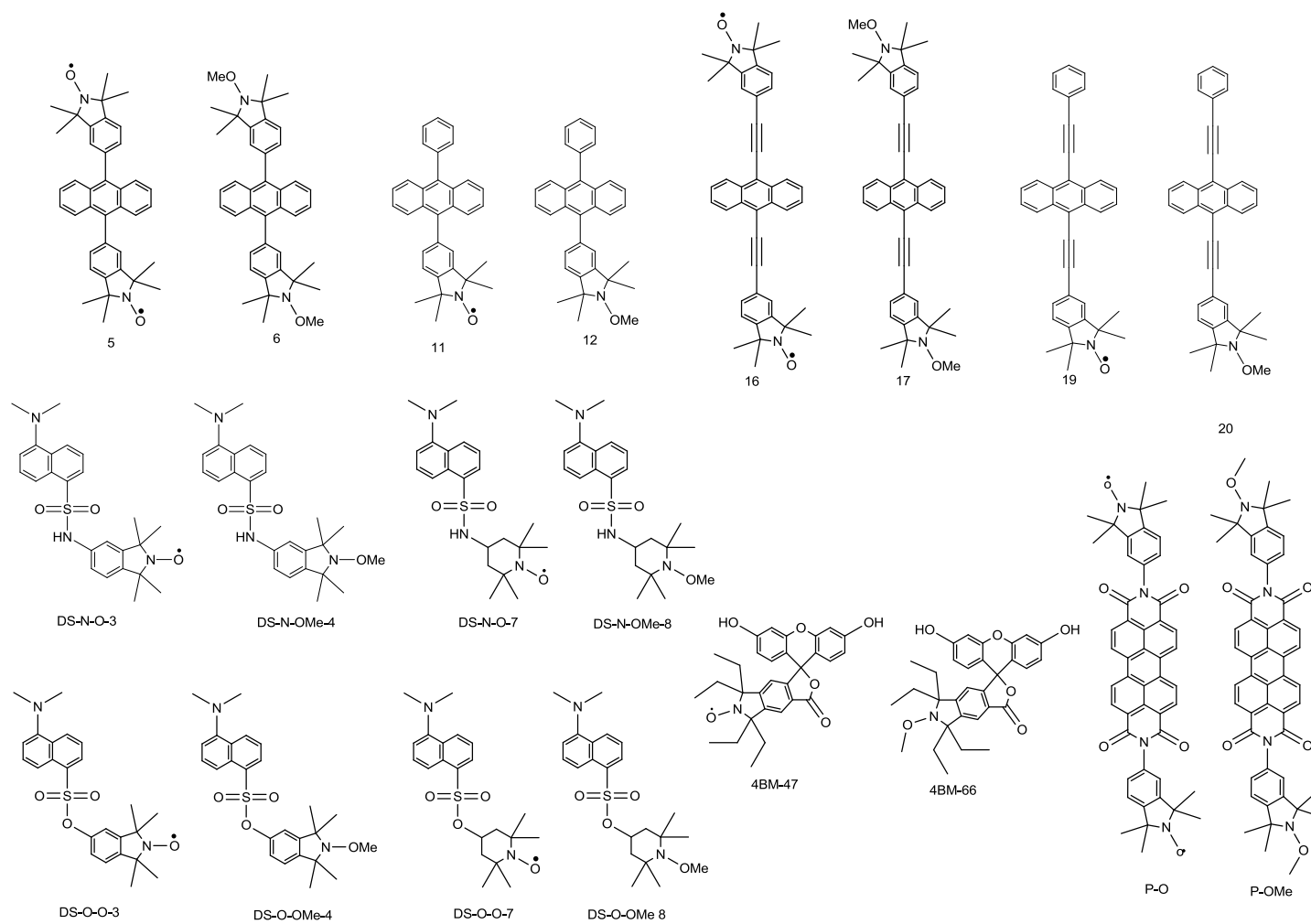


**Table 4.** Linear photophysical properties of the nitroxide and NOME derivatives.

S	cyclohexane						dichloromethane						glycerol	
	$\lambda^{\text{Abs.}}_{\text{max}}$	$\lambda^{\text{Em.}}_{\text{max}}$	$\Delta\lambda$	$\phi_{\text{FL}}$	$\tau_{\text{FL}}$ (ns)	$\chi^2$	$\lambda^{\text{Abs.}}_{\text{max}}$	$\lambda^{\text{Em.}}_{\text{max}}$	$\Delta\lambda$	$\phi_{\text{FL}}$	$\tau_{\text{FL}}$ (ns)	$\chi^2$	R	
5	374	411	37	0.041	0.48	0.92	376	416	40	0.059	0.05	0.98		
6	374	411	37	0.89	5.02	0.99	376	415	39	1.0	5.44	0.99	0.13	
11	374	418	44	0.021	0.34	0.99	375	430	55	0.017	0.07	0.91		
12	374	409	35	0.85	5.3	0.99	375	414	39	0.97	6.1	0.99	0.21	
16	452	475	23	0.025	0.16	0.99	469	481	12	0.015	0.09	0.99		
17	453	475	22	0.95	2.78	0.99	470	482	12	1.0	2.95	0.99	0.18	
19	452	473	21	0.04	0.35	0.90	465	478	13	0.011	0.10	0.98		
20	452	474	22	0.95	2.9	0.99	466	480	14	0.75	3.1	0.99	0.21	
DS-N-3	344	469	125	0.066	0.61	0.92	349	513	164	0.076	2.4	0.97		
DS-N-4	342	471	129	0.67	8.2	0.94	346	510	164	0.54	13.6	0.97	0.38	
DS-N-7	341	463	122	0.033	0.44	0.99	345	499	154	0.022	0.6	0.99		
DS-N-8	339	460	121	0.77	8.7	0.98	343	498	155	0.58	14.8	0.96	0.38	
DS-O-3	345	471	126	0.048	0.75	0.99	355	532	177	0.126	2.76	0.99		
DS-O-4	342	469	127	0.64	11.5	0.98	353	527	174	0.45	11.2	0.99	0.36	
DS-O-7	338	455	117	0.037	0.57	0.99	347	511	164	0.109	0.99	0.99		
DS-O-8	341	458	117	0.53	9.8	0.98	347	510	163	0.75	15.5	0.97	0.37	
P-NO							527	534	7	0.009	0.12	0.99		
P-NOMe							526	534	8	0.25	1.56	0.99	0.39	
							water							
4BM-47							491	511	20	0.14	0.38	0.99		
4BM-66							490	540	50	0.92	3.91	0.99	0.38	

## Nonlinear Optical Properties

When exposed to free radical species, such as products of oxidative damage in cells, the nitroxide traps free radicals, typically forming alkoxy (NOR) species. Figure 13 shows possible reactions of nitroxides in biological systems.<sup>19</sup> Since a nitroxide, and particularly the ones studied here are not fluorescent (very low fluorescence quantum yield), and the resulting free radical adduct (NOR) is typically very fluorescent (high fluorescence quantum yield), the nitroxide can serve as a profluorescent probe, essentially light up or turning on upon reaction with a radical species such as that produced by cellular oxidative stress. Thus, although the profluorescent nitroxide is incubated with cells, the NOME derivative is representative of the actual oxidation product and serves as a model probe. Therefore, the nonlinearity absorption of the NOME derivatives was measured.

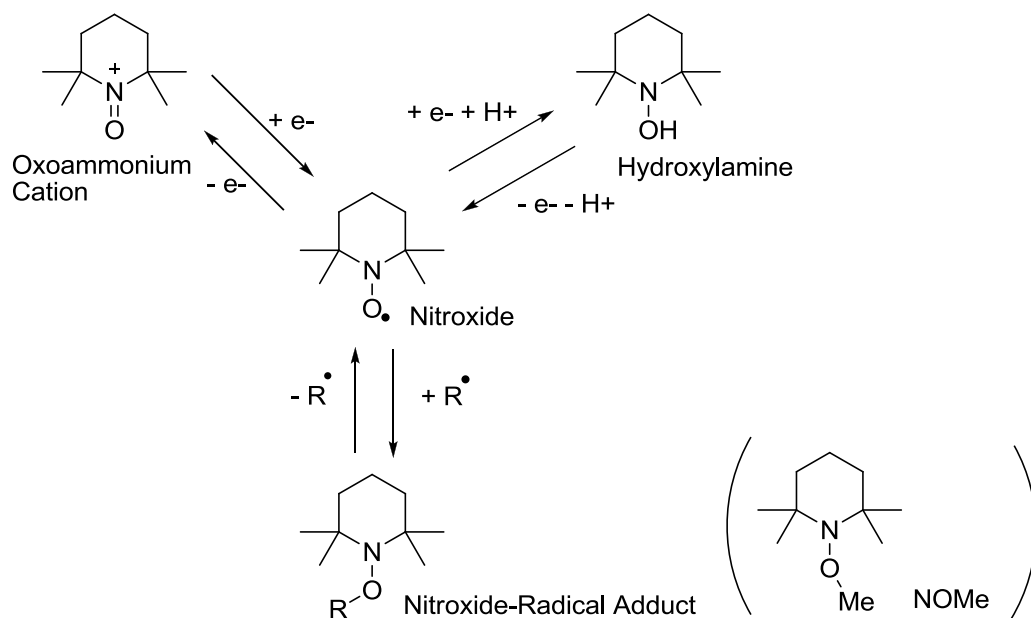


**Figure 13.** Possible reactions of nitroxides in biological systems.<sup>1</sup>

Each figure below has four different spectra; absorption (black line, normalized spectra), emission (blue, normalized spectra), anisotropy (green), and two-photon absorption (2PA) cross section (half-filled red circle). The 2PA cross section unit of measure is a value called a GM unit (1 GM (Göppert Meyer) =  $10^{-50}$  cm<sup>4</sup> s/photon<sup>-1</sup>). The 2PA spectra were recorded in 20 nm increments from 590 to 1030 nm corresponding to the top X-axis and right Y-axis.

The 2PA cross sections of NOME derivatives **20** and **66** were measured using a Coherent Legend Elite system (an amplified Ti:sapphire laser system) coupled with an OPerA Solo optical parametric amplifier ( $\sim 100$  fs (FWHM), 1 kHz repetition rate). The equation used for calculation of the 2PA cross section calculation is;

$$\delta_{2PA-s} = \delta_{2PA-r} \frac{\Phi_r C_r \langle F \rangle_s n_s \langle P_r \rangle^2}{\Phi_s C_s \langle F \rangle_r n_r \langle P_s \rangle^2} \quad (5)$$

where the subscript *R* and *S* refer to the reference and sample, respectively,  $\Phi$  is the fluorescence quantum yield, *C* is the concentration, *F* is the integrated area, *n* is the refractive index of the solvent, and *P* is the incident power of the laser. The experimental fluorescence excitation and detection were measured under conditions with negligible reabsorption (close to the cuvette wall).<sup>16</sup> Excitation anisotropy is correlated with the spectral position of various electronic transitions, and can be a very useful tool to estimate the position of 2PA allowed transitions.<sup>22</sup> the one-photon allowed S<sub>0</sub>-S<sub>1</sub> electronic transition, the maximum of the linear of absorption spectrum, is formally two-photon forbidden, according to quantum mechanical selection rules, and vice versa. In the case of the bis(phenylethynyl) derivative (**20**) the anisotropy spectrum is well correlated with the 2PA cross section data as shown in Figure 14 (a). Two maxima in the anisotropy spectrum ca. 320 and 440 nm show possible electronic transitions. These were

presumably two-photon allowed transitions, resulting in relatively high 2PA cross sections relative to other wavelengths. The highest 2PA cross section for this compound was ~500 GM at 670 nm in CHX. Predicting the position of two-photon allowed transitions is difficult because, occasionally, the one-photon allowed electron transition is also two-photon allowed, e.g., compound **4BM-66**. The highest 2PA cross section for this compound was ~400 GM at 970 nm in water (pH 8, adjusted with NaOH). Even though the 2PA cross section value is lower than **19**, it is still significant due to the desirably long wavelength that can afford deep tissue penetration for *ex vivo* and *in vivo* imaging. Hence, **4BM-66** is a potentially useful two-photon NIR probe.

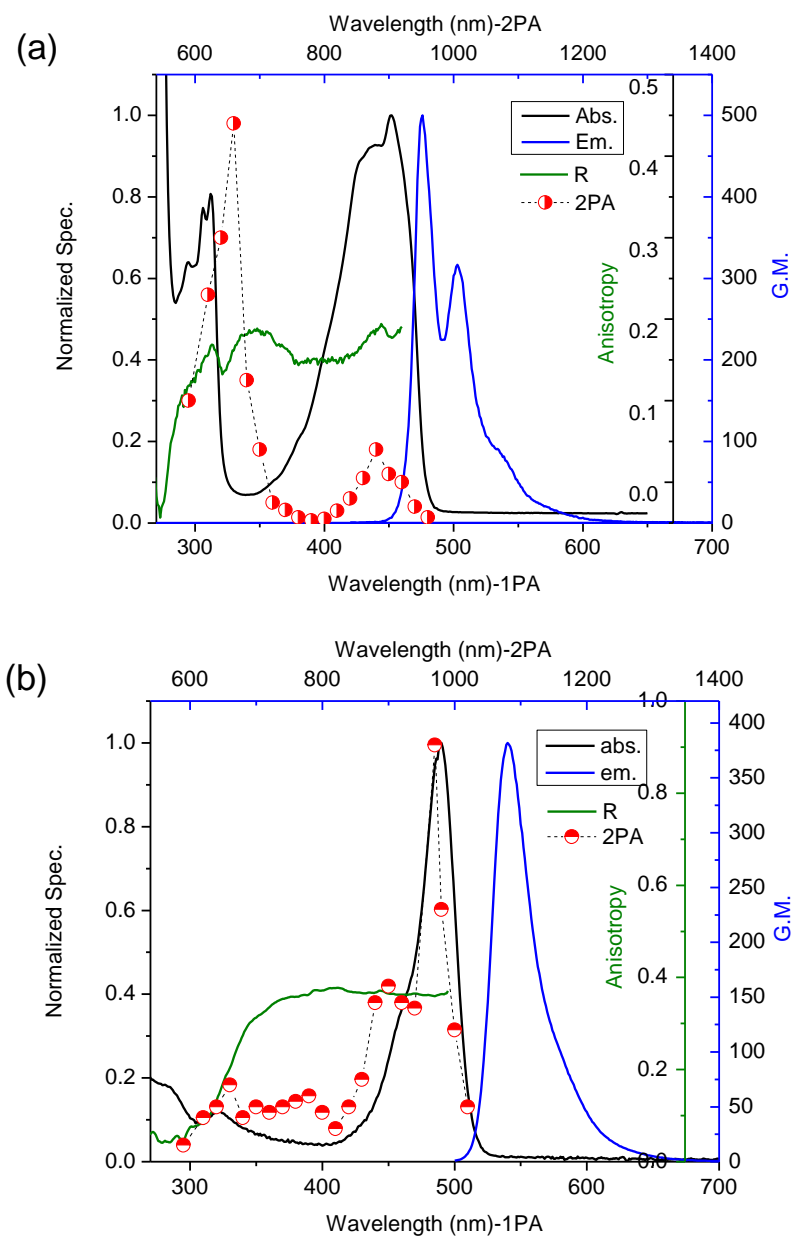


**Figure 14.** Linear and nonlinear optical spectra of (a) compound **20** and (b) **4BM-66**. In each graph, the absorption spectrum is a black line, the emission spectrum is a blue line, anisotropy is green, and two-photon absorption (2PA) cross section showed as half-filled red circle, respectively.

## Cytotoxicity

A Chinese hamster ovary (CHO) cell line was used for cell viability estimation based on measuring the MTS-formazan absorbance on a plate reader.<sup>23</sup> The MTS-formazan absorbance wavelength was observed at 538 nm (not the typical 490 nm) due to overlap with the absorbance of the sample. Hydrogen peroxide was used to induce oxidative stress.<sup>24</sup> Since the concentration of hydrogen peroxide is critical in cell viability, the cytotoxicity of hydrogen peroxide was measured, as shown in Figure 15. Cell viability was reasonable until 100  $\mu\text{M}$  of  $\text{H}_2\text{O}_2$  and the damage increased rapidly, consistent with a previous report.<sup>24</sup> When the concentration of  $\text{H}_2\text{O}_2$  reached 500  $\mu\text{M}$ , the cell viability was less than 10%.

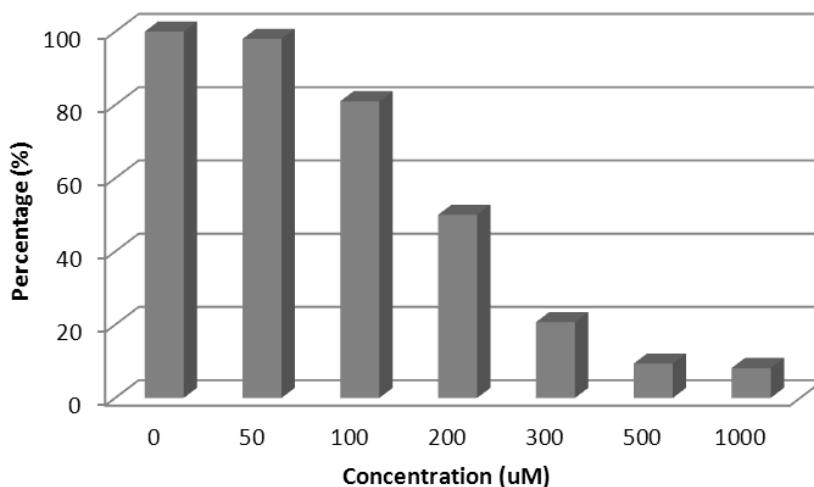


**Figure 15.** Cell viability evaluation as a function of  $\text{H}_2\text{O}_2$  concentration.

Compounds **19** and **20** were used to prepare micelle mixtures using 2 wt% of surfactant for solubility and biocompatibility. The samples were filtered before used. Cell viability using

micellular mixtures of **19** and **20** can be seen in Figure 16 (a), and was above 90% at concentrations up to 50  $\mu\text{M}$ . Interestingly, at some concentrations of nitroxide **19**, up to 20  $\mu\text{M}$ , enhanced cell viability was observed, as the nitroxide may serve as an antioxidant.

The use of the nitroxide compounds as an oxidative stress probe was then investigated. After oxidative stress was generated by 100  $\mu\text{M}$  of  $\text{H}_2\text{O}_2$  for 1 h, nitroxide **19** was added and cell viability was determined. Cell viability decreased by up to 25%. Up to 50  $\mu\text{M}$  concentration of **19** cell viability above 80%. Therefore, cell viability is generally not a problem for nitroxide **19** but one needs to empirically determine the optimal concentration.

Compounds **47** and **66** were used after dissolving in ultrapure water followed by filtration before use. Figure 16 (b) illustrates the cell viability using these two probes. Nitroxide **47** exhibited a similar trend as **19** in which the cell viability remained high and even boosted the cell growth at low nitroxide concentration. The threshold for **47** and **66** appeared to be reached with use of 100  $\mu\text{M}$  of  $\text{H}_2\text{O}_2$  to generate oxidative stress. Above the threshold, the two compounds exhibited a synergistic effect to destroy cells such that the apparent toxicity increased up to 50%. From these experiments, it was determined that 20  $\mu\text{M}$  of **47** and 100  $\mu\text{M}$  of  $\text{H}_2\text{O}_2$  can be used for cell culture (to maintain  $\sim 80\%$  cell viability within experimental error range). Compound **66**, the NOME analog of **47**, was relatively toxic to the CHO cells. Hence, only 5  $\mu\text{M}$  of dye can likely be utilized.

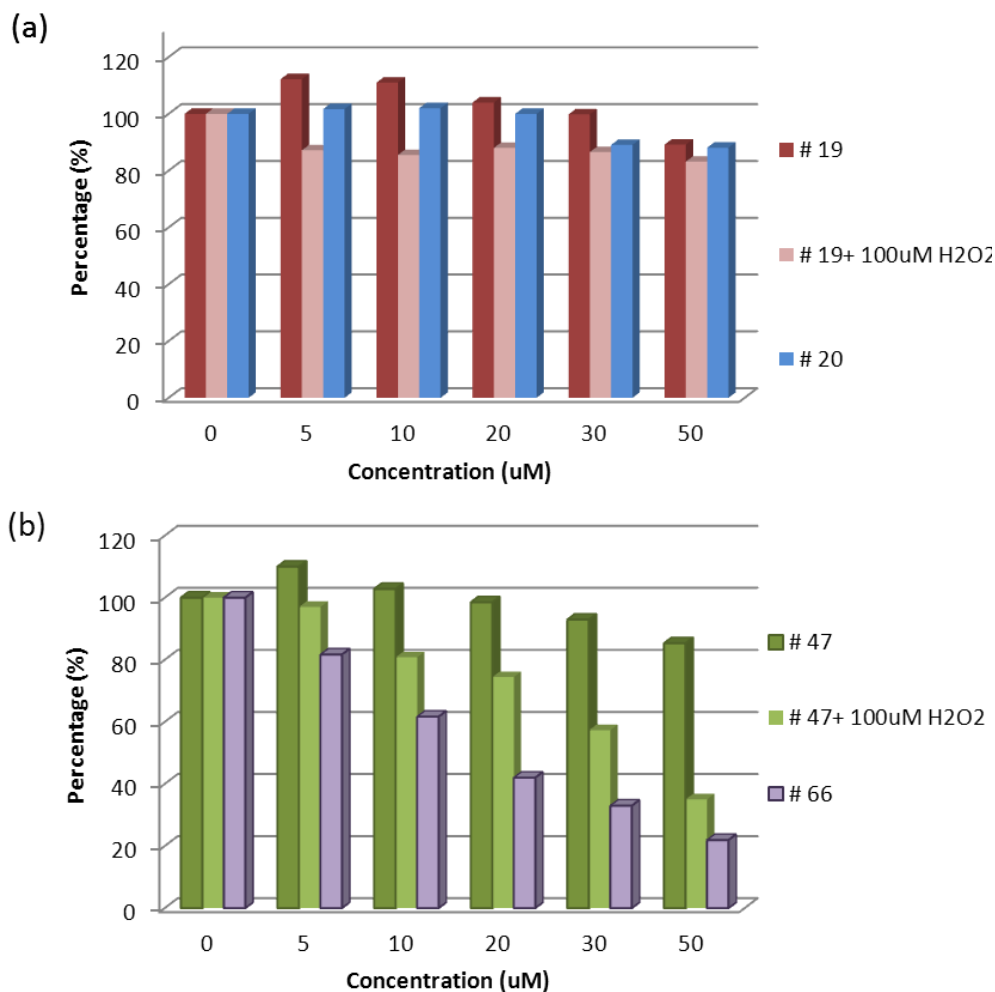


**Figure 16.** Comparative cell viability of (a) nitroxide **19**, **19** + 100 μM of H<sub>2</sub>O<sub>2</sub>, and NOME analog **20**, and (b) nitroxide **47**, **47** + 100 μM of H<sub>2</sub>O<sub>2</sub>, and NOME analog **66**.

### 1PFM and 2PFM Images

Based on the cell viability results described above along with luminescence quantum yields and 2PA cross sections, 5 μM and 10 μM of the concentration of nitroxides **19** and **4BF-47** were selected for demonstration as a two-photon fluorescent oxidative stress indicator.

Nitroxides **19** and **4BF-47** were incubated in CHO cells for 2 h. We now needed to determine if, when incubated in CHO cells after induction of oxidative stress, can fluorescence signal be observed that will be presumably from the NOR adduct (since the NOME analog has generally high fluorescence quantum yield and the profluorescent nitroxide is essentially nonfluorescent). Figure 17 shows the one-photon fluorescence microscopy (1PFM) images of CHO cells incubated with nitroxide **19**. The first row is the comparison of (a) the control (0  $\mu\text{M}$  of **19** and 0  $\mu\text{M}$   $\text{H}_2\text{O}_2$ ) vs. (b) 5  $\mu\text{M}$  of **19** and (c) 10  $\mu\text{M}$ . As anticipated, when the concentration increased, the observed fluorescence increased. The second row represents a combination of the dye concentration and oxidative stress inducer ( $\text{H}_2\text{O}_2$ ) concentration. When the  $\text{H}_2\text{O}_2$  concentration was increased from 100  $\mu\text{M}$  (d) to 200  $\mu\text{M}$  (e) with 5  $\mu\text{M}$  of nitroxide concentration, the fluorescence intensity was much greater with the higher  $\text{H}_2\text{O}_2$  concentration. This trend also held with the higher nitroxide concentration (10  $\mu\text{M}$ ) of the dye with 100  $\mu\text{M}$   $\text{H}_2\text{O}_2$  (f) and 200  $\mu\text{M}$   $\text{H}_2\text{O}_2$  (g). These results support reaction of species generated by  $\text{H}_2\text{O}_2$  with profluorescent nitroxide probe **19**, generating fluorescent NOR analogs (analogous similar to **20**) that are visualized by 1PFM via an increase in fluorescence.

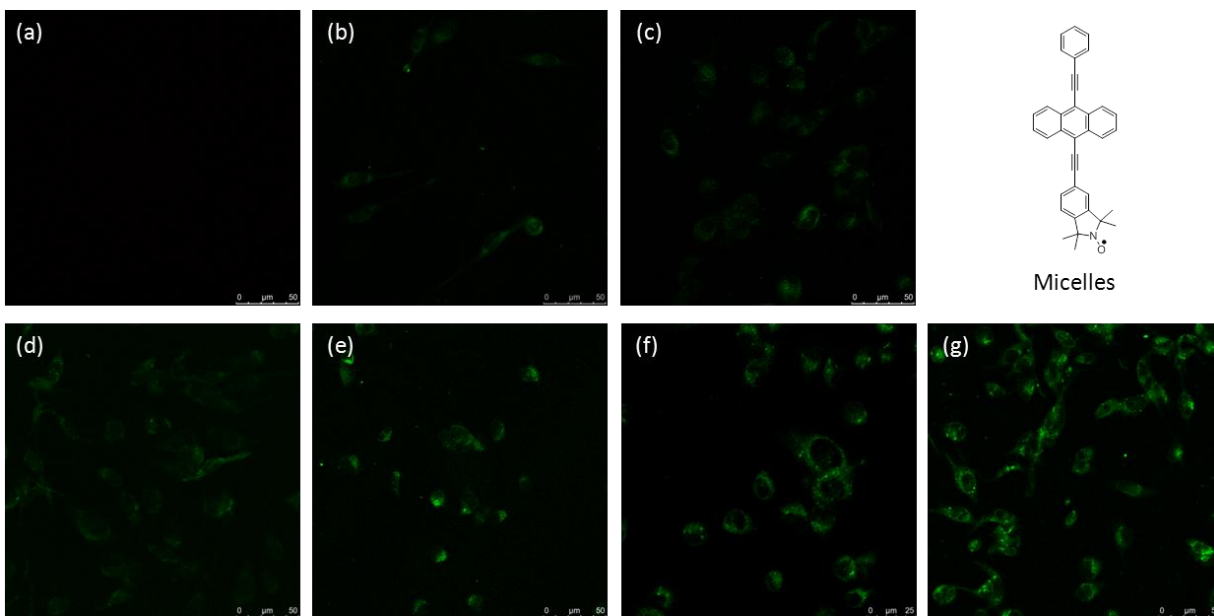


**Figure 17.** 1PFM image using nitroxide **19** and CHO cells (a) control (0  $\mu\text{M}$  of **19** and 0  $\mu\text{M}$   $\text{H}_2\text{O}_2$ ), (b) 5  $\mu\text{M}$  of **19**, (c) 10  $\mu\text{M}$  of **19**, (d) 5  $\mu\text{M}$  **19** + 100  $\mu\text{M}$  of  $\text{H}_2\text{O}_2$ , (e) 5  $\mu\text{M}$  of **19** + 200  $\mu\text{M}$  of  $\text{H}_2\text{O}_2$ , (f) 10  $\mu\text{M}$  of **19** + 100  $\mu\text{M}$  of  $\text{H}_2\text{O}_2$ , (g) 10  $\mu\text{M}$  of **19** + 200  $\mu\text{M}$  of  $\text{H}_2\text{O}_2$ .

The trend observed for nitroxide **19** was observed for nitroxide **47**, as shown in Figure 18. The fluorescence intensity increased at higher probe concentration and higher levels of oxidative stress. Even though the fluorescence quantum yield of nitroxide **47** is significantly higher than nitroxide **19**, the difference in the fluorescence quantum yields of nitroxide **47** and the corresponding NOME analog **66** is sufficient and clearly evident in Figure 18 (compare (b) with (d) and (e) or (c) with (f) and (g)), depending on the  $\text{H}_2\text{O}_2$  inducer concentration.

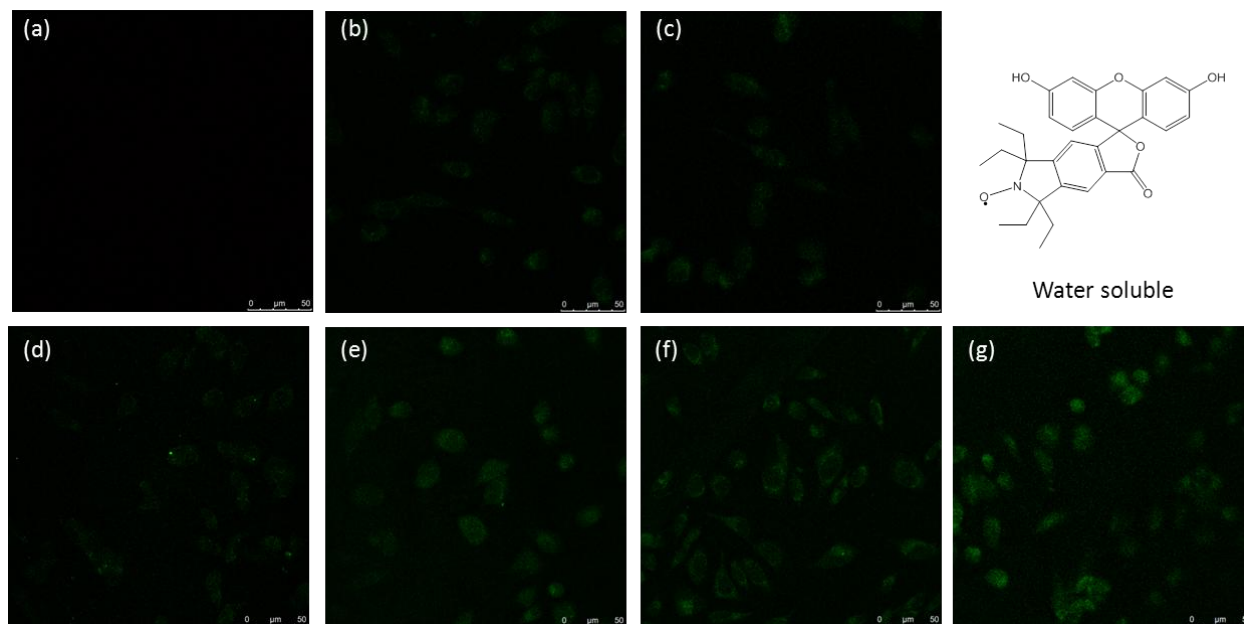


**Figure 18.** 1PFM imaging with nitroxide **47** and CHO cells (a) control (0  $\mu$ M of **19** and 0  $\mu$ M  $\text{H}_2\text{O}_2$ ), (b) 5  $\mu$ M of **47**, (c) 10  $\mu$ M of **47**, (d) 5  $\mu$ M of **47** + 100  $\mu$ M of  $\text{H}_2\text{O}_2$ , (e) 5  $\mu$ M of **47** + 200  $\mu$ M of  $\text{H}_2\text{O}_2$ , (f) 10  $\mu$ M of **47** + 100  $\mu$ M of  $\text{H}_2\text{O}_2$ , (g) 10  $\mu$ M of **47** + 200  $\mu$ M  $\text{H}_2\text{O}_2$ .

To support the oxidative stress detection ability of nitroxide **19**, a colocalization study was conducted with commercially available oxidative stress probe CellROX Deep Red reagent. 1PFM images of CHO cells co-stained with CellROX Deep Red and nitroxide **19**, shown in Figure 19, demonstrated that the localization of the presumed NOR adduct of **19** in the cells was nearly identical to CellROX Deep Red (see Figure 19 (d)). Due to the difference in absorption spectra of the two probes, there was no overlap in detecting fluorescence from CellROX Deep Red and the NOR analog(s) of **19** as this was resolved in two channels (NOR of **19**: Ex. 458 nm/Em. 500–600 nm). That is, the excitation wavelength for imaging of the NOR analogs of **19**

was 458 nm while emission was collected from 500–600 nm. Likewise, for CellROX Deep Red (Ex. 561/Em. 580–650 nm) the excitation wavelength was 561 nm and emission was collected from 580 nm to 650 nm.

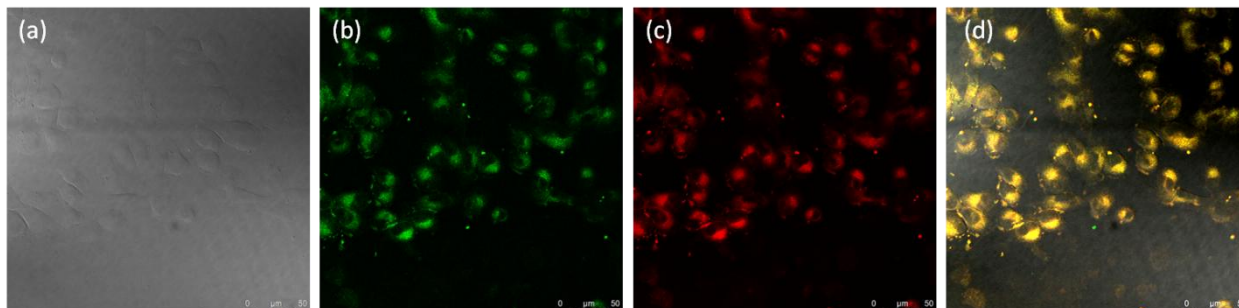


**Figure 19.** Colocalization study in CHO cells using probe **19** with commercial oxidative stress probe CellROX Deep Red (NOR analogs of **19**: Ex. 458 nm/Em. 500–600 nm, CellROX Deep Red: Ex. 561/Em. 580–650 nm), (a) DIC, (b) cells incubated with 10  $\mu$ M of **19**, (c) cells then incubated with 5  $\mu$ M of CellROX Deep Red, and (d) overlaid images of (a), (b), and (c).

A similar colocalization study was performed for nitroxide **47** and CellROX deep red, as shown in Figure 20. These results indicate good colocalization, supporting the utility of nitroxide **47** as an oxidative stress probe. For more quantitative comparison, the colocalization coefficient was calculated with ImageJ software (Mander's overlap coefficient). The presumed NOR derivatives of **19** and **47** each had colocalization coefficients of 96%.

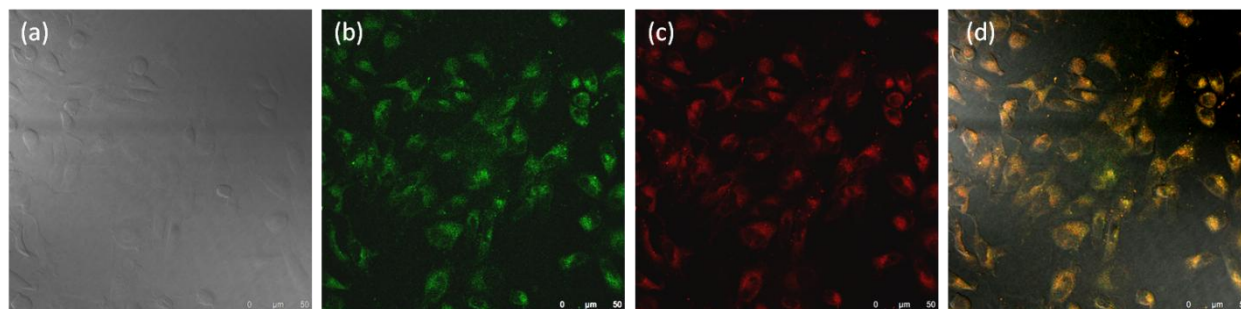


**Figure 20.** Colocalization study of nitroxide **47** in CHO cells with commercial oxidative stress probe CellROX Deep Red (Sample: Ex. 458 nm /Em. 500–600 nm, CellROX Deep Red: Ex. 561/Em. 580-650 nm), (a) DIC, (b) incubated with 20  $\mu$ M of **47**, (c) then incubated with 5  $\mu$ M of CellROX Deep Red, and (d) overlaid image of (a), (b), and (c).

These NOME analogs of **19** and **47** (**20** and **66**, respectively) had reasonable 2PA cross sections at 900 nm, a good wavelength for 2PFM due to the generally high transparency of biological materials at this wavelength. 2PFM *in vitro* cell imaging was performed to demonstrate the potential utility of these new probes for 2PFM oxidative stress imaging, as shown in Figure 21.

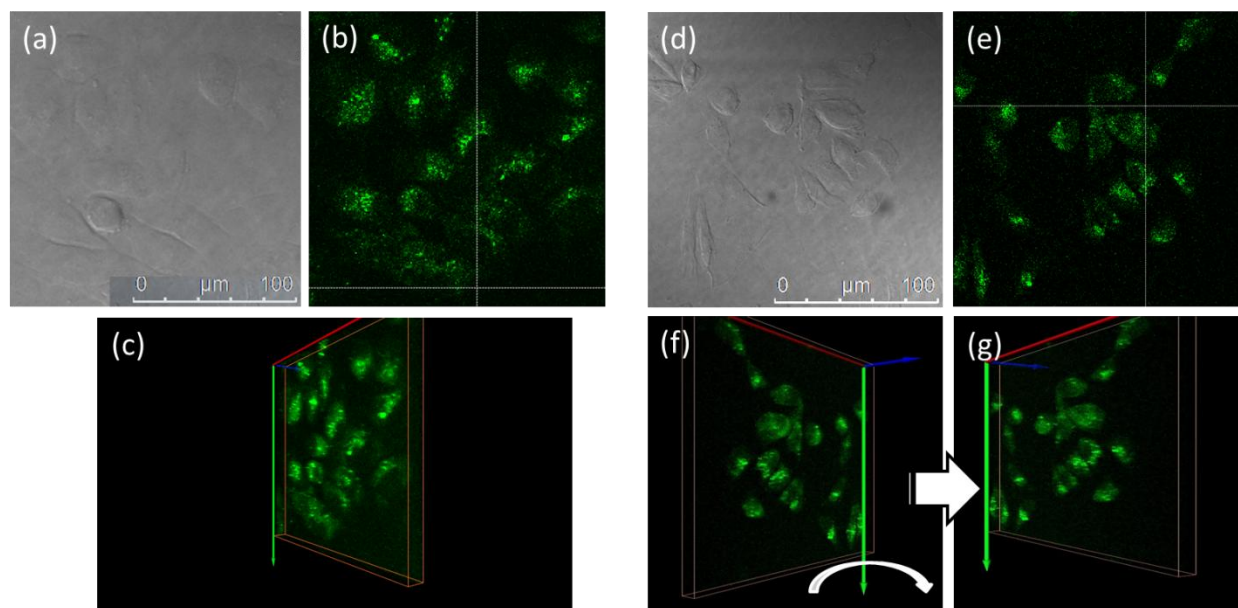


**Figure 21.** 2PFM images with fs excitation at 900 nm of CHO cells incubated with 10  $\mu\text{M}$  of **19** and 200  $\mu\text{M}$   $\text{H}_2\text{O}_2$  of (a) DIC, (b) one 2PFM XY optical slice, (c) 2PFM 3D reconstructed image, with 20  $\mu\text{M}$  of **47** and 200  $\mu\text{M}$   $\text{H}_2\text{O}_2$  (d) DIC, (e) one 2PFM XY optical slice, (f) and (g) 2PFM 3D reconstructed image.

### 3-5. Conclusion

Ten pairs of nitroxides and their NOME analogs were examined for their linear and nonlinear photophysical properties. The nitroxides exhibited profluorescent behavior, i.e., the fluorescence quantum yield was significantly higher for the NOME analogs while several displayed reasonably high 2PA cross section values above 800 nm, making them good candidates as two-photon fluorescent oxidative stress indicators. Due to their linear absorption, nonlinear absorption, and fluorescence properties, nitroxides **19** and **47** were selected for further in vitro cell studies using CHO cells. Cytotoxicity was evaluated via cell viability assays,

indicating the probes were fairly benign at concentrations suitable for fluorescence microscopy imaging. Colocalization experiments in CHO cells after induction of oxidative stress with H<sub>2</sub>O<sub>2</sub> with a commercial indicator of cellular oxidative stress, CellROX Deep Red, demonstrated very good colocalization coincidence (96%), supporting the role of the nitroxide probe as a suitable indicator of oxidative stress (damage) *in vitro*. 2PFM imaging was conducted for the first time of with a nitroxide oxidative stress probe using probes **19** and **47**. The results from this study provides impetus for the further development of this important class of materials as 2PFM oxidative stress probes, and may lead to a new NIR 2PA probe for investigating oxidative stress that has been implicated as playing important roles in diseases and conditions such as Alzheimer disease, Parkinson's disease, heart failure, and myocardial infarction.

### References

1. Stryer, L.; Griffith, H. O., A spin-labeled haptene. *Proc. Natl Acad. Sci* **1965**, 54, 1785-1791.
2. Chen, K.; Glockner, J. F.; Morse, P. D.; Swartz, H. M., Effects of oxygen on the metabolism of nitroxide spin labels in cells. *Biochemistry* **1989**, 28, (6), 2496-501.
3. Swartz, H. M.; Chen, K.; Pals, M.; Sentjurs, M.; II, P. D. M., Hypoxia- sensitive NMR contrast agents. *Magn. Reson. Med.* **1986**, 3, 169-174
4. Samunis, A.; Krishna, C. M.; Riesz, P.; Finkelstein, E.; Rusw, A., A nobel metal-free low molecular weight superoxide dismutase mimic. *Biological Chemistry* **1988**, 263, (43), 17921-17924.

5. Raju, S. V. Y.; Barouch, L. a.; Hare, J. M., Nitric oxide and oxidative stress in cardiovascular aging. *Science of aging knowledge environment : SAGE KE* **2005**, 2005, (21), re4-re4.
6. Lipman, T.; Tabakman, R.; Lazarovici, P., Neuroprotective effects of the stable nitroxide compound Tempol on 1-methyl-4-phenylpyridinium ion-induced neurotoxicity in the Nerve Growth Factor-differentiated model of pheochromocytoma PC12 cells. *European journal of pharmacology* **2006**, 549, (1-3), 50-7.
7. Varadarajan, S.; Yatin, S.; Aksenova, M.; Butterfield, D. a., Review: Alzheimer's amyloid beta-peptide-associated free radical oxidative stress and neurotoxicity. *Journal of structural biology* **2000**, 130, (2-3), 184-208.
8. Samuni, A. M.; DeGraff, W.; Cook, J. a.; Krishna, M. C.; Russo, A.; Mitchell, J. B., The effects of antioxidants on radiation-induced apoptosis pathways in TK6 cells. *Free radical biology & medicine* **2004**, 37, (10), 1648-55.
9. Mitchell, J. B.; Samuni, A.; Krishna, M. C.; DeGraff, W. G.; Ahn, M. S.; Samuni, U.; Russo, A., Biologically active metal-independent superoxide dismutase mimics. In *Biochemistry*, **1990**; Vol. 29, pp 2802-2807.
10. Mitchell, J. B.; DeGraff, W.; Kaufman, D.; Krishna, M. C.; Samuni, a.; Finkelstein, E.; Ahn, M. S.; Hahn, S. M.; Gamson, J.; Russo, a., Inhibition of oxygen-dependent radiation-induced damage by the nitroxide superoxide dismutase mimic, tempol. In *Archives of biochemistry and biophysics*, **1991**; Vol. 289, pp 62-70.

11. Bystryak, I. M.; Likhtenshtein, G. I.; Kotel'nikov, A. I.; Hankovskii, H. O.; Hideg, K., Effect of solvent molecular dynamics on the photochemical reduction of nitroxyl radicals. *Zh. Fiz. Khim.* **1986**, 60, (11), 2796-802.
12. Blough, N. V.; Simpson, D. J., Chemically mediated fluorescence yield switching in nitroxide-fluorophore adducts: optical sensors of radical/redox reactions. *Journal of the American Chemical Society* **1988**, 110, (6), 1915-1917.
13. Chen, P.; Peng, C.; Luff, J.; Spring, K.; Watters, D.; Bottle, S.; Furuya, S.; Lavin, M. F., Oxidative stress is responsible for deficient survival and dendritogenesis in purkinje neurons from ataxia-telangiectasia mutated mutant mice. *The Journal of neuroscience : the official journal of the Society for Neuroscience* **2003**, 23, (36), 11453-60.
14. Lakowicz, J. R., *Principles of Fluorescence Spectroscopy*. Third ed.; Springer: Singapore, 2006.
15. Sheik-bahae, M.; Said, A. A.; Hagan, D. J.; Van Stryland, E. W., Sensitive measurement of Optical nonlinearities using a single beam. In 1990; pp 760-9.
16. Wang, X.; Yao, S.; Ahn, H.-Y.; Zhang, Y.; Bondar, M. V.; Torres, J. A.; Belfield, K. D., Folate receptor targeting silica nanoparticle probe for two-photon fluorescence bioimaging. *Biomed. Opt. Express* **2010**, 1, (2), 11539-11544.
17. Fairfull-Smith, K. E.; Bottle, S. E., The Synthesis and Physical Properties of Novel Polyaromatic Profluorescent Isoindoline Nitroxide Probes. *European Journal of Organic Chemistry* **2008**, 2008, (32), 5391-5400.

18. Likhtenstein, G. I.; Ishii, K., Invited Review Dual Chromophore-Nitroxides: Novel Molecular Probes, Photochemical and Photophysical Models and Magnetic Materials. *Photochemistry* **2007**, (2), 871-881.
19. Makarov, N. S.; Drobizhev, M.; Rebane, A., Two-photon absorption standards in the 550-1600 nm excitation wavelength range. *Optics Express* **2008**, 16, (6).
20. Chui, C. H.; Wang, Q.; Chow, W. C.; Yuen, M. C. W.; Wong, K. L.; Kwok, W. M.; Cheng, G. Y. M.; Wong, R. S. M.; Tong, S. W.; Chan, K. W.; Lau, F. Y.; Lai, P. B. S.; Lam, K. H.; Fabbri, E.; Tao, X. M.; Gambari, R.; Wong, W. Y., 5-(Dimethylamino)-N-(4-ethynylphenyl)-1-naphthalenesulfonamide as a novel bifunctional antitumor agent and two-photon induced bio-imaging probe. *Chemical communications (Cambridge, England)* **2010**, 46, (20), 3538-40.
21. Rhodes, C. J., *Toxicology of the Unman environment: The critical role of free radicals*. Taylor & Francis: London and New York, **2000**; p 93.
22. Lakowicz, J. R., *Principles of Fluorescence Spectroscopy* **2006**, Springer.
23. Wang, X.; Nguyen, D. M.; Yanez, C. O.; Rodriguez, L.; Ahn, H.-Y.; Bondar, M. V.; Belfield, K. D., High-fidelity hydrophilic probe for two-photon fluorescence lysosomal imaging. *Journal of the American Chemical Society* **2010**, 132, (35), 12237-9.
24. DeGraff, W. G.; Krishna, M. C.; Russo, a.; Mitchell, J. B., Antimutagenicity of a low molecular weight superoxide dismutase mimic against oxidative mutagens. In *Environmental and molecular mutagenesis*, 1992; Vol. 19, pp 21-6.

## **CHAPTER 4: TWO-PHOTON EXCITED FLUORESCENCE OF A CONJUGATED POLYELECTROLYTE AND ITS APPLICATION IN CELL IMAGING**

Reproduced with permission from: Anand Parthasarathy, Hyo-Yang Ahn, Kevin D. Belfield, and Kirk S. Schanze *Applied Materials & Interfaces* **2010**, 2 (10), 2744-2748. Copyright 2010 American Chemical Society.

### **4-1. Abstract**

Two photon excited (2PE) fluorescence of a conjugated polyelectrolyte (CPE), PPESO<sub>3</sub>, was studied in methanol and in water. The photophysical and amplified quenching properties of the CPE observed by two photon excitation were comparable to the results obtained under one photon excited conditions. Two photon microscopy performed with CPE coated silica nanoparticles in HeLa cells provided images with better resolution compared to one photon microscopy, demonstrating the utility of the CPE as fluorescent probe in two photon cell imaging.

### **4-2. Introduction**

Conjugated polyelectrolytes (CPEs) combine the properties of conjugated polymers with water solubility (1). While the conjugated backbone allows efficient exciton delocalization, which forms the basis for amplified quenching (2,3), the ionic side chains afford the advantage

of processability from aqueous solution. The fluorescence of CPEs is generally quenched very efficiently by oppositely charged species such as metal ions organic ions and biomolecules (1,4). CPEs have been explored as biosensors due to their selectivity in binding specific molecules and they have found applications in optoelectronic devices (1,5-11). Recent developments in the field of CPEs have shown that this class of compounds could also serve as efficient light-activated biocidal agents (12,13).

Conjugated polymers feature non-linear optical properties and their two-photon excitation induced fluorescence has been documented by a few groups (14-31). Tailoring the properties of CPEs for two-photon absorption (2PA) is important as it could enhance their application in biological systems. The influence of solvent and the concentration dependence of two-photon absorption cross sections of conjugated polymers in organic solvents has been reported by Wang et al. (26). A recent study from Narayanan et al. describes the application of a fluorescent conjugated polymer as an efficient chemosensor for TNT under two-photon excited conditions (27). Their work combines together the phenomenon of amplified quenching of the polymer fluorescence with two-photon excitation to develop a highly sensitive sensor for TNT in the vapor phase. In the present communication, we report two-photon excited fluorescence from a water-soluble poly(phenylene ethynylene) based CPE, amplified quenching and its application to two-photon fluorescence microscopy (2PFM) imaging in HeLa cells. The photophysical properties of the CPE, PPESO<sub>3</sub>, have been studied by our group and others (32,33,34).

### **4-3. Experimental Materials and Methods**

#### **Materials.**

Silica microspheres of average diameter  $300\text{ nm} \pm 10\text{ nm}$  were purchased from Bangs Laboratories. Poly(dimethyldiallylammonium)chloride (PDDA) was purchased from Aldrich and the water soluble anionic conjugated polyelectrolyte, PPESO<sub>3</sub> was synthesized following previously reported procedure. HeLa cells were purchased from ATCC (America Type Culture Collections, Manassas, VA, USA).

#### ***Polymer Coated Silica Particles***

The polymer coated silica nanospheres were prepared using the layer-by-layer method described by Kyungkon Kim et.al.<sup>1</sup> PDDA and PPESO<sub>3</sub> were used as the polycation and the fluorescent polyanion, respectively (1 mM in water). PDDA was allowed to adsorb on the negatively charged surface of the nanospheres through electrostatic interactions. Subsequent exposure of the PDDA-coated silica nanospheres to oppositely charged PPESO<sub>3</sub> results in silica/PDDA/PPESO<sub>3</sub> spheres. Additional bilayers were deposited by successive treatments with PDDA and PPESO<sub>3</sub>. Between layer coatings, remaining unadsorbed polyelectrolytes were separated by centrifugation (3650 g) and washing with deionized water (Milli-Q, 18M $\Omega$ ).

#### **Methods**

#### ***Differential Interference Contrast Image and One-Photon Fluorescence Microscopy***

Conventional differential interference contrast (DIC) and conventional one-photon excited fluorescence (1PA) images were obtained using an inverted microscope (Olympus IX70) equipped with a QImaging cooled CCD (Model Retiga EXi) and tungsten or mercury excitation

lamps (100 W). One-photon confocal fluorescence images of the fixed cells were obtained using a custom made filter cube (Ex: 377/50; DM: 409; Em: 525/40). Both images were collected with a 60x oil immersion microscope objective (UPLANSAPO 60x, NA=1.35, Olympus).

#### *Two Photon Absorption and Imaging*

Two-photon absorption (2PA) of PPESO<sub>3</sub> in methanol and aqueous solutions were determined over a broad spectral region by the two-photon unconverted fluorescence (2PF) method relative to rhodamine B in methanol (Figures 22 and S2). A PTI QuantaMaster spectrofluorimeter coupled with a Ti:sapphire femtosecond laser (Coherent MIRA 900 with pulse duration, ~200 fs, tuning range 700–1000 nm, 76 MHz repetition rate) was used.

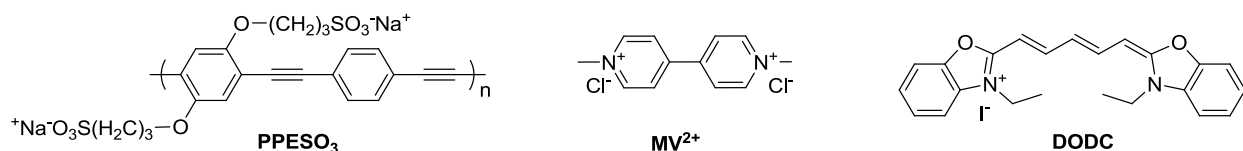
Two-photon fluorescence microscopy images were collected on a modified Olympus Fluoview FV300 microscope system coupled to the coherent MIRA Ti:sapphire laser, which is used for 2PA measurement. A short pass emission filter (FF01-694/SP-25, Semrock) was placed in the microscope scan head to avoid background irradiance from the excitation source. Consecutive layers, separated by 0.2  $\mu\text{m}$ , were recorded to create a 3D reconstruction from overlaid two-photon fluorescence images. The two-photon induced fluorescence was collected with a 60x oil immersion microscope objective (UPLANSAPO 60x, NA=1.35, Olympus).

#### **4-4. Results and Discussion**

PPESO<sub>3</sub> (Scheme 3) is an anionic polymer that is soluble both in water and alcohol and exhibits blue or green fluorescence. In methanol, the polymer shows a strong fluorescence and a well-defined 0-0 band with  $\lambda_{\text{max}} = 450 \text{ nm}$  whereas a broad, red shifted band with diminished

quantum yield is observed in water. The spectral data suggest that in water the polymer is strongly aggregated whereas in methanol, a ‘good solvent’, it exists as individual chains with minimal aggregation.

**Scheme 3.** Chemical structures of CPEs and quenchers



The two-photon absorption (2PA) of PPESO<sub>3</sub> in methanol was determined by monitoring the upconverted fluorescence, and the spectrum is shown along with the 2PA excited fluorescence spectrum in Figure 22. First, note that the 2PA excited fluorescence spectrum ( $\lambda_{\text{ex}} = 740 \text{ nm}$ ) exhibits  $\lambda_{\text{max}} = 440 \text{ nm}$ , and it is essentially identical to that observed under 1PA excitation, indicating that the emitting state produced by 2PA is the same as that produced by 1PA. The 2PA cross section was determined relative to rhodamine B in methanol; the onset of 2PA is at  $\sim 800 \text{ nm}$  and the cross section increases monotonically and reaches  $\sim 400 \text{ GM}$  at  $690 \text{ nm}$  (36). Comparing the 2PA and 1PA spectra (plotted for comparison in Figure 22) reveals that the onset of 2PA occurs to the blue of the longest wavelength  $\pi, \pi^*$  transition in the 1PA spectrum (when comparing as  $2\lambda$  for the 2PA spectrum). This is consistent with the notion that the lowest energy transition ( $1A_g \rightarrow 1B_u$ ) is one-photon allowed but two-photon forbidden; enhanced 2PA occurs on the blue side of the 1PA allowed transition and it is likely due to

absorption into the second singlet state ( $1A_g \rightarrow mA_g$ ). Similar observations have been made in the 2PA spectra of other centrosymmetric conjugated polymers (30,37).

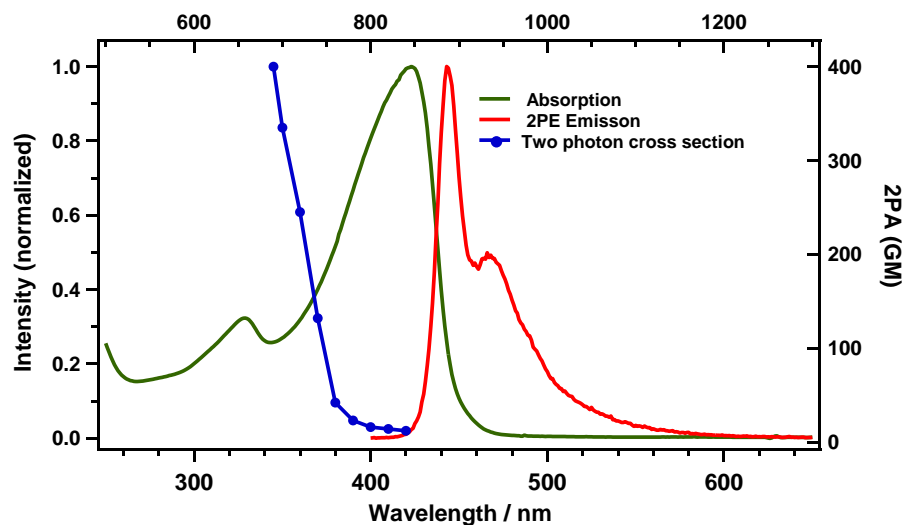


**Figure 22.** Linear and two-photon photophysical properties of PPESO<sub>3</sub> polymer in methanol (Normalized absorption spectrum (green line), normalized emission spectrum (red line), and 2PA spectrum (blue line and circle symbol)).

In order to determine if the aggregated and molecularly dissolved states of PPESO<sub>3</sub> exhibit similar fluorescence under one-photon and two-photon excitation, we examined the solvent dependence of the fluorescence spectra in methanol/water mixtures and the results are shown in Figure 23. For both 2PA and 1PA excitation (Figure 23a and 23b, respectively) it is seen that the as the volume fraction of water increases in the solvent the fluorescence intensity decreases, the spectra become broader, and undergo a significant red-shift. The response of the fluorescence to solvent is very similar for 2PA and 1PA excitation, indicating that the

photophysics of the fluorescent state, including exciton transport and trapping by aggregate states, remains the same when the polymer is excited by 2PA.

Much of the interest in conjugated polyelectrolytes is motivated by their use as fluorescent sensors that respond to analytes present at very low concentration. The sensitive fluorescence response is a result of the “amplified quenching effect” (2), whereby oppositely charged quencher ions are able to quench CPE fluorescence with Stern-Volmer quenching constants ( $K_{SV}$ ) in excess of  $10^7 \text{ M}^{-1}$ . Amplified quenching is attributed to the electrostatic interaction between oppositely charged polymer and the quencher (ion-pairing) as well as the delocalization and rapid transport of the singlet exciton over the  $\pi$ -conjugated CPE chain. In the present study we sought to determine whether the amplified fluorescence quenching properties of PPESO<sub>3</sub> are also observed when the CPE is excited by 2PA. Thus, parallel quenching studies were carried out under 1PA and 2PA excitation using PPESO<sub>3</sub> and the cationic electron transfer quencher methylviologen ( $MV^{2+}$ ) and cationic cyanine dye energy transfer quencher (DODC).

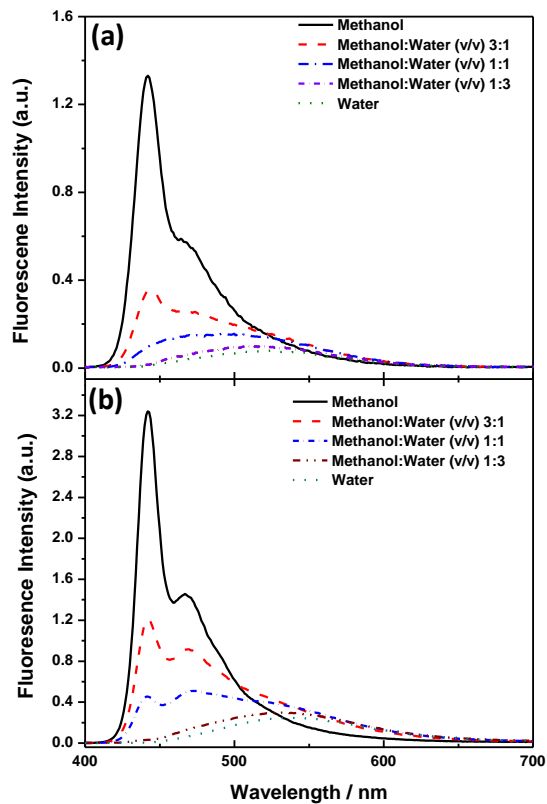


**Figure 23.** Fluorescence spectra of 10  $\mu\text{M}$  PPESO<sub>3</sub> in varying proportions of methanol and water at (a)  $\lambda_{\text{ex}} = 740$  nm and (b)  $\lambda_{\text{ex}} = 380$  nm (bottom).

Thus, parallel quenching studies were carried out under 1PA and 2PA excitation using PPESO<sub>3</sub> and the cationic electron transfer quencher methyl viologen ( $\text{MV}^{2+}$ ) and cationic cyanine dye energy transfer quencher (DODC).

The Stern-Volmer fluorescence quenching of PPESO<sub>3</sub> ( $c = 10 \mu\text{M}$ ) by  $\text{MV}^{2+}$  under 1PA and 2PA excitation gave rise to similar results (see Figure S-2 in supporting information). At low  $[\text{MV}^{2+}]$  ( $< 2 \mu\text{M}$ ) the SV plots are nearly linear, and the  $K_{\text{SV}}$  values are  $3.8 \times 10^{-6}$  and  $3.0 \times$

$10^{-6} \text{ M}^{-1}$  under 2PA and 1PA excitation, respectively. In both cases at higher  $[\text{MV}^{2+}]$  the SV plots show upward curvature, and the observed quenching efficiency was slightly larger under 2PA excitation. Overall, however, the results indicate that the amplified quenching effect is clearly active when PPESO<sub>3</sub> is excited by 2PA; this result shows that the CPE could be used in sensing schemes with infrared excitation.

We also examined quenching of PPESO<sub>3</sub> by the energy acceptor DODC. The dye was selected because in previous work we have shown that dye quenches by a fluorescence resonance energy transfer (FRET) mechanism, and consequently the polymer can be used to sensitize the dye fluorescence (33). As shown in the supporting information (Figure S-3), addition of DODC results in very efficient quenching of the PPESO<sub>3</sub> fluorescence under 2PA excitation, with  $K_{\text{SV}} \sim 2.5 \times 10^6 \text{ M}^{-1}$ , which is slightly larger than observed under 1PA excitation ( $K_{\text{SV}} \sim 1.5 \times 10^6 \text{ M}^{-1}$ ). Interestingly, we also compared the ability of PPESO<sub>3</sub> to sensitize the DODC fluorescence under 1- and 2PA excitation, and the results are shown in Figure 24. Here it is seen that addition of a low concentration of DODC results in quenching of the PPESO<sub>3</sub> fluorescence with concomitant increase of fluorescence from the DODC at longer wavelength ( $\lambda \sim 640 \text{ nm}$ ). While the intensity of the sensitized fluorescence is somewhat weaker under 2PA excitation, the control experiments show that near-infrared excitation (740 nm) of DODC in the absence of PPESO<sub>3</sub> results in virtually no up-converted fluorescence. This result indicates that the PPESO<sub>3</sub> can act as a relatively efficient “two-photon” upconverting sensitizer. It is likely that this 2PA FRET sensitizing scheme will apply to other cationic dyes that are able to effectively associate with the anionic CPE in solution. In addition, since a number of CPE sensor schemes are based on FRET

to an ion-paired dye, the result suggests that these sensors may operate under 2PA excitation using near-infrared photons.

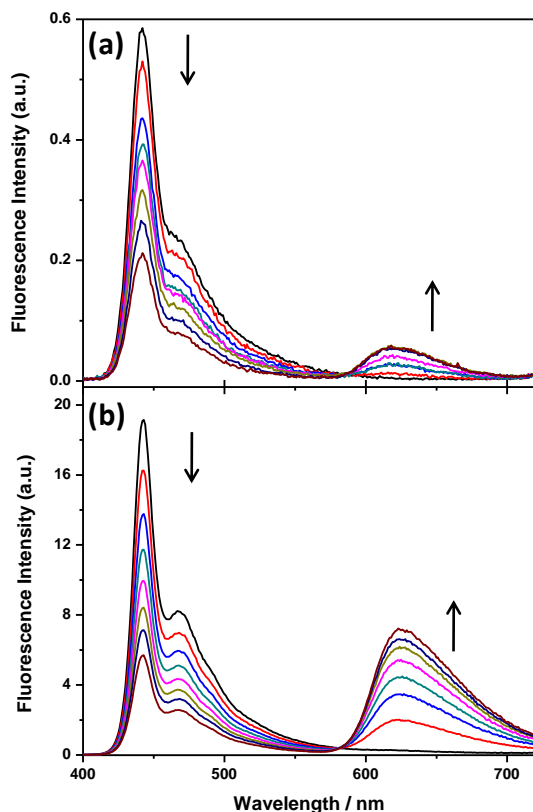


**Figure 24.** Fluorescence quenching of PPESO<sub>3</sub> (10  $\mu$ M in methanol) by DODC [0.1 – 10  $\mu$ M] at

(a)  $\lambda_{\text{ex}} = 740$  nm and (b)  $\lambda_{\text{ex}} = 380$  nm.

One important application of 2PA excited fluorescence lies in its utility in cellular imaging by two-photon fluorescence microscopy (2PFM). Given that the fluorescence of PPESO<sub>3</sub> can be excited efficiently in the near-infrared by 2PA, we set out to demonstrate that the polymer could be used for intracellular imaging. Thus, PPESO<sub>3</sub> coated silica nanoparticles (300

nm) were fabricated by using the layer-by-layer technique as described previously (35). HeLa cells were incubated with the PPESO<sub>3</sub> coated particles (20 µg/mL for 2 h), and the labeled cells were subsequently imaged by using differential interference contrast (DIC), and one-photon and two-photon excited fluorescence microscopy (1PFM and 2PFM, respectively, see Figure 25) (38).

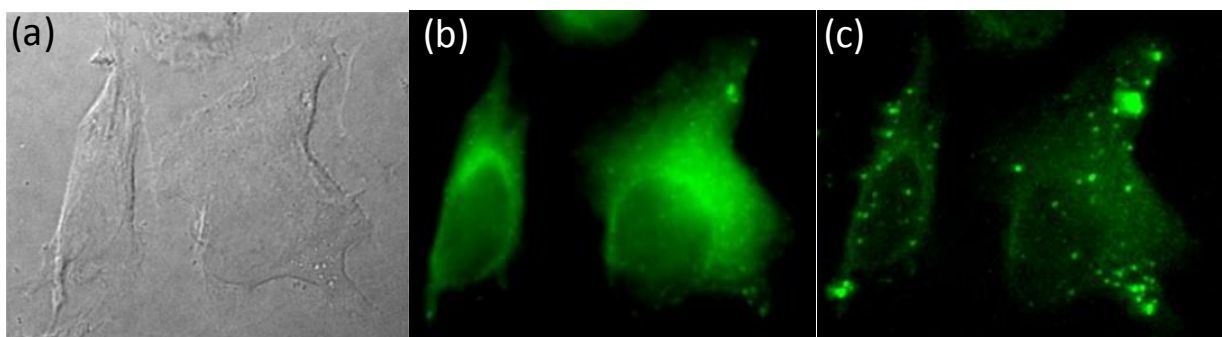


**Figure 25.** Images of HeLa cells incubated with PPESO<sub>3</sub> silica nanoparticle (20 µg/mL, 2 h). (a) DIC, exposure time 20 ms, (b) 1PFM image, 130 ms (filter cube Ex: 377/50 DM: 409 Em: 525/40), and (c) one layer of 2PFM image (Ex: 750 nm; Power: 30 mW).

As seen in Figure 25c, 2PFM images of the stained HeLa cells ( $\lambda_{\text{ex}} = 750$  nm) feature bright fluorescence from the polymer coated silica particles present in the cell. Comparison of the images in Figure 25b and 25c makes it clear that the 2PFM images provide considerably improved contrast and spatial resolution compared those obtained by 1PFM; indeed, it is possible to detect the emission from individual PPESO<sub>3</sub> coated nanoparticles in the 2PFM images (Figure 25c). Inspection of the image reveals single particles as well as aggregates, and the particles appear to be preferentially localized in endosomes in the cytosolic region of the cell. As shown in the supporting information, a 3D reconstruction of the cell image is possible (Figure S5).

#### **4-5. Conclusion**

In summary, we have demonstrated that the anionic CPE based PPESO<sub>3</sub> exhibits moderately strong 2PA in the near infrared region, with an onset at *ca.* 800 nm. The absorption is shifted blue relative to the lowest allowed 1PA transition, indicating that the 2PA excites the polymer into the second singlet state which is forbidden in the 1PA spectrum. The photophysical and amplified quenching properties of the polymer are essentially identical under 1PA and 2PA, indicating that the same fluorescent state is populated via 2PA. We demonstrated that the polymer can serve as a two-photon sensitizer for a long wavelength emitting cyanine dye, as well as its application in cellular imaging using two-photon excited fluorescence microscopy. These studies provide the blueprint for application of poly(phenylene ethylene) based CPEs as sensors, fluorescent imaging agents, and singlet oxygen sensitization with near-infrared excitation.

#### **References**

- (1) Jiang, H.; Taranekar, P.; Reynolds, J. R.; Schanze, K. S. *Angew. Chem., Int. Ed.* **2009**, *48*, 4300-4316.
- (2) Zhou, Q.; Swager, T. M. *J. Am. Chem. Soc.* **1995**, *117*, 12593-12602.
- (3) Chen, L.; McBranch, D. W.; Wang, H.-L.; Helgeson, R.; Wudl, F.; Whitten, D. G. *Proc. Natl. Acad. Sci.* **1999**, *96*, 12287-12292.
- (4) Duan, X.; Liu, L.; Feng, F.; Wang, S. *Acc. Chem. Res.* **2010**, *43*, 260-270.
- (5) Wang, D.; Gong, X.; Heeger, P. S.; Rininsland, F.; Bazan, G. C.; Heeger, A. J. *Proc. Natl. Acad. Sci.* **2002**, *99*, 49-53.
- (6) Feng, F.; He, F.; An, L.; Wang, S.; Li, Y.; Zhu, D. *Adv. Mater.* **2008**, *20*, 2959-2964.

- (7) Hoven, C. V.; Garcia, A.; Bazan, G. C.; Nguyen, T.-Q. *Adv. Mater.* **2008**, *20*, 3793-3810.
- (8) Jin, Y.; Bazan, G. C.; Heeger, A. J.; Kim, J. Y.; Lee, K. *Appl. Phys. Lett.* **2008**, *93*, 123304/1-123304/3.
- (9) Park, J.; Hoven, C. V.; Yang, R.; Cho, N.; Wu, H.; Nguyen, T.-Q.; Bazan, G. C. *J. Mater. Chem.* **2009**, *19*, 211-214.
- (10) Seo, J. H.; Gutacker, A.; Walker, B.; Cho, S.; Garcia, A.; Yang, R.; Nguyen, T.-Q.; Heeger, A. J.; Bazan, G. C. *J. Am. Chem. Soc.* **2009**, *131*, 18220-18221.
- (11) Seo, J. H.; Namdas, E. B.; Gutacker, A.; Heeger, A. J.; Bazan, G. C. *Appl. Phys. Lett.* **2010**, *97*, 043303/1-043303/3.
- (12) Corbitt, T. S.; Ding, L.; Ji, E.; Ista, L. K.; Ogawa, K.; Lopez, G. P.; Schanze, K. S.; Whitten, D. G. *Photochem. Photobiol. Sci.* **2009**, *8*, 998-1005.
- (13) Corbitt, T. S.; Sommer, J. R.; Chemburu, S.; Ogawa, K.; Ista, L. K.; Lopez, G. P.; Whitten, D. G.; Schanze, K. S. *ACS Appl. Mater. Interfaces* **2009**, *1*, 48-52.
- (14) Hua, J. L.; Li, B.; Meng, F. S.; Ding, F.; Qian, S. X.; Tian, H. *Polymer* **2004**, *45*, 7143-7149.
- (15) *Nonlinear Optical Effects in Organic Polymers*; Messier, J.; Kajzar, F.; Prasad, P.; Ulrich, D., Eds.; Kluwer: Dordrecht, 1989.
- (16) Correa, D. S.; Cardoso, M. R.; Goncalves, V. C.; Balogh, D. T.; De Boni, L.; Mendonca, C. R. *Polymer* **2008**, *49*, 1562-1566.
- (17) Stabo-Eeg, F.; Lindgren, M.; Nilsson, K. P. R.; Inganaes, O.; Hammarstroem, P. *Chem. Phys.* **2007**, *336*, 121-126.

- (18) Schroeder, R.; Graupner, W.; Scherf, U.; Ullrich, B. *J. Chem. Phys.* **2002**, *116*, 3449-3454.
- (19) Belfield, K. D.; Yao, S.; Bondar, M. V. *Adv. Polym. Sci.* **2008**, *213*, 97-156.
- (20) Yamamoto, T.; Kumagai, A.; Saito, K.; Nagai, T. *J. Nanosci. Nanotechnol.* **2009**, *9*, 670-672.
- (21) Hildner, R.; Lemmer, U.; Scherf, U.; Koehler, J. *Chem. Phys. Lett.* **2007**, *448*, 213-217.
- (22) Yang, Z.; Li, N.; Xia, A.-d.; He, Q.-g.; Lin, H.-Z.; Bai, F.-l. *Chin. J. Chem. Phys.* **2007**, *20*, 500-508.
- (23) Wu, C.; Szymanski, C.; Cain, Z.; McNeill, J. *J. Am. Chem. Soc.* **2007**, *129*, 12904-12905.
- (24) Tian, N.; Xu, Q.-H. *Adv. Mater.* **2007**, *19*, 1988-1991.
- (25) Sohn, Y.; Richter, J.; Ament, J.; Stuckless, J. T. *Appl. Phys. Lett.* **2004**, *84*, 76-78.
- (26) Wang, H.; Li, Z.; Shao, P.; Qin, J.; Huang, Z.-l. *J. Phys. Chem. B* **2010**, *114*, 22-27.
- (27) Narayanan, A.; Varnavski, O. P.; Swager, T. M.; Goodson, T., III *J. Phys. Chem. C* **2008**, *112*, 881.
- (28) Screen, T. E. O.; Thorne, J. R. G.; Denning, R. G.; Bucknall, D. G.; Anderson, H. L. *J. Am. Chem. Soc.* **2002**, *124*, 9712-9713.
- (29) Pollagi, T. P.; Stoner, T. C.; Dallinger, R. F.; Gilbert, T. M.; Hopkins, M. D. *J. Am. Chem. Soc.* **1991**, *113*, 703-4.
- (30) Baker, C. J.; Gelsen, O. M.; Bradley, D. D. C. *Chem. Phys. Lett.* **1993**, *201*, 127-31.
- (31) Takahashi, M.; Yamada, S.; Matsuda, H.; Nakanishi, H.; Tsuchida, E.; Nishide, H. *Chem. Commun.* **1997**, 1853-1854.
- (32) Tan, C.; Pinto Mauricio, R.; Schanze Kirk, S. *Chem. Commun.* **2002**, 446-7.

- (33) Tan, C.; Atas, E.; Mueller, J. G.; Pinto, M. R.; Kleiman, V. D.; Schanze, K. S. *J. Am. Chem. Soc.* **2004**, *126*, 13685-13694.
- (34) Zhang, T.; Fan, H.; Zhou, J.; Liu, G.; Feng, G.; Jin, Q. *Macromolecules* **2006**, *39*, 7839-7843.
- (35) Kim, K.; Webster, S.; Levi, N.; Carroll, D. L.; Pinto, M. R.; Schanze, K. S. *Langmuir* **2005**, *21*, 5207-5211.
- (36) The scan range was limited by the tuning range of the Ti: Sapphire laser system.
- (37) Harrison, M. G.; Urbasch, G.; Mahrt, R. F.; Giessen, H.; Bassler, H.; Scherf, U. *Chem. Phys. Lett.* **1999**, *313*, 755-762.
- (38) Parallel studies were carried out by incubating the HeLa cells with PPESO<sub>3</sub> and the imaging results of the resulting cells are shown in supporting information (Figure S4).

## CHAPTER 5: ENHANCEMENT OF J-AGGREGATION OF POLYMER-TEMPLATED SELF ASSEMBLED PORPHYRIN-BASED DYES

### 5-1. Abstract

Supramolecular structures based on organized assemblies of macrocyclic chromophores, particularly porphyrin-based dyes, have attracted widespread interest as molecular devices with potential applications in molecular electronics, artificial light harvesting, and pharmacology. We report the formation of J-aggregates of two porphyrin-based dyes, 5,10,15,20-tetrakis(4-sulfonatophenyl)porphyrin (TPPS, **4**) and an amino tris-sulfonate analog (**5**) in water using a functionalized norbornene-based homopolymer, synthesized by the ring opening metathesis polymerization technique. The polymer template enhanced J-aggregation of the porphyrin dyes, exploiting the ionic interaction of the cationic side chains (tertiary amino groups) of the polymer under acidic conditions with the negatively charged sulfonate groups of the dyes. The J-aggregation behavior was investigated by UV-vis, fluorescence, and lifetime decay studies. The two-photon absorption (2PA) cross section was found to be ca. an order of magnitude higher for the J-aggregated TSPP relative to the free base TSPP. Finally, the 2PA cross section of the polymer-templated TSPP J-aggregate was determined and found to be up to three times higher than the J-aggregated TSPP itself, suggesting a role of polymer-templating to facilitate porphyrin aggregation and modulate 2PA.

## **5-2. Introduction**

Supramolecular structures based on organized assemblies/aggregation of macrocyclic chromophores have attracted widespread interest as molecular devices with potential applications in molecular electronics, artificial light harvesting and pharmacology. In the late 1930s, Gunter Scheibe<sup>2</sup> and Edwin E. Jelly<sup>3</sup> independently first discovered the phenomenon of J and H aggregation for cyanine-based dyes. Among the aggregates, J-aggregation (side-by-side) and H-aggregation (face-to-face) have been well-studied and are characterized by strong, narrow, red-shifted absorption bands (J) and blue shifted absorption bands (H) with respect to its monomeric form. Aggregation, driven largely by non-covalent interactions, causes remarkable changes in the optical and electronic properties of the molecular aggregates. Strong intermolecular interactions between the dyes and delocalized excitonic energy over the whole assembly of the aggregate are characteristic of this phenomenon. Kasha *et al.*<sup>4</sup> proposed the following equation to explain the dipole–dipole coupling interaction energy (V) in aggregates:

$$V = -\frac{M^2}{r^3}(1 - 3\cos^2\theta) \quad (6)$$

where M is the transition dipole moment, r is the distance from center-center between dipoles, and  $\theta$  represents the geometrical factor related to mutual inclination of the aligned monomers.

Among the known molecular building blocks, porphyrins constitute a highly attractive class of “synthons” for functional nanomaterials due to their unique photonic and electronic properties, specifically for their potential applications in PDT, nonlinear optics, and for investigation of artificial light harvesting systems that mimic natural photosynthetic receptors. 5,10,15,20-Tetrakis(4-sulfonatophenyl)porphyrin (TPPS, **4**) is, perhaps, one of the most studied

synthetic porphyrins. Under acidic aqueous conditions (usually pH <1), the diacid species of the TPPS porphyrin, forms J-aggregates due to hydrophobic  $\pi$ - $\pi$  stacking and electrostatic interaction between the anionic sulfonated phenyl group and the cationic core. The tuning factors of porphyrin aggregation in aqueous solution vary depending on the porphyrin structure and concentration, as well as the pH, ionic strength,<sup>5</sup> and counterions of inorganic salts in the media. Also, the medium, such as copolymer micelles,<sup>6,7</sup> ionic liquids,<sup>8</sup> nucleic acids, polypeptides, proteins, and carbon nanotubes, is capable of influencing porphyrin aggregation behavior.

Investigation of polymer based self-assembled J-aggregation of the dyes is of recent interest. Santoro *et al.* demonstrated that the tetraanionic meso-tetrakis(4-sulfonatophenyl)porphine (H<sub>2</sub>TPPS) in the pH range 5-12 exists in a monomeric form, and its fluorescence is not pH-dependent.<sup>54</sup> However, in the presence of polylysine, absorption, circular dichroism, and resonant light scattering data indicate extensive polymer-induced self-aggregation of the porphyrins. In particular, at low pH (<7), the protonated polylysine promotes porphyrin binding and self-aggregation with consequent strong quenching of their fluorescence.<sup>9</sup> Periasamy *et al.* observed that poly-(L, D, or DL)-lysine, depending on optical chirality, induced J-aggregation of TPPS more efficiently than monomeric lysine. Only micromolar concentrations of polylysine was required for complete conversion of the porphyrin monomer to its J-aggregate.<sup>10</sup> Quite impressively, Whitten *et al.* demonstrated ‘superquenching’ of polyelectrolytes containing cyanine pendant polylysines (repeat unit: 1-900) both in solution and after adsorption onto silica nanoparticles. The self-assembled polymer-initiated surface activated quenching led to formation of J-aggregates due to enhanced binding with increasing number of repeating unit of the polymers.<sup>11</sup> Also, laponite clay behaved similarly with cyanine dyes to induce J-aggregation.<sup>12</sup>

Zhao *et al.* recently reported the micellization of poly(ethylene glycol)-block-poly(4-vinylpyridine) (PEG114-b-P4VP61) induced by TPPS in acidic solution where the core contained TPPS/PV4P and the shell was structured with PEG. TPPS formed aggregates in the micellar core to form J-aggregates and H-aggregates, respectively, at pH 1.5-2.5 and 3.0-4.0.<sup>7</sup> Kano *et al.* found that the TPPS-acid form was stabilized to induce J-aggregation by binding with ferric myoglobin (metMb) in water at neutral pH due to encapsulation and fixation by the relatively rigid protein molecules. The hydrophobic core of the J-aggregate caused the deformation of the secondary structure of the metMb, and, thus, denaturation of the protein.<sup>13</sup> Chmelka *et al.* reported that mesostructured silica-block copolymer thin films provided orientationally-ordered host matrixes for stable alignment of co-assembled porphyrin J-aggregates with anisotropic optical properties.<sup>14</sup> Smith *et al.* reported the induction of J- and H-aggregation of TPPS by the cationic polyelectrolyte, poly(diallyldimethylammonium chloride) (PDDA) on films deposited on Si. The films were made by dipping in alternating aqueous solutions containing film components (layer-by-layer deposition).<sup>15</sup> There is obviously substantial interest in inducing and controlling porphyrin aggregation.

Herein, our main focus is to determine whether a functional copolymer can serve as the foundation to build a supramolecular structure containing a porphyrin-based dye and facilitating J-aggregation. Of particular interest is the potential enhancement of two-photon absorption by J-aggregates relative to the corresponding unaggregated monomers. We report the synthesis and characterization of a norbornene-based monomer, containing dimethylamino pendant groups, and the corresponding homopolymer by ring opening metathesis polymerization (ROMP). ROMP was selected for its tolerance to a variety of functional groups and the ability to control

molecular weight. J-aggregation of two porphyrin-based dyes, commercial TSPP (**4**) and a synthetic analog (**5**), in acidic aqueous solution was investigated with and without presence of the homopolymer template. The aggregation properties were evaluated by UV-vis absorption, fluorescence spectroscopy, and fluorescence lifetime decay studies, clearly demonstrating J-aggregation was more pronounced in dyes in the presence of the polymer, possibly due to enhanced stabilization of the anionic dye's periphery by the cationic nature of the siderophore ( $\text{-NHMe}_2^+$ ) of the polymers at low pH. Finally, two-photon absorption was determined for free (unaggregated) and aggregated (with and without the polymer template).

### **5-3. Experimental Materials and Methods**

#### **Materials**

5,10,15,20-Tetrakis(4-sulfonatophenyl)porphyrin (TPPS) was purchased from Strem Chemicals, and used without further purification. Dimethylaminohexanol was obtained from TCI America. Grubbs first generation catalyst and norbornene carboxylic acid were purchased from Aldrich. Compound **1** was prepared according to our previously reported procedure. All solvents were purified and dried according to standard procedures.

#### **Synthesis**

*Synthesis of 6-(dimethylamino)hexyl bicyclo[2.2.1]hept-5-ene-2-carboxylate (**2**).* Acid chloride (**1**) (10.8 g, 0.069 M) was dissolved in freshly dried THF. Then, a mixture of 6-dimethylaminohexanol (14.22 mL, 0.086 M) and  $\text{NaHCO}_3$  (11.6 g, 0.14 M) were added to the solution at room temperature under  $\text{N}_2$  atmosphere and refluxed overnight. After the reaction was

complete, the mixture was filtered to remove the salt, and THF was removed under reduced pressure. This was followed by washing with water and extraction with CH<sub>2</sub>Cl<sub>2</sub>, then dried overnight. Na<sub>2</sub>SO<sub>4</sub>. Colorless oil was obtained after column chromatography with 3:1 CH<sub>2</sub>Cl<sub>2</sub>:MeOH, solvent removal, and vacuum drying (13.73g, 75%). <sup>1</sup>H NMR (500 MHz, CDCl<sub>3</sub>) δ: 8.98 (NH, 1H), 6.18-5.79 (m, 2H, HC=CH), 4.09 – 3.82 (m, 2H), 3.13 (s, 0.5H), 3.04-2.68 (m, 2H), 2.42-2.06 (m, 8H), 1.92 - 1.73 (s, 1H), 1.64 -1.06 (m, 11H). <sup>13</sup>C NMR (125 MHz, CDCl<sub>3</sub>) δ: 176.24, 174.69, (C=O exo and endo) 138.02, 137.55, 135.74, 132.36, 64.29, 63.38, 59.40, 46.74, 45.76, 43.07, 43.31, 30.40, 30.22, 29.27, 28.88, 28.34, 26.90, 25.79. HR-MS-ESI theoretical m/z [M+H]<sup>+</sup> = 266.21, found 266.21.

*Synthesis of polymer 3.* ROMP of monomer **2** with Grubbs' first generation catalyst was performed as shown in Scheme 4. The glassware was dried, evacuated under vacuum, and purged with N<sub>2</sub> in a Schlenk line several times prior to conducting the polymerization reaction. A solution (0.2 M) of monomer **2** (265 mg, 1 x 10<sup>-3</sup> M, 175 eq) was prepared in dry CH<sub>2</sub>Cl<sub>2</sub> under N<sub>2</sub>. The catalyst solution was prepared by dissolving the catalyst in anhydrous CH<sub>2</sub>Cl<sub>2</sub> under N<sub>2</sub> in a glovebox. The catalyst solution (8.5 mg, 1 x 10<sup>-6</sup> M in 0.5 mL CH<sub>2</sub>Cl<sub>2</sub>, 1 eq) was added to the reaction mixture and stirred for 1 h at 30 °C. The polymerization reaction mixture was terminated with excess ethyl vinyl ether (300 eq relative to catalyst) and stirred for another 1 h. The reaction mixture was then poured into cold methanol, stirred, collected by filtration, and dried under vacuum, yielding flaky white solid in 82% yield. <sup>1</sup>H NMR (500 MHz, CDCl<sub>3</sub>) δ: 5.54 -5.09 (b, -HC=CH-), 4.22- 3.84, 3.26- 2.61, 2.58-2.22, 2.15-1.85, 1.80-1.05(b). M<sub>w</sub> =3400 (by NMR), M<sub>w</sub> =3400 (by NMR), n ~ 13.

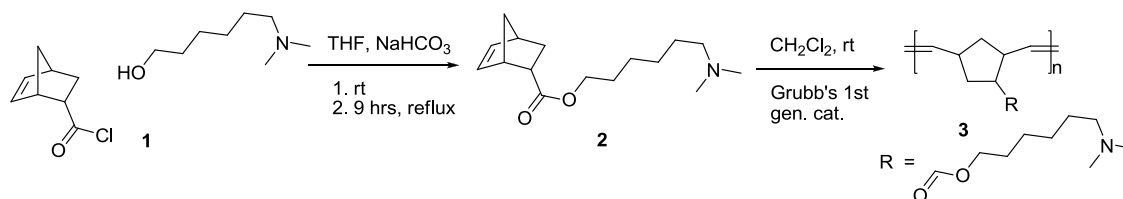
## Methods

$^1\text{H}$  NMR and  $^{13}\text{C}$  NMR spectra were acquired on a Varian Mercury Gemini spectrometer at 500 and 125 MHz, respectively, using  $\text{CDCl}_3$  as the solvent for all monomers and polymers. High resolution mass spectrometry (HR-MS) analysis was performed in the Department of Chemistry, University of Florida, Gainesville, FL. Samples for the spectroscopy measurements were prepared by dissolving the dyes in ultrapure water and acidified with 0.2 M HCl solution. Different buffer solutions (pH: 2.2-1.0) were prepared according to the CRC handbook<sup>14</sup> procedure.

Linear photophysical properties were investigated in spectroscopic-grade solvents (DMSO and ultrapure water) at room temperature. Absorption spectra were obtained with an Agilent 8453 UV-visible spectrophotometer using 10 mm path length quartz cuvettes with dye concentrations of  $1 \times 10^{-5}$  M. Fluorescence spectra were obtained with a Photon Technologies, Inc. (PTI) QuantaMaster spectrofluorimeter, using 10 mm spectrofluorometric quartz cuvettes and low concentration  $C \leq 10^{-6}$  M. All fluorescence spectra were corrected for the spectral sensitivity of the PTI emission monochromator and photomultiplier tube (PMT) detector. The values of the fluorescence lifetime of were measured with a time-correlated single photon counting system (PicoQuant PicoHarp 300) under linear polarized femtosecond excitation.

## 5-4. Results and discussion

**Scheme 4.** Synthesis of monomers and homopolymer.



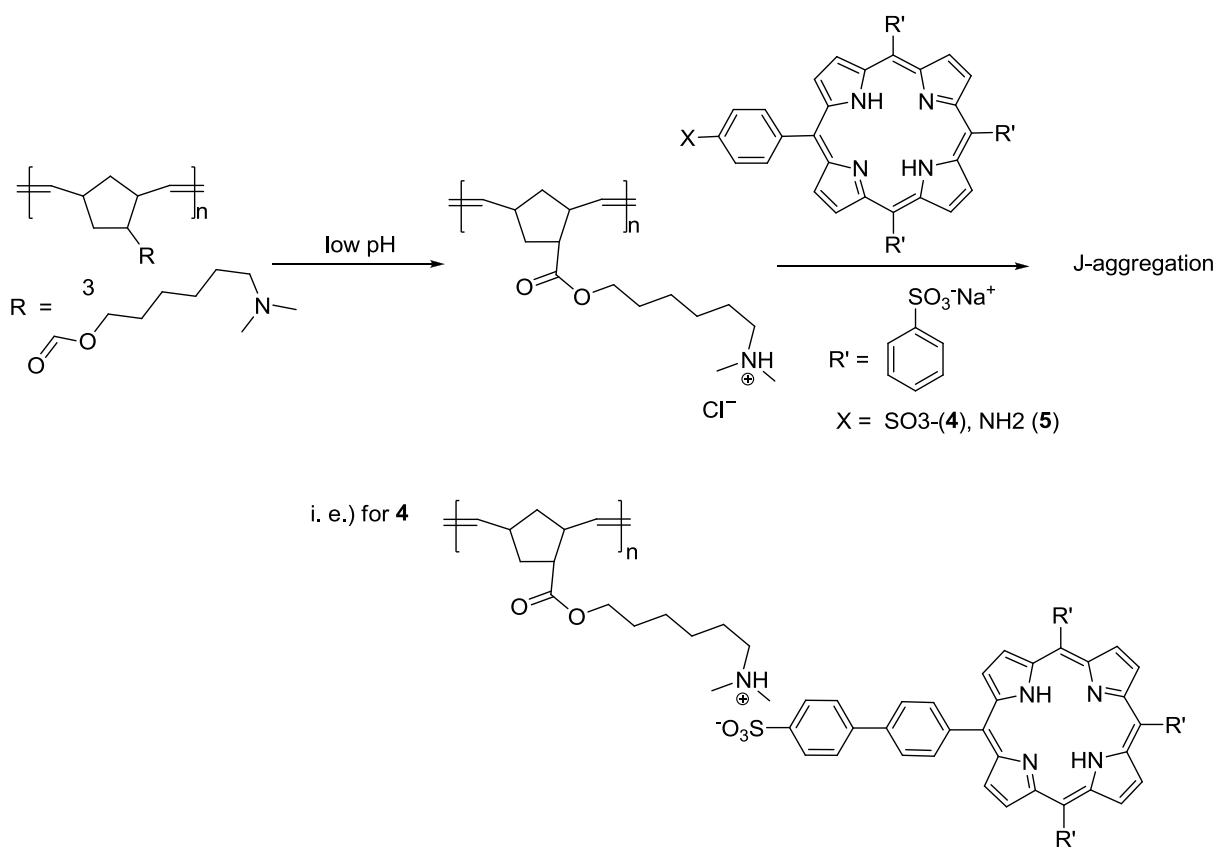
**Synthesis.** The synthesis of monomer **2** is shown in Scheme 4. Acid chloride **1** was reacted with 6-dimethylaminohexanol under basic conditions, affording ester **2**. The NMR spectra and GCMS results confirmed product formation. The homopolymer of **2** was prepared via ROMP, using Grubbs' first generation catalyst, and characterized by NMR, (see Experimental Section). The polymer was soluble in organic solvents such as  $\text{CHCl}_3$  and  $\text{CH}_2\text{Cl}_2$ . However, the solubility of the homopolymer in THF was poor, which restricted measurement of the molecular weight via GPC with polystyrene as standard in THF. Therefore, the molecular weight of the polymer was estimated by comparison of its diffusion coefficient with the diffusion coefficients of three polyethylene glycol standards via an NMR technique (see the Supporting Information),<sup>ref</sup> resulting an estimated molecular weight of ca. 3400. The polymer became water soluble after lowering the pH with HCl due to protonation at the amino groups. As the porphyrin derivatives generally undergo aggregation at low pH (<1) in aqueous medium, polymer **3** should serve as a suitable template.

An analog of commercially available TPPS dye, **4** was synthesized by a three-step process.<sup>15</sup> Briefly, tetraphenylporphyrin was selectively nitrated (mono) with fuming nitric acid, then the resulting nitro group was reduced with  $\text{SnCl}_2/\text{conc. HCl}$ , transformed it into an amino

group, followed by exhaustive sulfonation to produce water soluble porphyrin derivative **4**, an analog of **5**.

The solutions of two porphyrin dyes (**4** and **5**) were prepared in aqueous solution at low pH by acidification with different buffers (HCl/KCl – pH range 2.2, 2.0, 1.5, 1.0). The solutions of dyes were prepared in neutral conditions by dissolving them in ultra-pure water (pH ~ 7.0) and another in acidic condition by adding 0.2 M HCl (without adding any salt, pH 2.0). All the solutions were prepared at the same concentration of porphyrin dye ( $[C] = 4 \times 10^{-6}$  M, Figure 26). To investigate the use of a polymer template for porphyrin aggregation, homopolymer **3** was dissolved in the same pH buffers as mentioned above and a certain amount (0.4g/L) of the porphyrin dye was gradually added (Scheme 5). All solution preparation and photophysical studies were done in the dark. The aggregation properties were studied by time-dependent UV-vis absorption, fluorescence, and fluorescence lifetime decay for both the dye solutions themselves as well as polymer-templated dye solutions.

**Scheme 5.** Scheme for dye aggregation with the polymeric template.



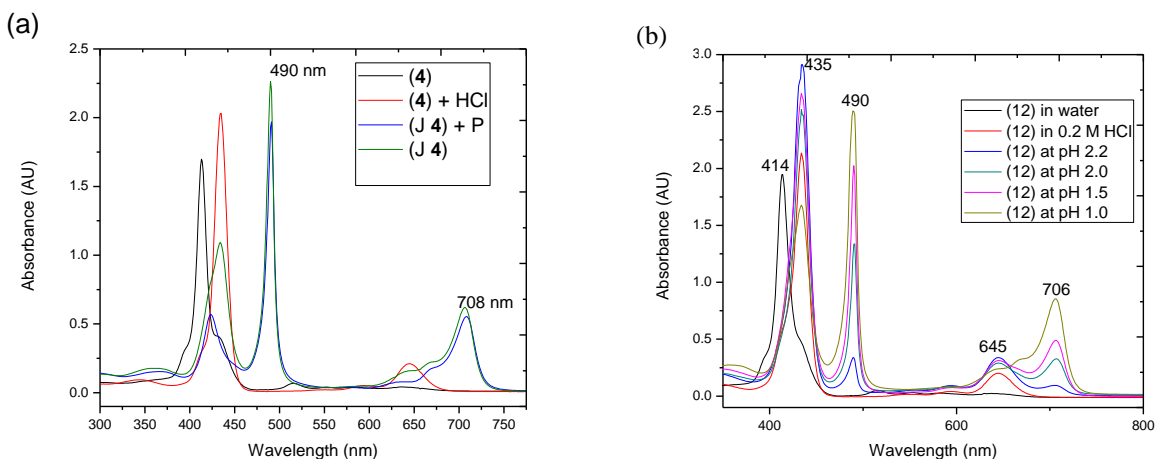


**Figure 26.** (a) UV-vis absorption spectra of (4) solution (black line is 4 in water, red is 4 in acidic condition (0.2 M HCl), green is 4 in pH 1 buffer, and blue is 4 templated with polymer in pH 1 buffer); (b) formation of J-aggregates of (4) at different pH (HCl/KCl aqueous buffer).

**UV-vis Absorption Spectroscopy:** The absorption spectra of TPPS (4) and its analog (5) in acidified water with or without a polymer template at  $10^{-5}$  M concentration of the dyes were measured. Commercially available TSPP (4) is known to form J-aggregates under strong acidic conditions. In neutral aqueous solution, TPPS remains as a monomeric free base form considering the electrostatic anionic repulsion from the sulfonate group. The absorption bands correspond to its non-protonated form (Figure 27 (a)), having an intense Soret band at 414 nm and weak Q bands at 516, 550, 581, and 635 nm.

In the presence of acid, protonation takes place at the 2 N of the porphyrin core. Thus, the absorption maxima of Soret band shifts to 435 nm and the two Q bands shift to 590 and 645 nm. The presence of J-type aggregation is usually signaled by an intense and narrow absorbance at

490 nm (J-band), which is bathochromically shifted relative to the monomer absorption band at about 435 nm (the Soret band), and a weaker broad band at 705 nm. The 490 nm J-band of the aggregates has been assigned to a Frenkel exciton transition.<sup>18,19</sup> Porphyrins tend to self-assemble through balancing  $\pi$ - $\pi$  oblique stacking interactions of their hydrophobic porphyrin rings, and charged substituent groups, present at the inner (cationic N) core and outer surface (anionic sulfonate groups) by electrostatic forces. The induction of J-aggregation of **4** was been studied using HCl/KCl buffers (pH range 2.2 -1.0) at room temperature in the dark. Porphyrin **4** formed stronger J-bands with decreasing pH (Figure 27 (b)). At pH 1.0, with increasing time, more molecules of **4** appear to participate in the J-aggregation, as shown in Figure 27 (b). This behavior is consistent with other reports.<sup>20</sup>

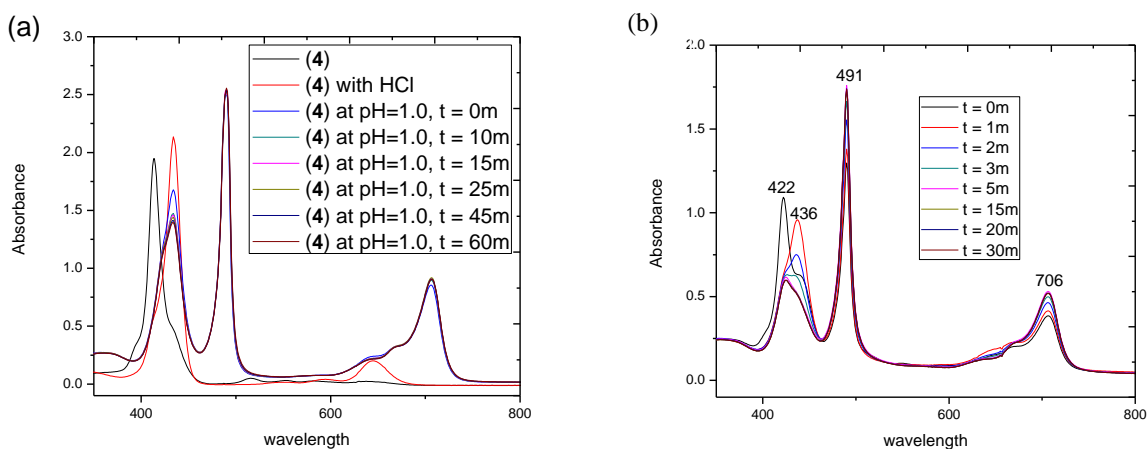


**Figure 27.** (a) Kinetic study of J-band of **4** at pH 1.0 at different time intervals (a 1.0 cm path length cuvette cell was used with (**4** = 40  $\mu$ M) at room temperature), (b) Formation of stable J-aggregates of **4** in the presence of polymer **3** in aqueous buffer (pH = 1.0) at different time intervals.

In the presence of polymer **3**, porphyrin **5** produced a well-defined strong and sharp J-band at 491 nm along with a broad band at 706 nm, while an H band at 422 nm appeared at slightly higher pH (>1.0). Formation of the H-aggregates is generally attributed to  $\pi$ -conjugation of the porphyrin rings with the combined effect of attractive  $\sigma$ - $\pi$  and repulsive  $\pi$ - $\pi$  interactions.<sup>21</sup> Also, with increasing time periods (0-30 min), it has been noticed that more molecules were transformed from H-aggregation to J-aggregation with a very sharp and narrow J-band at 490 nm, possibly due to a stabilization effect of cationic polymer **3** as shown in Figure 28 (b). Also, the spectral width (full-width at half-maximum, FWHM) of the absorption peak of the J-aggregate varies with the coherence length as  $N^{-1/2}$ , where N is the spectroscopic aggregation number,<sup>22,23</sup> and the effect of external ammonium ions were reported.<sup>10</sup>

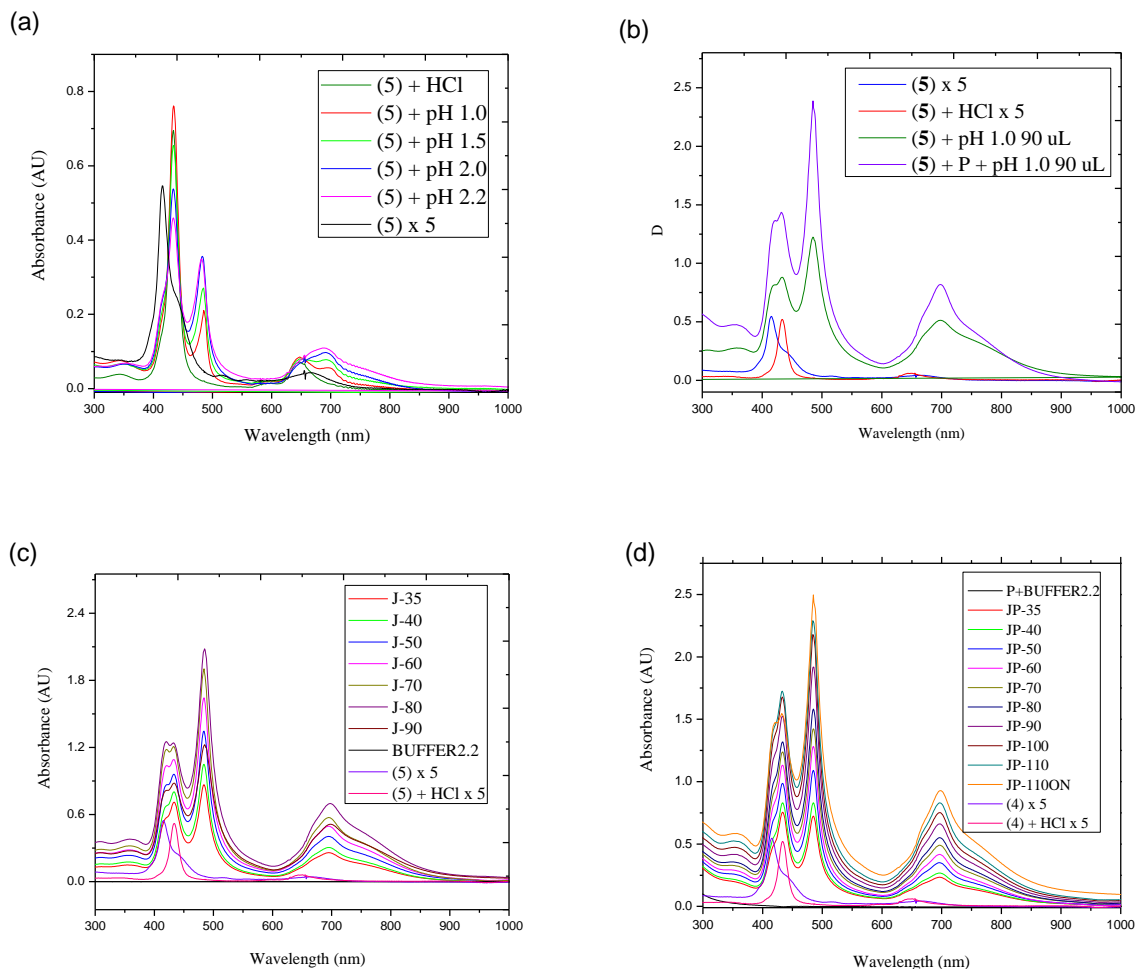


**Figure 28.** UV-vis absorption spectra of **5** (a) at different pH in HCl/KCl aqueous buffer and formation of J- aggregates of **5**, (b) in presence of polymer **3** at pH 1.0 (HCl/KCl buffer), (c) dependence of J-aggregation on concentration of **5** without polymer; (d) J-aggregation as a function of varying concentration of **5** in presence of polymer **3**. All experiments are done with

$[4] = 10^{-5}$  M in 1 cm cuvette at room temperature.

To the best of our knowledge the J-aggregation of porphyrin **5** has not been reported. Porphyrin **5**, in its non-protonated form, exhibited a Soret band at 416 nm along with a shoulder at 444 nm and a weak band at 654 nm. In presence of 0.2 M HCl, the Soret band of **5** bathochromically shifted to 433 nm and the Q band blue shifted to 647 nm. Porphyrin **5** behaved differently with respect to **4** in the pH range 1.0-2.2 due to the presence of the amine group instead of the fourth sulfonate group at the para position of one of the phenyl substituents. Porphyrin **5** showed an increasing J-band with increasing pH (Figure 28 (a)) at sharp J-band at 484 nm and another red shifted band at 696 nm. With the addition of polymer **3**, stronger J-aggregation of **5** occurred at the same concentration of the dye at pH 1.0 relative to without the polymer, which is clear from the higher ratio and sharper nature of the peak corresponding to the J band at 484 nm to the peak at 432 nm. In addition to  $\pi$ - $\pi$  hydrophobic interactions and the electrostatic attraction force between imidazolium ring and sulfonated phenyl group, the interaction of the cationic dimethylammonium groups in the J-aggregated species reduced the repulsive forces among porphyrin rings, thus, making the J-aggregation solution more stable in aqueous solution.

**Fluorescence Spectroscopy:** Steady state fluorescence emission spectra were recorded for TPPS under neutral conditions, acidic conditions ( $10^{-6}$  M), and after formation of J-aggregates with or without the polymer ( $10^{-5}$  M) at room temperature in 1 cm cuvettes using a PTI Quantamaster spectrofluorimeter. The emission spectra did not change whether excited at the B or Q bands, as reported in literature.<sup>20</sup> Emission of the aggregated species (with or without polymer) was considerably weaker, with almost negligible Stokes shifts, compared to the

monomer and dianion species, likely due to the predominance of radiative quenching pathways.<sup>20b</sup>

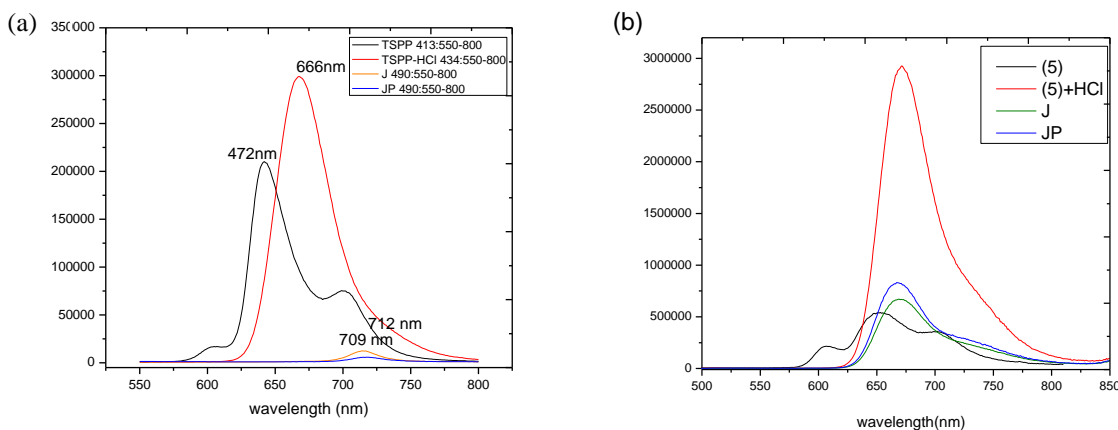


**Figure 29.** Steady state fluorescence spectra of (a) **4** (black line is **4** in water, red is **4** in acidic condition (0.2 M HCl), orange is **4** in pH 1 buffer, and blue is **4** templated with polymer in pH 1 buffer) and (b) **5** (black line is **5** in water, red is **5** in acidic condition (0.2 M HCl), green is **5** in pH 1 buffer, and blue is **5** templated with polymer in pH 1 buffer).

Figure 29 shows the fluorescence spectra of **4** and **5** resulting from the excitation of the Soret band (B-band) of the species at 413, 434, and 490 nm for the free base, dianion monomer, and J-aggregated species, respectively. The emission spectra did not change whether excited at the B or Q bands, as previously reported.<sup>20b</sup> Emission of the aggregated species (with or without polymer) was considerably weaker, with almost negligible Stokes shifts, compared to the monomer and dianion species, again likely due to the predominant effect of radiative quenching pathways.

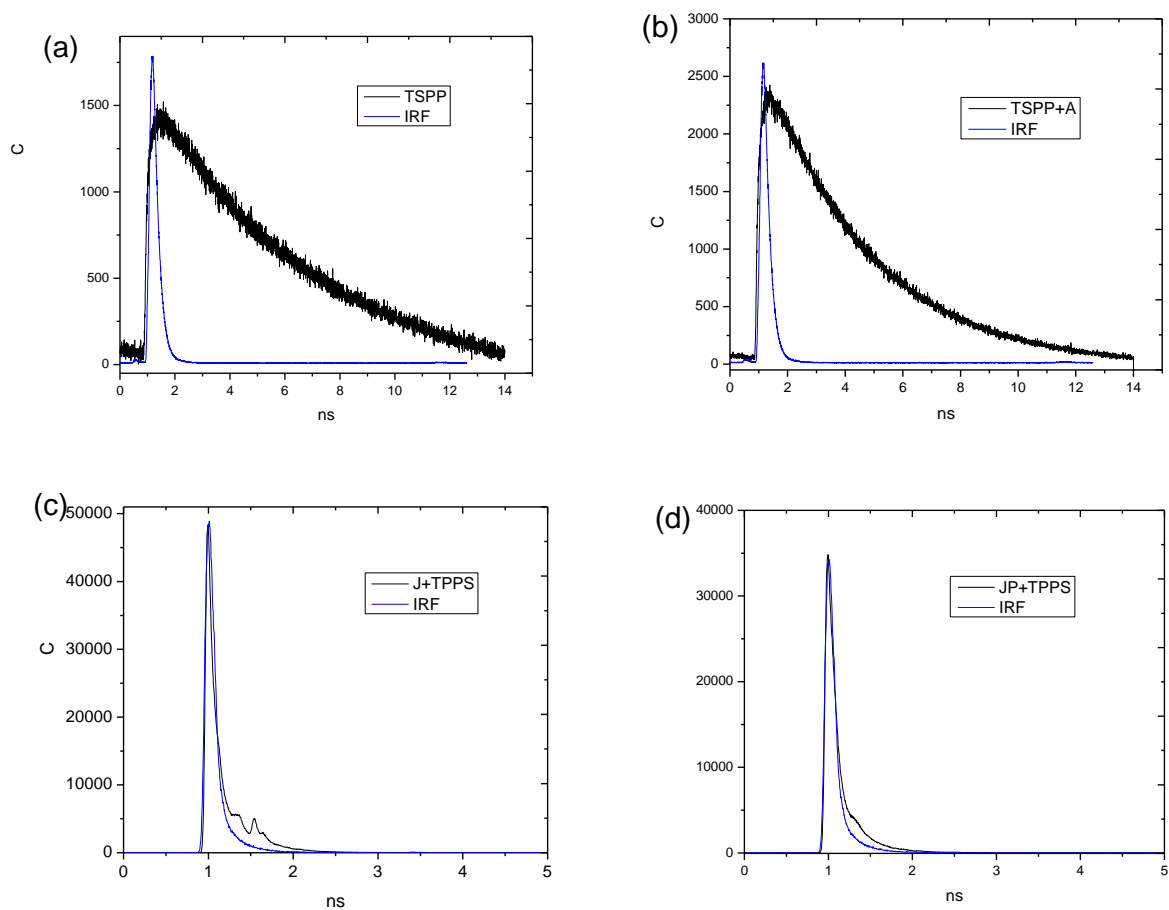


**Figure 30.** Fluorescence decays of TPPS monomer **4** (free base in water (a) and dianion in 0.2 M HCl (b)) and a J-aggregated species without (c) or with polymer (d) templates (both in pH 1), measured with time correlated singlephoton counting methods (compared with Instrument response function (IRF) in each case).

**Lifetime studies:** To shed light on the photodynamics of porphyrin J-aggregation, fluorescence lifetime decay was studied using a time-correlated single photon counting system (PicoHarp 300) under linear polarized femtosecond excitation.

Fluorescence lifetime decays of TPPS, **4**, are shown in Figure 30. The free base and dianion monomer had a single exponential decay with excited state lifetimes of 6.87 and 3.74 ns for nonlinear excitation at 826 and 868 nm, respectively. As anticipated, the lifetime of the J-aggregated species was very short when excited at the Q band (710 nm). Specifically, with the polymer template a shorter (250 ps) lifetime was observed, as shown in Table 5. Fluorescence quenching and shortening of the excited state lifetime can be explained by different mechanisms, e.g., efficient internal conversion between different energy states and fast quenching of fluorescence intermolecular phonon modes that controls motion in the aggregate formation direction.<sup>25,26</sup>

**Table 5.** Photophysical properties of the TPPS (**4**, free base and dianion) and related J-aggregations with or without polymer templates.

	$\lambda_{\text{abs}}$ (nm)	$\lambda_{\text{em}}$ (nm)	$\lambda_{\text{exc}}$ (nm)	Lifetime (ns)		
				$t_1$	$t_2$	$R^2$
TSPP ( <b>4</b> )	413, 515, 635	472	413(826)	6.87		0.99246
TSPP (0.2 M HCl)	434, 644	466	434 (868)	3.74		0.99788
TSPP (pH 1.0)	434, 490, 708	709	710	0.32	0.080	0.99711
TSPP + polymer (pH1)	421, 491, 711	712	710	0.25		0.99728

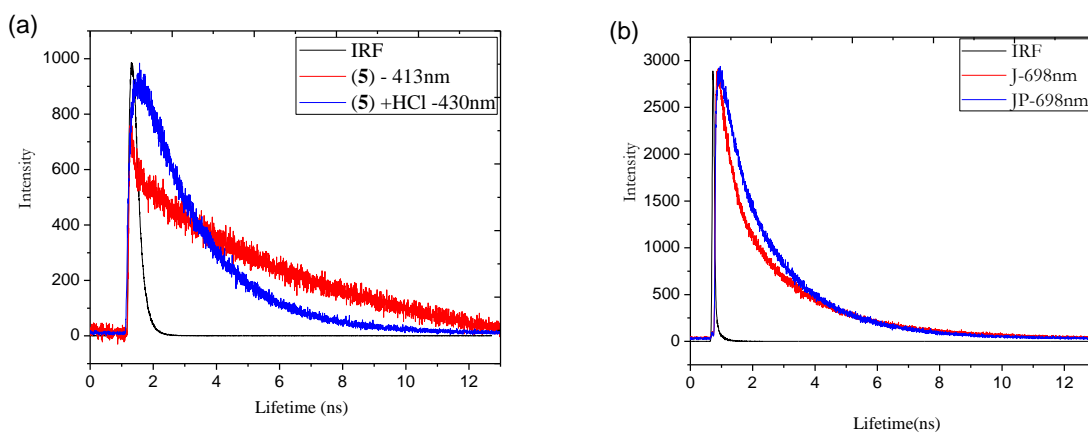


**Figure 31.** Fluorescence decays of monomer **5** (free base in water and dianion in 0.2 M HCl (a)) an J-aggregated species without or with polymer (b) templates, measured with time correlated singlephoton counting methods (compared with Instrument response function (IRF) in each case).

**Table 6.** Photophysical properties of the **5** (free base and anion) and related J-aggregations with or without polymer templates.

	$\lambda_{\text{abs}}$ (nm)	$\lambda_{\text{em}}$ (nm)	$\lambda_{\text{exc}}$ (nm)	Lifetime (ns)		$R^2$
				$t_1$	$t_2$	
NH2-TPPS ( <b>5</b> )	415, 659	606, 653, 706	413 (826)	6.47		0.980
NH2-TPPS+HCl	433,647	671	430 (860)	2.01		0.9964
J	433, 485, 698	671	698	2.22 (64%)	0.35(36%)	0.9982
JP	433, 485, 698	671	698	1.87(80%)	0.24 (20%)	0.9984

Fluorescence lifetime decays of porphyrin **5**, are shown in Figure 31. For **5** the lifetime for free monomer and its anionic form are 6.47 and 2.01 ns, respectively, as shown in Table 6. While at a higher concentration of the dye, with or without polymer, it forms partially J-aggregated species with a very short lifetime along with the contribution from its anionic form.

**Nonlinear absorption studies:** In order to broaden the potential applications of porphyrin aggregates and probe the effect of aggregation on nonlinear absorption, two-photon absorption (2PA) cross sections ( $\delta_{2PA}$ ) were measured by an open aperture Z-scan method using an amplified Ti:sapphire laser system (Coherent, Legend Elite seeded with a Verdi-pumped Mira 900) with an optical parametric amplifier (Coherent OPerA Solo) providing laser pulses of ~100 fs (FWHM) duration with 1 kHz repetition rate (Figure 32) in a 1 mm quartz cuvette at room temperature. The concentration of TSPP (**4**) solution for Z scan measurement was  $10^{-2}$  M. J-aggregated TPPS solution at pH 1 and polymer-templated J-aggregated TPPS were used at  $10^{-3}$  M due to precipitation at higher concentrations.

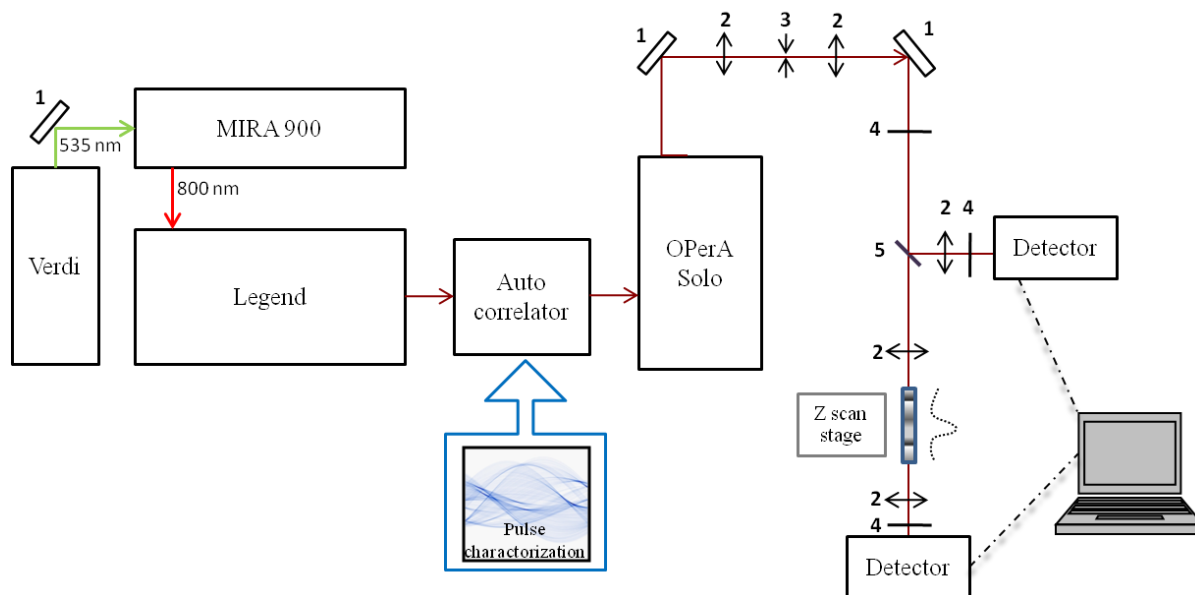


**Figure 32.** Z scan experiment setup, (1) 100% reflection mirrors, (2) focusing lens, (3) pinhole, (4) neutral density filter, and (5) beam splitter.

As shown in Figure 33, 2PA cross section of TPPS is 30 to 95 G. M. (Goppert-Mayer,  $1 \times 10^{-50} \text{ cm}^4 \text{ s photon}^{-1} \text{ molecule}^{-1}$ ). After undergoing aggregation in pH 1, the 2PA cross section values increased by a factor of four. In addition, after polymer-templated aggregation the 2PA cross section values increased 2.5 times. Therefore, the polymer template not only increased J-aggregates but the increased J-aggregation increased two-photon absorption.

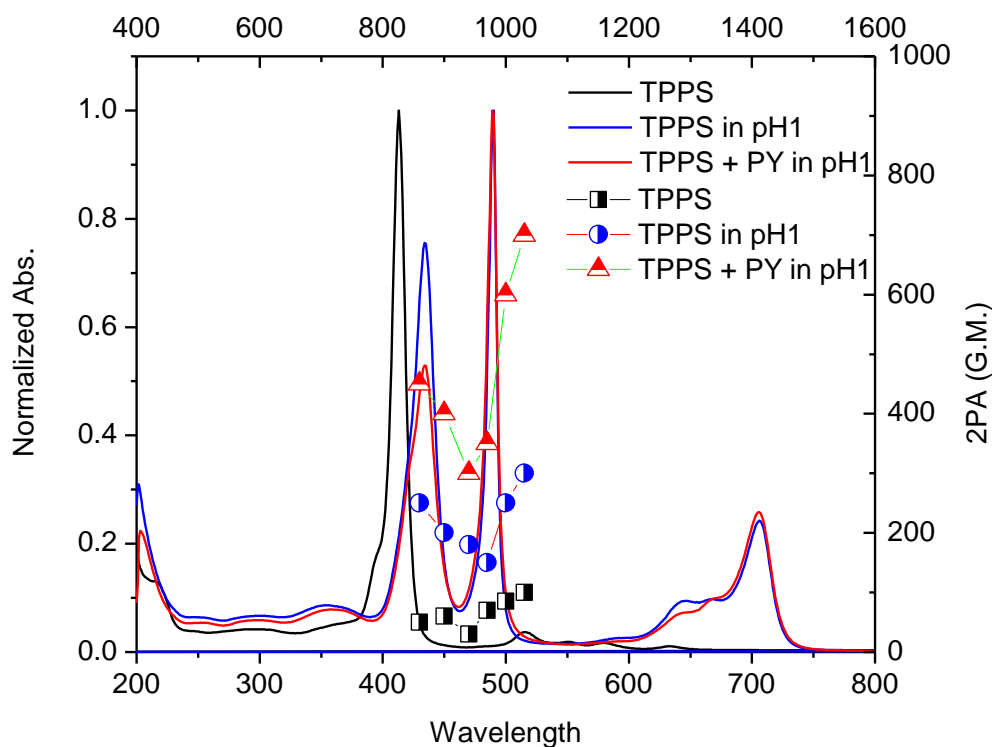


**Figure 33.** Normalized absorption spectra and 2PA cross sections of **4** in water, TPPS in pH 1 solution, and **4** with polymer in pH 1 solution. **4** (black line is the absorption spectrum of **4** in water, blue line is the absorption spectrum of **4** in pH 1 buffer solution, red line is the absorption spectrum of **4** templated with polymer in pH 1 buffer, black half-filled square dots are nonlinear optical spectrum of **4** in water, blue half-filled circle dots are nonlinear optical spectrum of **4** in pH 1 buffer solution, and red half-filled triangle dots are nonlinear optical spectrum of **4** templated with polymer in pH 1 buffer).

### **5-5. Conclusion**

The effects exerted by a ROMP-based water soluble polymeric template, containing pendant amino groups, on the J-aggregation properties of two porphyrin-based dyes (TSPP, **4**, and its amine-containing analog **5**) were investigated. The photophysical properties of the J-aggregated species showed facilitation of J-aggregation by the amphiphilic polymer, with the polymer inducing J-aggregation faster than the dye alone under similar conditions. TSPP dye **4** produce J-aggregated species with or without the polymer template more efficiently compared to **5**. Not surprisingly, substitution of one sulfonic acid group by an amine group may have affected the ionic interaction of the dyes, thereby influencing aggregation properties. These results support the use of cationic polymer templates to enhance the J-aggregation in solution through possible attractive interaction between anionic porphyrin periphery, facilitating the design of polymer-templated supramolecular aggregates. Significantly, two-photon absorption of J-aggregates was higher than the corresponding unaggregated porphyrins. This provides a means to modulate the nonlinear absorptivity of a porphyrin.

### **References**

- (1) Collini, E.; Ferrante, C.; Bozio, R. *The Journal of Physical Chemistry. B* **2005**, *109*, 2-5.
- (2) Scheibe, G. *Angew Chem* **1936**, *49*, 563.
- (3) Jelly, E.E. *Nature* **1936**, *138*, 1009.
- (4) Kasha, M.; Rawls, H. R.; El-Bayoumi, M. A. *Pure Appl. Chem* **1965**, *11*, 371-392.
- (5) Ohno, O.; Kaizu, Y.; Kobayashi, H. *The Journal of Chemical Physics* **1993**, *99*, 4128.

- (6) Lin, J.; Ding, W.; Hong, K.; Mays, J. W.; Xu, Z.; Yuan, Y. *Soft Matter* **2008**, *4*, 1605-1608.
- (7) Zhao, L.; Ma, R.; Li, J.; Li, Y.; An, Y.; Shi, L. *Biomacromolecules* **2008**, *9*, 2601-2608.
- (8) Wu, J. J.; Li, N.; Li, K. A.; Liu, F. *The Journal of Physical Chemistry B* **2008**, *112*, 8134-8138.
- (9) Purrello, R.; Bellacchio, E.; Gurrieri, S.; Lauceri, R.; Raudino, A.; Scolaro, L. M.; Santoro, A. M. *J. Phys. Chem. B* **1998**, *102*, 8852-8857.
- (10) Koti, A. S. R.; Taneja, J.; Periasamy, N. *Chemical Physics Letters* **2003**, *375*, 171-176.
- (11) Jones, R. M.; Lu, L.; Helgeson, R.; Bergstedt, T. S.; McBranch, D. W.; Whitten, D. G. *Proceedings of the National Academy of Sciences* **2001**, *98*, 14769.
- (12) Lu, L.; Jones, R. M.; McBranch, D.; Whitten, D. *Langmuir* **2002**, *18*, 7706-7713.
- (13) Kano, K.; Watanabe, K.; Ishida, Y. *The Journal of Physical Chemistry B* **2008**, *112*, 14402-14408.
- (14) Steinbeck, C. A.; Ernst, M.; Meier, B. H.; Chmelka, B. F. *J. Phys. Chem. C* **2008**, *112*, 2565-2573.
- (15) Smith, A. R. G.; Ruggles, J. L.; Yu, A.; Gentle, I. R. *langmuir* **2009**, *25*, 9873-9878.
- (16) Lide, D. R. *Handbook of chemistry and physics*; CRC Pr I Llc, 2003.
- (17) Kruper Jr, W. J.; Chamberlin, T. A.; Kochanny, M. *The Journal of Organic Chemistry* **1989**, *54*, 2753-2756.
- (18) Akins, D. L.; Ozcelik, S.; Zhu, H. R.; Guo, C. *J. Phys. Chem* **1996**, *100*, 14390-14396.
- (19) Kano, H.; Saito, T.; Kobayashi, T. *J. Phys. Chem. B* **2001**, *105*, 413-419.
- (20) Smith, A. R. G.; Ruggles, J. L.; Yu, A.; Gentle, I. R. *Langmuir* **2009**, *25*, 9873-9878.

- (21) Hunter, C. A.; Sanders, J. K. M. *Journal of the American Chemical Society* **1990**, *112*, 5525-5534.
- (22) Knapp, E. W. *Chemical Physics* **1984**, *85*, 73-82.
- (23) Knapp, E. W. *Chem. Phys. Lett.*, *11* **1984**, *1*, 481.
- (24) Akins, D. L.; Ozcelik, S.; Zhu, H.-R.; Guo, C. *The Journal of Physical Chemistry* **1996**, *100*, 14390-14396.
- (25) Kobayashi, T. *J-aggregates*; World Scientific, Singapore, 1996.
- (26) Misawa, K.; Kobayashi, T. *The Journal of Chemical Physics* **1999**, *110*, 5844.

## CHAPTER 6: PHOTSENSITIZATION OF CARBON NANOTUES USING DYE AGGREGATES

Reproduced with permission from: Ryuichi Tsuchikawa, Hyo-Yang Ahn, Sheng Yao, Kevin D Belfield and Masa Ishigami *Journal of Physics: Condensed Matter* **2011**, 23, 202204+05.  
Copyright 2011 IOP Publishing Ltd.

### **6-1. Abstract**

Ordered assemblies of dye molecules, dye aggregates, possess significantly larger molar optical absorptivity than dye monomers. Yet, aggregates have not been utilized for photosensitizing nanoscale electronic devices. We find that single-walled carbon nanotubes, which are cleaned down to atomic scale, template the growth of squaraine dye aggregates and these aggregates effectively photosensitize nanotubes. Templating of aggregates by nanotubes and functionalization of nanotubes with ordered molecular films are reported for the first time. The sensitivity achieved by aggregate-functionalized nanotube network devices is approximately an order of magnitude better than those of similar nanotube devices functionalized with dye monomers and photoactive polymers.

### **6-2. Introduction**

Carbon nanotubes (CNTs) can be used for developing novel nanoscale photodetectors [1]. Yet, the utility of such nanotube-based optoelectronics is limited because relatively high light intensities are required for inducing a detectable photoresponse [2]. Nanotubes can be

photosensitized by functionalizing their surface with dye molecules [3-11]. The nanotube surface morphology determines optoelectronic property of dye molecule films, the coupling of dye molecules to nanotubes and, therefore, the performance of photosensitized devices. Yet in previous studies, the structure of dye films were not controlled and the surface of nanotubes were likely covered with photoresist residues, which cannot be removed using traditional solvent-based techniques [12], as inferred from a recent scanning tunneling microscopy study [13].

Our approach for photosensitization, reported in this paper, is unprecedented: we begin with single-walled carbon nanotubes (SWNTs) which have been cleaned down to atomic scale [13] and functionalize these clean nanotubes by squaraine (SQ) dye molecules, which have a strong tendency for structural-ordering [14, 15]. We have investigated the interaction between SQ molecules and carbon nanotubes using optical absorption spectroscopy, atomic force microscopy (AFM), and photoconductivity measurements. SWNTs selectively promote the formation of SQ dye aggregates with a head-to-head stacking arrangement, and these SQ dye aggregates effectively photosensitize SWNTs. Nanotube network devices functionalized with dye aggregates are sensitive down to  $20 \mu\text{W}/\text{cm}^2$ , demonstrating that our novel approach can yield highly photosensitized devices.

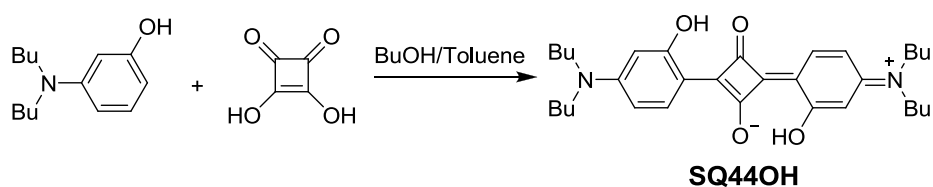
### **6-3. Experimental Materials and Methods**

#### **Synthesis**

(Z)-2-(4-(dibutylamino)-2-hydroxyphenyl)-4-(4-(dibutylaminio)-2-hydroxycyclohexa-2,5-dienylidene)-3-oxocyclobut-1-enolate (SQ44OH), a SQ dye was nicely provided by Dr. Sheng Yao (Belfield research group) and reported previous study [37]

### **6-4. Results and discussion**

**Scheme 6.** Molecular structure of SQ44OH



Scheme 6 shows (Z)-2-(4-(dibutylamino)-2-hydroxyphenyl)-4-(4-(dibutylaminio)-2-hydroxycyclohexa-2,5-dienylidene)-3-oxocyclobut-1-enolate (SQ44OH), a SQ dye, chosen for its large hydrophobic “tails” that can increase the interaction with the hydrophobic  $\pi$ -bonded nanotube walls. SQ dyes have been studied extensively due to their unique optical properties and their potential utility in a number of optoelectronic applications, including imaging, photovoltaics, and nonlinear optics [16]. In solvents [14, 15] and on various substrates [17-19], SQ dyes readily assemble into supramolecular structures with strong intermolecular coupling known as *J* (*Jelley*)-aggregates, in which molecules are stacked side-by-side, and *H* (*Hypsochromic*)-aggregates, in which molecules are stacked face-to-face. Optical properties of aggregates are determined by the  $\pi$ - $\pi$  interaction between dye molecules and are characterized by

narrow absorption bands, high absorptivity, large polarizability and nonlinearity [20]. With respect to those of dye monomers, *J*-aggregates have red-shifted absorption bands, called *J*-bands, while the absorption bands of *H*-aggregates possess blue-shifted bands, called *H*-bands. Optical properties for aggregates in thin films remain relatively unknown while aggregation of SQ and other dye molecules has been extensively studied in solution [17, 19, 21-23].

SQ44OH was dissolved in 1,2-dichloroethane (DCE) with a concentration of 1 wt%. Dye molecules in DCE display a strong peak in the optical adsorption spectrum at 650 nm with a full width at half maximum of 29 nm, accompanied by a minor shoulder at approximately 600 nm, as shown in Figure 34a. The absorption spectrum indicates that SQ44OH molecules exist as isolated monomers in solution. CNTs were grown from cobalt [24] or iron-based catalyst [25] using chemical vapor deposition, producing nanotube networks, which contain a mix of 1~3 nm diameter semiconducting and metallic SWNTs [25, 26], with densities of approximately 0.4 to 8 nanotubes per  $\mu\text{m}^2$ . Cobalt-seeded nanotubes were used for optical and AFM measurements on quartz substrates and iron-seeded nanotubes were used for photoconductivity measurements on  $\text{SiO}_2$ . SQ44OH was coated on substrates using a spin-coater at 3000 rpm. The spin-coated films were vacuum-annealed at 80 °C for 30 minutes to remove the residual solvent prior to measurements. The dye film thickness was observed to be approximately 100 nm on both quartz and nanotubes as measured by AFM. Optical absorption measurements were performed using a standard UV-visible spectrophotometer. Digital Instruments Multimode Microscope operated in air was used for the AFM measurements. Nanotube network devices [27] used for photoconductivity measurements were fabricated using photolithography and cleaned down to atomic scale using the hydrogen annealing process [13] prior to functionalization. The

cleanliness of nanotubes was confirmed by scanning probe microscopy measurements in a previous study [13]. Photoconductivity measurements were performed using a homemade setup that has a xenon lamp coupled with a standard monochromator. The light intensity was maintained at  $10 \text{ mW/cm}^2$  with the bandwidth of 5 nm for the measurements.

Figure 34b shows the comparison of optical absorbance spectra of nanotubes, dye molecules on quartz and dye molecules on nanotube network. Optical absorbance of nanotubes is negligible as nanotube films used for our functionalization studies were only one nanotube in thickness at most locations. Prominent absorption bands for dye molecules on quartz are located at 618 and 785 nm, each with broad shoulders tending towards 700 nm. The peak at 618 nm corresponds to the blue-shifted absorption band of *H*-aggregates, while the peak at 785 nm is due to the red-shifted band of *J*-aggregates. The plateaus are due to the broadening of absorption bands caused by the inhomogeneous environment of the sample and substrate as observed previously in films of other SQ dyes [18]. SQ44OH molecules exist as *H*- or *J*-aggregates on quartz substrates, with a comparable amount of each aggregates.

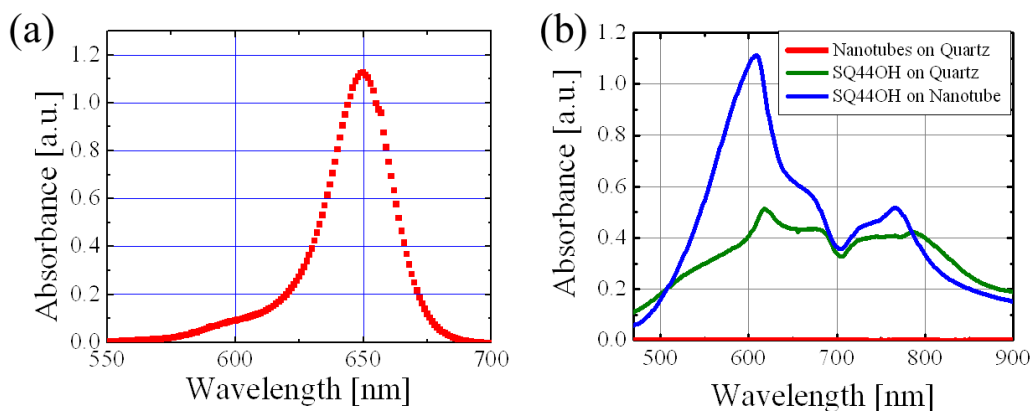


**Figure 34.** (a) Optical absorption spectrum of SQ44OH in DCE (1 % by weight). (b) Optical absorption spectra of a nanotube network on quartz (red), SQ44OH on quartz (green) and SQ44OH on a nanotube network (blue).

Two peaks at 608 and 766 nm characterize the absorption spectrum of dye molecules on nanotubes, with a broad shoulder extending from both the blue- and red-shifted bands as shown in Figure 34b. Blue-shifting of both H- and J-bands is likely due to the interaction of dye aggregates with nanotubes. The absorbance at the H-band increased by 115%, while the absorbance at the J-band increased by 20% compared to the molecules on quartz without changing the thickness of the dye film. Therefore, the H-band is significantly enhanced in the presence of nanotubes.

AFM images of clean nanotubes, dye molecules on quartz, and dye molecules on nanotubes are shown in Figure 35. Dye clusters on quartz are radially symmetric (Figure 35a), while the clusters are not symmetric and manifest rod-like appearances on nanotubes (Figure

35b). These rod features are not due to simple coating of dye molecules on nanotubes since clean as-grown nanotubes have a radically different morphology (Figure 35c)..

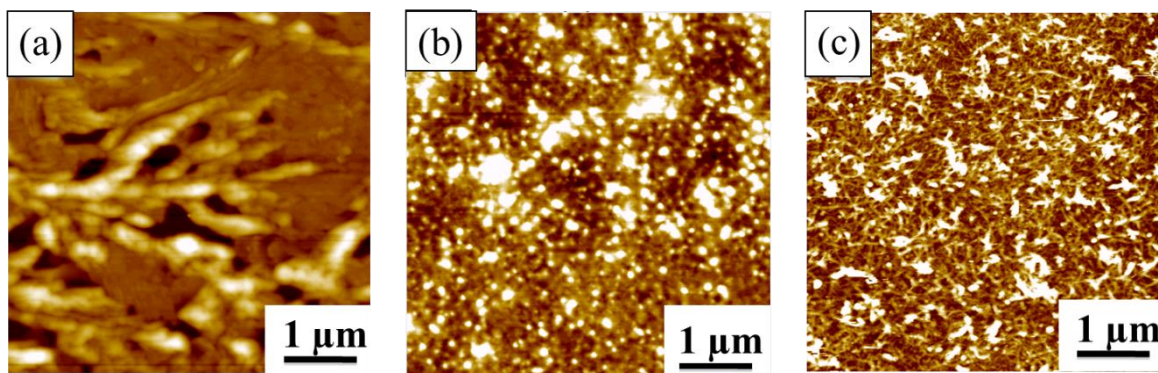


**Figure 35.**  $5 \times 5 \mu\text{m}^2$  AFM images of (a) SQ44OH on quartz, (b) SQ44OH on nanotubes, and (c) as-grown nanotubes.

Dr. Ishigami's research group calculated height-height correlation functions (see the appendix), indicating that dye molecules deposited on nanotubes have a different morphology compared to the underlying nanotube network. Therefore, we conclude that the presence of nanotubes enhances the size of aggregates by ca. 100%, and this enlargement of aggregates leads to the observed enhancement of optical absorptivity of the H-band. Also, Dr. Ishigami's research group compared the optical response of bare and aggregate-functionalized nanotube network devices. The wavelength-dependent response of the device to light resembles the optical absorption spectrum. Assuming the optical response to be linear with the intensity of the incoming light, it was estimated that the device was sensitive down to  $20 \mu\text{W}/\text{cm}^2$  from 620 to 760 nm with 25 volt applied to the gate electrode [34]. The observed photosensitivity was better

than previous dye monomer- [9, 11] or photoactive polymer-sensitized [35] devices by nearly an order of magnitude (see the appendix).

### **6-5. Conclusion**

We have functionalized atomically-clean SWNTs with SQ44OH which has a strong propensity to form dye aggregates. SWNTs are found to template aggregation of SQ44OH, strongly favoring aggregates in the face-to-face arrangement. Our AFM studies show that the observed enhancement in optical absorptivity is caused by doubling of the size of aggregates. Photoconductivity measurements on nanotube network devices reveal that dye aggregates, templated by nanotubes, effectively photosensitize nanotubes. Understanding and controlling the mechanism of the templating behavior of dye aggregates on nanotubes are clearly the next steps necessary to realize further improvements in photosensitization.

### **References**

1. P. Avouris and J. Chen, *Nanotube electronics and optoelectronics*. Materials Today, **9**(10): p. 46-54,(2006).
2. M. Freitag, Y. Martin, J.A. Misewich, R. Martel, and P.H. Avouris, *Photoconductivity of single carbon nanotubes*. Nano letters, **3**(8): p. 1067-1071,(2003).
3. Y.M. Shi, H. Tantang, C.W. Lee, C.H. Weng, X.C. Dong, L.J. Li, and P. Chen, *Effects of substrates on photocurrents from photosensitive polymer coated carbon nanotube networks*. Applied Physics Letters, **92**(10),(2008).

4. B. Pradhan, K. Setyowati, H.Y. Liu, D.H. Waldeck, and J. Chen, *Carbon nanotube - Polymer nanocomposite infrared sensor*. Nano Letters, **8**(4): p. 1142-1146,(2008).
5. N. Lebedev, S.A. Trammell, S. Tsoi, A. Spano, J.H. Kim, J. Xu, M.E. Twigg, and J.M. Schnur, *Increasing efficiency of photoelectronic conversion by encapsulation of photosynthetic reaction center proteins in arrayed carbon nanotube electrode*. Langmuir, **24**(16): p. 8871-8876,(2008).
6. J.P. Casey, S.M. Bachilo, and R.B. Weisman, *Efficient photosensitized energy transfer and near-IR fluorescence from porphyrin-SWNT complexes*. Journal of Materials Chemistry, **18**(13): p. 1510-1516,(2008).
7. K. Yanagi, K. Iakoubovskii, H. Matsui, H. Matsuzaki, H. Okamoto, Y. Miyata, Y. Maniwa, S. Kazaoui, N. Minami, and H. Kataura, *Photosensitive function of encapsulated dye in carbon nanotubes*. Journal of the American Chemical Society, **129**(16): p. 4992-4997,(2007).
8. J.M. Simmons, I. In, V.E. Campbell, T.J. Mark, F. Leonard, P. Gopalan, and M.A. Eriksson, *Optically modulated conduction in chromophore-functionalized single-wall carbon nanotubes*. Physical Review Letters, **98**(8),(2007).
9. D.S. Hecht, R.J.A. Ramirez, M. Briman, E. Artukovic, K.S. Chichak, J.F. Stoddart, and G. Gruner, *Bioinspired detection of light using a porphyrin-sensitized single-wall nanotube field effect transistor*. Nano letters, **6**(9): p. 2031-2036,(2006).
10. J. Borghetti, V. Derycke, S. Lenfant, P. Chenevier, A. Filoramo, M. Goffman, D. Vuillaume, and J.P. Bourgoin, *Optoelectronic switch and memory devices based on*

- polymer-functionalized carbon nanotube transistors*. Advanced Materials, **18**(19): p. 2535-+,(2006).
11. A. Star, Y. Lu, K. Bradley, and G. Gruner, *Nanotube optoelectronic memory devices*. Nano letters, **4**(9): p. 1587-1591,(2004).
  12. *Such as recommended by the Microchem Corporation (www.microchem.com)*.
  13. M. Ishigami, J.H. Chen, W.G. Cullen, M.S. Fuhrer, and E.D. Williams, *Atomic structure of graphene on SiO<sub>2</sub>*. Nano letters, **7**(6): p. 1643-1648,(2007).
  14. E.E. Jelly, *Spectral absorption and fluorescence of dyes in the molecular state*. Nature, **138**: p. 1009,(1936).
  15. G. Scheibe, *Variability of the absorption spectra of some sensitizing dyes and its cause*. Angew. Chem., **49**: p. 563,(1936).
  16. S. Sreejith, P. Carol, P. Chithra, and A. Ajayghosh, *Squaraine dyes: a mine of molecular materials*. Journal of Materials Chemistry, **18**: p. 264-274,(2008).
  17. H.J. Chen, M.S. Farahat, K.Y. Law, and D.G. Whitten, *Aggregation of surfactant squaraine dyes in aqueous solution and microheterogeneous media: Correlation of aggregation behavior with molecular structure*. Journal of the American Chemical Society, **118**(11): p. 2584-2594,(1996).
  18. M. Furuki, M. Tian, Y. Sato, L.S. Pu, S. Tatsuura, and S. Abe, *Absorption bleaching of squarylium dye J aggregates via a two-photon excitation process*. Applied Physics Letters, **79**: p. 708-710,(2001).

19. R.S. Stoll, N. Severin, J.P. Rabe, and S. Hecht, *Synthesis of a novel chiral squaraine dye and its unique aggregation behavior in solution in self-assembled monolayers*. Advanced Materials (Weinheim, Germany), **18**: p. 1271-75,(2006).
20. T. Kobayashi, *J-aggregates*. 1996, Singapore: World Scientific Publishing Company.
21. K. Jyothish, M. Hariharan, and D. Ramaiah, *Chiral supramolecular assemblies of a squaraine dye in solution and thin films: Concentration-, temperature-, and solvent-induced chirality inversion*. Chemistry-a European Journal, **13**(20): p. 5944-5951,(2007).
22. S. Yagai, T. Seki, T. Karatsu, A. Kitamura, and F. Wurthner, *Transformation from H- to J-aggregated perylene bisimide dyes by complexation with cyanurates*. Angewandte Chemie-International Edition, **47**(18): p. 3367-3371,(2008).
23. S. Gadde, E.K. Batchelor, and A.E. Kaifer, *Controlling the Formation of Cyanine Dye H- and J-aggregates with Cucurbituril Hosts in the Presence of Anionic Polyelectrolytes*. Chem. Eur. J., **15**: p. 6025-31,(2009).
24. *Cobalt film of 1 nm was evaporated using an electron beam evaporator. Ethanol was used as the carbon feedstock with hydrogen as carrier at 62.7 standard cubic centimeters per minute. The reaction was carried out at 850 °C, producing uniform, dense nanotube networks. .*
25. J.H. Hafner, C.L. Cheung, T.H. Oosterkamp, and C.M. Lieber, *High-yield assembly of individual single-walled carbon nanotube tips for scanning probe microscopies*. Journal of Physical Chemistry B, **105**(4): p. 743-746,(2001).
26. L.M. Huang, B. White, M.Y. Sfeir, M.Y. Huang, H.X. Huang, S. Wind, J. Hone, and S. O'Brien, *Cobalt ultrathin film catalyzed ethanol chemical vapor deposition of single-*

- walled carbon nanotubes. *Journal of Physical Chemistry B*, **110**(23): p. 11103-11109,(2006).
27. *Interdigitated electrodes with spacing of 500  $\mu\text{m}$  were used for the device configuration. Devices were fabricated on 500 nm thick thermal oxide grown on highly doped silicon wafer.*
  28. J.L. Goldberg, X.-S. Wang, N.C. Bartelt, and E.D. Williams, *Surface height correlation functions of vicinal Si(111) surfaces using scanning tunneling microscopy*. *Surface Science Letters*, **249**: p. L285-92,(1991).
  29. J. Krim, I. Heyvaert, C.V. Haesendonck, and Y. Bruynseraede, *Scanning Tunneling Microscopy Observation of Self-Affine Fractal Roughness in Ion-Bombarded Film Surfaces*. *Physical Review Letters*, **70**: p. 57,(1993).
  30. G. Palasantzas, D. Tsamoras, and J.T.M. De Hosson, *Roughening aspects of room temperature vapor deposited oligomer thin films onto Si substrate*. *Surface Science*, **507-10**: p. 357-361,(2002).
  31. K. Vanormelingen, B. Degroote, and A. Vantomme, *Quantitative characterization of the surface morphology using a height difference correlation function*. *Journal of Vacuum Science & Technology B*, **24**(2): p. 725-729,(2006).
  32. M.S. Fuhrer, B.M. Kim, T. Durkop, and T. Brintlinger, *High-mobility nanotube transistor memory*. *Nano letters*, **2**(7): p. 755-759,(2002).
  33. J. Borghetti, V. Derycke, S. Lenfant, P. Chenevier, A. Filoramo, M. Goffman, D. Vuillaume, and J.P. Bourgoin, *Optoelectronic switch and memory devices based on*

- polymer-functionalized carbon nanotube transistors*. Advanced Materials, **18**(19): p. 2535,(2006).
34. *Calculated using the observed noise of 1% in conductance*.
  35. Y.M. Shi, X.C. Dong, H. Tintang, C.H. Weng, F.M. Chen, C.W. Lee, K.K. Zhang, Y. Chen, J.L. Wang, and L.J. Li, *Photoconductivity from Carbon Nanotube Transistors Activated by Photosensitive Polymers*. Journal of Physical Chemistry C, **112**(46): p. 18201-18206,(2008).
  36. T. Durkop, S.A. Getty, E. Cobas, and M.S. Fuhrer, *Extraordinary mobility in semiconducting carbon nanotubes*. Nano letters, **4**(1): p. 35-39,(2004).
  37. Toro, C.; De Boni, L.; Yao, S.; Ritchie, J. P.; Masunov, A. E.; Belfield, K. D.; Hernandez, *Linear and nonlinear optical characterizations of a monomeric symmetric squaraine-based dye in solution* F. E. J.Chem. Phys. **2009**, 130, 1-6.

## CHAPTER 7: CONCLUSIONS

In this dissertation, a variety of methods and application that utilize two-photon absorption was employed for a number of important and new organic materials. In Chapter 2, two squaraine dyes were studied and squaraine **1** had an impressive 2PA cross section of ca. 20,000 GM at 800 nm, and exhibited high photostability. Cytotoxicity tests resulted in ca. 80% cell viability up to 50  $\mu$ M concentration in HCT 116 and COS 7 cell lines. Therefore, one- and two-photon fluorescence microscopy imaging were demonstrated for the new squaraine probes **1** and a previously reported squaraine that had not been investigated as a fluorescent probe (**2**) in both cell lines, suggesting the potential utility of the probes for both conventional and two-photon based bioimaging. Nitroxides and their NOME analogs were examined as new NIR 2PA probes for investigating oxidative stress in CHO cells in Chapter 3. Nitroxides **19** and **47** were chosen based on their linear absorption and emission properties. CHO cells were used for both cell viability and oxidative stress studies, resulting in probes that were suitable up to 20  $\mu$ M concentration. After inducing oxidative stress with  $\text{H}_2\text{O}_2$ , colocalization experiments conducted in CHO cells with CellROX Deep Red (a commercial indicator of cellular oxidative stress) resulted very good colocalization (96%), supporting the role of the nitroxide probe as a suitable indicator of oxidative stress (damage) *in vitro*. The photophysical and amplified quenching properties of the anionic CPE based  $\text{PPESO}_3$  were studied and the results showed essentially an identical quenching effect under 1PA and 2PA, which means the same fluorescent state is populated via 2PA in Chapter 4. In order to improve supramolecular aggregation, a ROMP-based water soluble polymeric template, containing pendant amino groups, on the J-aggregation

properties of two porphyrin-based dyes (TSPP, **4**, and its amine-containing analog **5**) was investigated in Chapter 5. These results support the use of cationic polymer templates to enhance the J-aggregation in solution through possible attractive interaction between anionic porphyrin derivatives, facilitating the design of polymer-templated supramolecular aggregates. 2PA enhancement was observed for the porphyrin aggregates, with it being higher for the aggregates templated with the block copolymer, likely due to a greater degree of aggregation with the copolymer. Finally, in Chapter 6, the templating of aggregation of squaraine dyes with SWCNTs. The effect of processing conditions on aggregation, such as spin coating, solvent, and thermal annealing, were investigated. Through collaboration, this work was focused on a photosensitizing device and the result showed that an aggregate-functionalized nanotube network devices was approximately an order of magnitude better than those of similar nanotube devices.

Overall, exploiting fluorescent materials coupled with two-photon absorption-based methods opens the door to the development of new, sophisticated functional materials for a variety of biophotonic and optoelectronic applications. Future studies will involve *in vivo* and *ex vivo* bioimaging to fully investigate the potential of the new probes for deep tissue imaging. Additional research in the use of molecular aggregates in various nano-devices that can benefit by two-photon absorption is also envisioned.

## **APPENDIX A: PUBLICATIONS TO DATE FROM DISSERTATION WORK**

1. N-Alkylated aminopyrazines for use as hydrophilic optical agents, Amruta R. Poreddy, Bethel Asmelash, Karen P. Galen, Richard M. Fitch, Jeng-Jong Shieh, James M. Wilcox, Tasha M. Schoenstein, Jolette K. Wojdyla, Kimberly R. Gaston, John N. Freskos, William L. Neumann, Raghavan Rajagopalan, Hyo-Yang Ahn, James G. Kostelc, Martin P. Debreczeny, Kevin D. Belfield, Richard B. Dorshow, *Proc. of SPIE*, 7190, 71900P-1 (2009).
2. Femtosecond two-photon absorption measurements based on the accumulative photothermal effect and the Rayleigh interferometer, Luis Rodriguez, Hyo-Yang Ahn, Kevin D. Belfield, *Optics Expre.*, 17, 20, 19617-28 (2009).
3. Donor-Acceptor-Donor Fluorene derivatives for two-photon fluorescence lysosomal imaging, Sheng Yao, Hyo-Yang Ahn, Xuhua Wang, Jie Fu, Eric W. Van Stryland, David J. Hagan, and Kevin D. Belfield, *J. Org. Chem.*, 75, 3965–3974, (2010).
4. Folate receptor targeting silica nanoparticles probe for two-photon fluorescence bioimaging, Xuhua Wang, Sheng Yao, Hyo-Yang Ahn, Yuanwei Zhang, Mykhailo V. Bondar, Joseph A. Torres, and Kevin D. Belfield, *Biomed. Opt. Express*, Vol. 1, No. 2, (2010).
5. High-Fidelity hydrophilic probe for two-photon fluorescence lysosomal imaging, Xuhua Wang, Dao M. Nguyen, Ciceron O. Yanez, Luis Rodriguez, Hyo-Yang Ahn, Mykhailo V. Bondar, and Kevin D. Belfield, *J. Am. Chem. Soc.*, 132, 12237–12239, (2010).
6. Two-Photon Excited Fluorescence of a Conjugated Polyelectrolyte and Its Application in Cell Imaging, Anand Parthasarathy, Hyo-Yang Ahn, Kevin D. Belfield, and Kirk S. Schanze, *Appl. Mater. Interfaces*, 2 (10), pp 2744–2748, (2010).
7. Novel hydrophilic bis(1,2,3-triazolyl)fluorenyl probe for In vitro zinc ion sensing, Dao M. Nguyen, Xuhua Wang, Hyo-Yang Ahn, Luis Rodriguez, Mikhailo. V. Bondar, and Kevin D. Belfield, *Appl. Mater. Interfaces*, 2 (11), pp 2978–2981, (2010).

8. Integrin-targeting block copolymer probes for two-photon fluorescence bioimaging, Sanchita Biswas, Xuhua Wang, Alma R. Morales, Hyo-Yang Ahn, and Kevin D. Belfield, *Biomacromolecules*, 12 (2), pp 441–449, **(2011)**.
9. Photosensitization of carbon nanotubes using dye aggregates, Ryuichi Tsuchikawa, Hyo-Yang Ahn, S Yao, Kevin D Belfield, and Masa Ishigami, *J. Phys.: Condens. Matter*, 23, 202204, **(2011)**.

## **APPENDIX B: SUPPORTING INFORMATION OF CHAPTER 2**

### *1 Spectroscopic measurements*

The absorption spectra were measured by Agilent 8453 UV/Vis spectrophotometer. Fluorescence emission and excitation spectra were measured by PTI Quantamaster Spectrofluorimeter with a Hamamatsu R928 photomultiplier tube (PMT) in acetonitrile (ACN), 1, 2-dichloromethane (DCM), dimethyl sulfoxide (DMSO), methanol (MeOH), and tetrahydrofuran (THF).

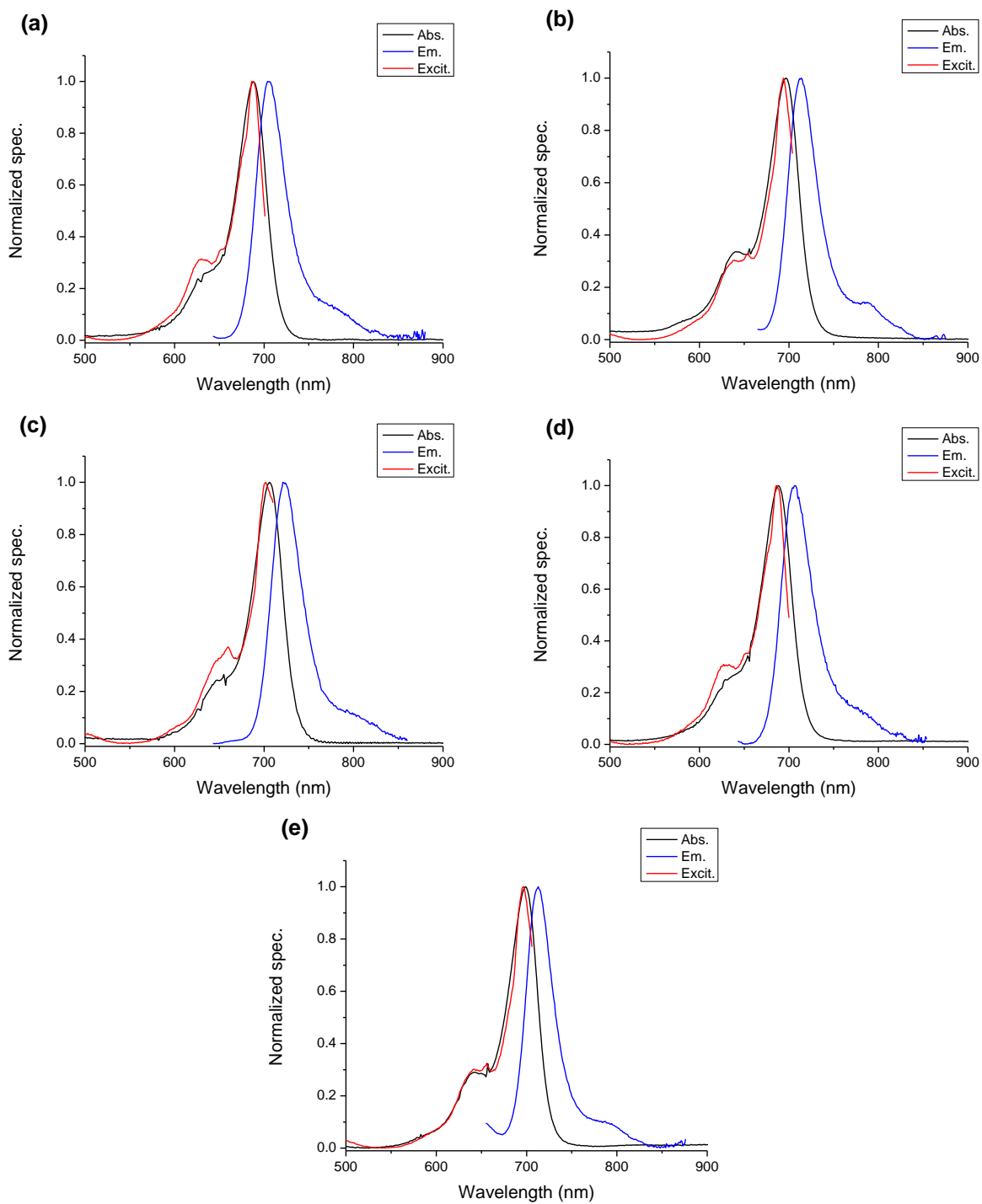


**Figure S 1.** Absorption, fluorescence emission, and excitation spectra of dye **1** in (a) ACN, (b) DCM, (c) DMSO, (d) MeOH, and (e) THF.

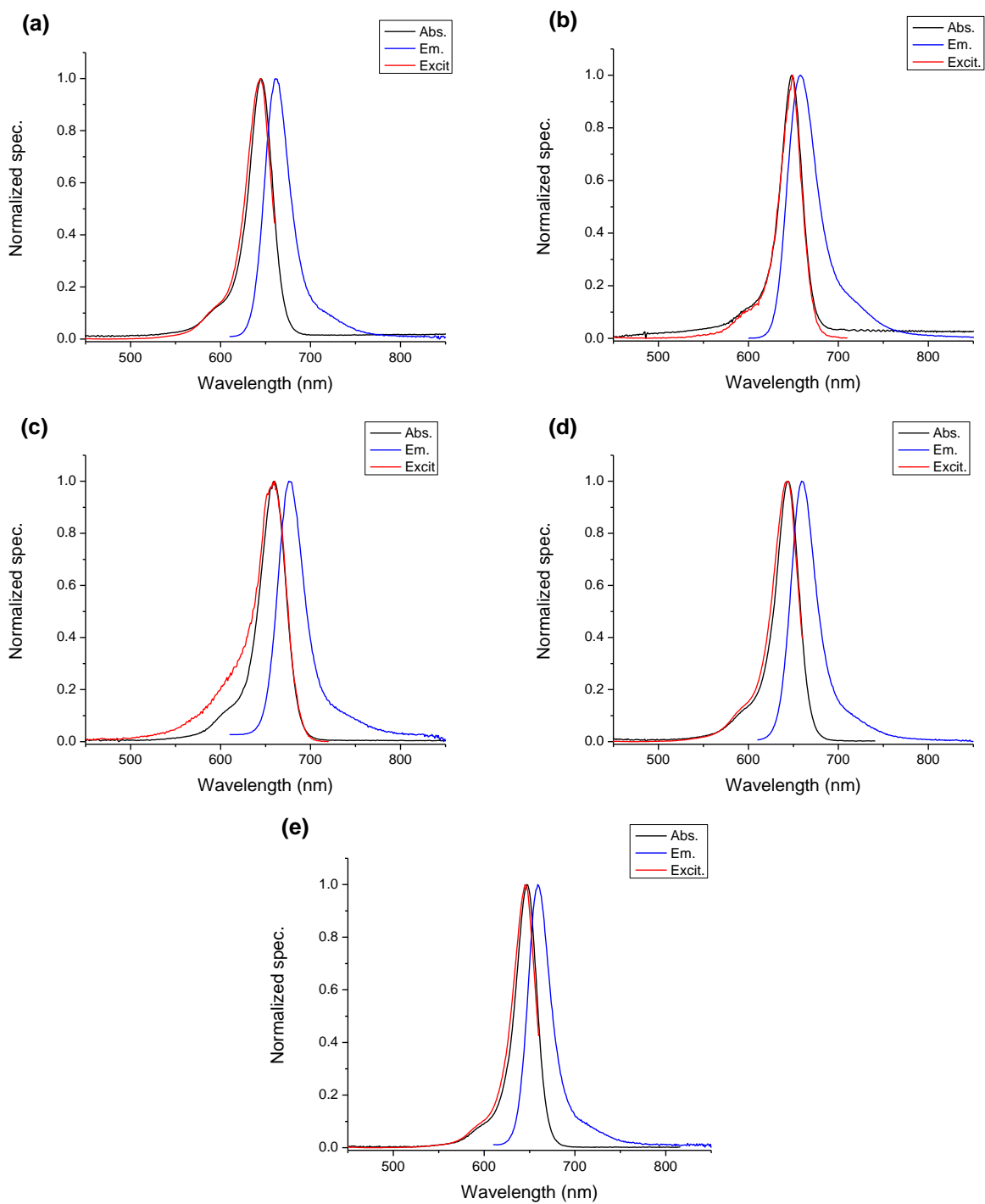


**Figure S 2.** Absorption, fluorescence emission, and excitation spectra of dye **2** in (a) ACN, (b) DCM, (c) DMSO, (d) MeOH, and (e) THF.

## 2 Photostability measurements

The photochemical stability test results of dye **1**, **2**, and Cy 5 (DiD oil, D 307, Invitrogen, Carlsbad, CA 92008) in DMSO were conducted by irradiating a 650 nm diode laser<sup>1</sup> of the degased solution in a 10 mm path length quartz cuvette. Kinetic changes in the absorption spectra were obtained with an Agilent 8453 UV/Vis spectrophotometer.

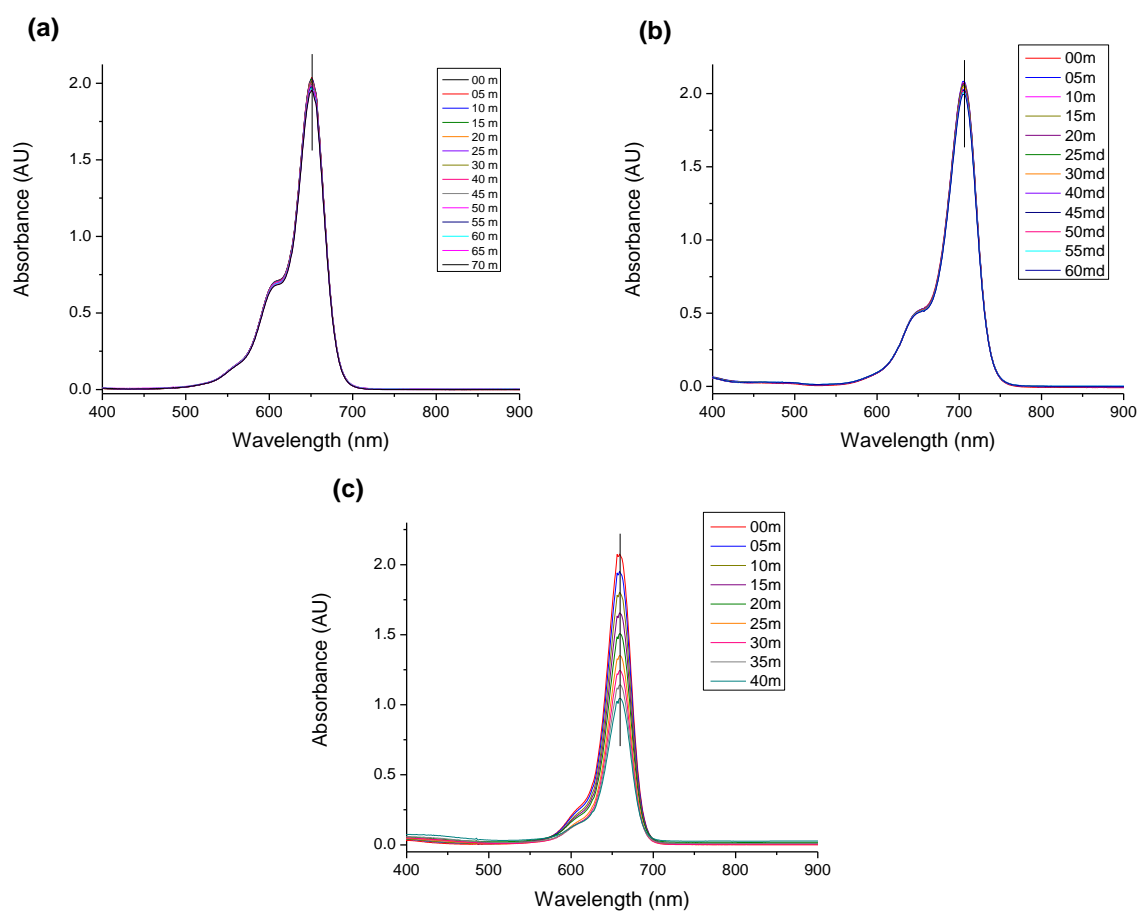


**Figure S 3.** Irradiation time-dependent absorption spectra of corresponding dyes by excited at 650 nm argon of (a) Cy 5, (b) dye 1, and (c) dye 2.

### 3 Linear and nonlinear properties of Cy 5

The absorption and fluorescence emission spectra were measured in DMSO by Agilent 8453 UV/Vis spectrophotometer and PTI Quantamaster Spectrofluorimeter, respectively. 2PA measurement were performed by a using tunable Ti:Sapphire laser system (Coherent MIRA 900, pulse duration ~200 fs/pulse (FWHM), repetition rate 76 MHz) coupled with PTI system.

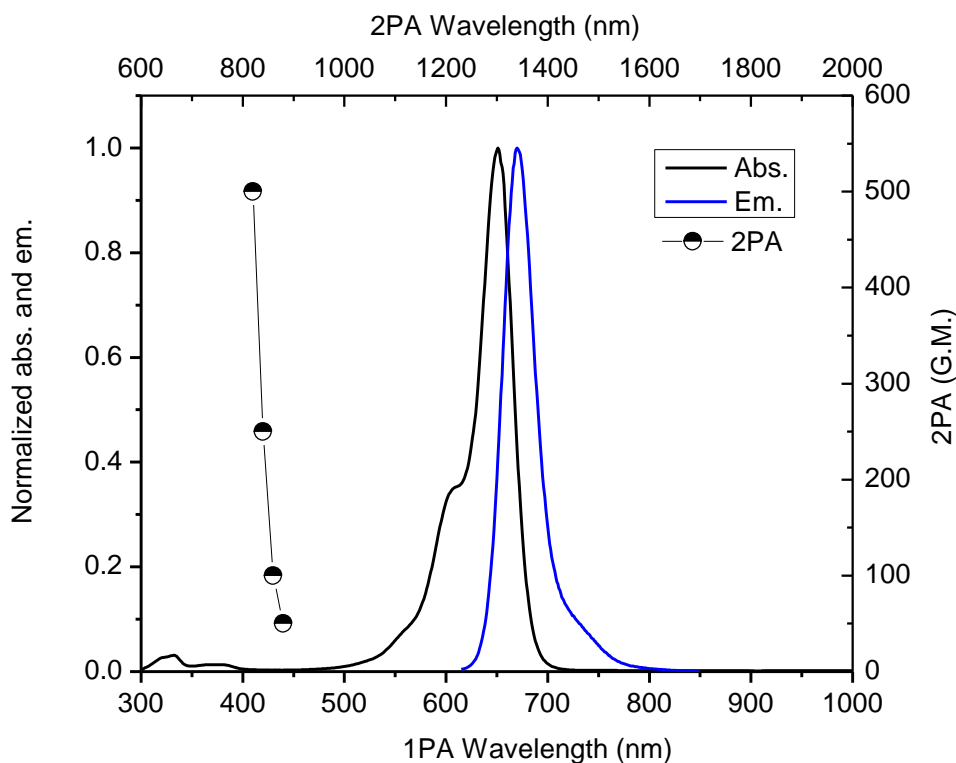


**Figure S 4.** Linear and non-linear property spectra of Cy 5 (1 GM (Göppert Meyer) =  $10^{-50} \text{ cm}^4 \text{ s/photon}^{-1}$ , uncertainty of the 2PA value = 15 %).

#### 4 Linear and nonlinear properties of micelles

The open aperture Z-scan method was performed using a Ti:Sapphire amplified system (Coherent, MIRA and Legend) with an optical parametric amplifier (model OPerA) providing laser pulses ~100 fs (FWHM) duration with 1 kHz repetition rate. The concentration of solutions was  $\sim 10^{-3}$  M in a 1 mm quartz cuvette at room temperature. (Sheik-bahae, Said et al. 1990)

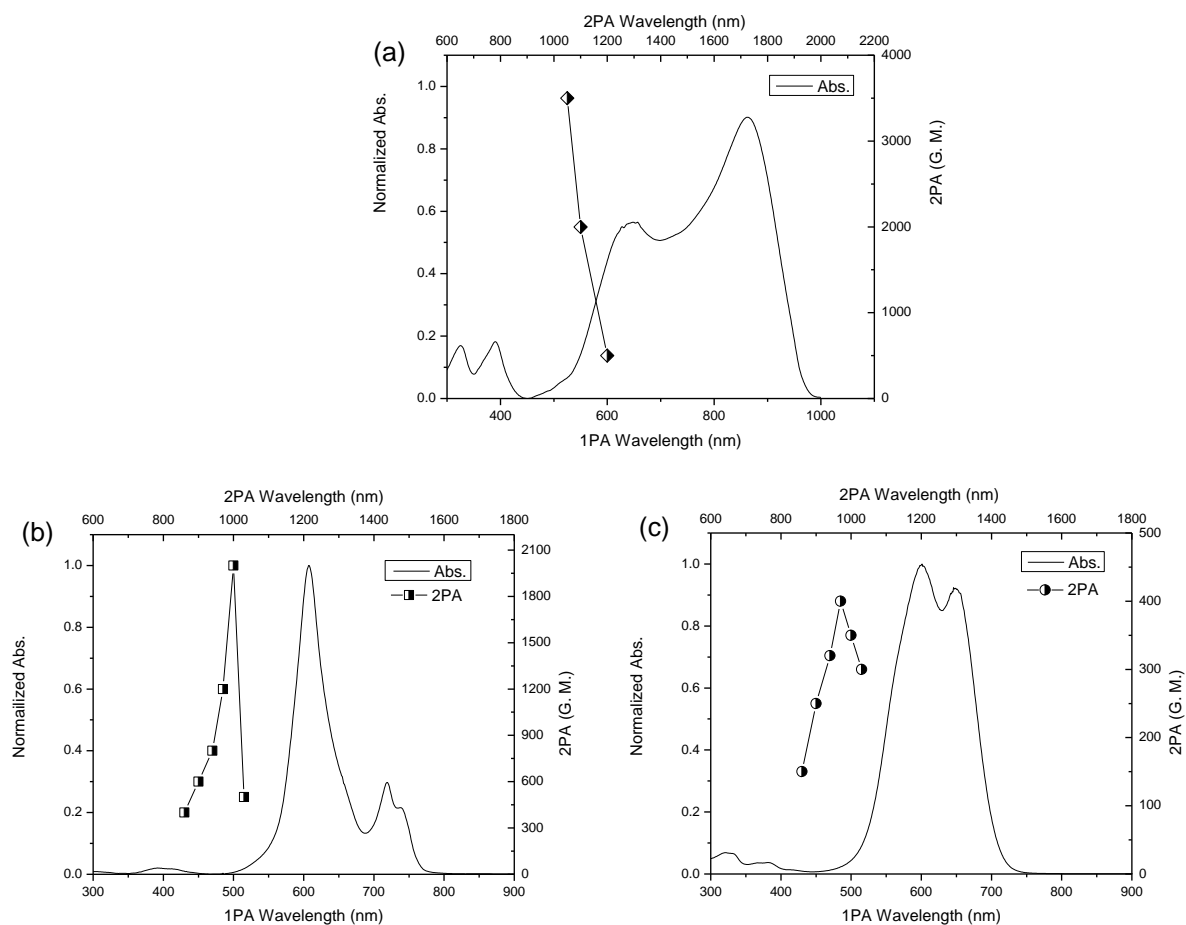


**Figure S 5.** Linear and non-linear property spectra of the micelles of (a) dye 1, (b) dye 2, and (c) Cy 5 (error  $\pm 25\%$ ).

*5  $^1\text{H}$  NMR and  $^{13}\text{C}$  NMR spectra*

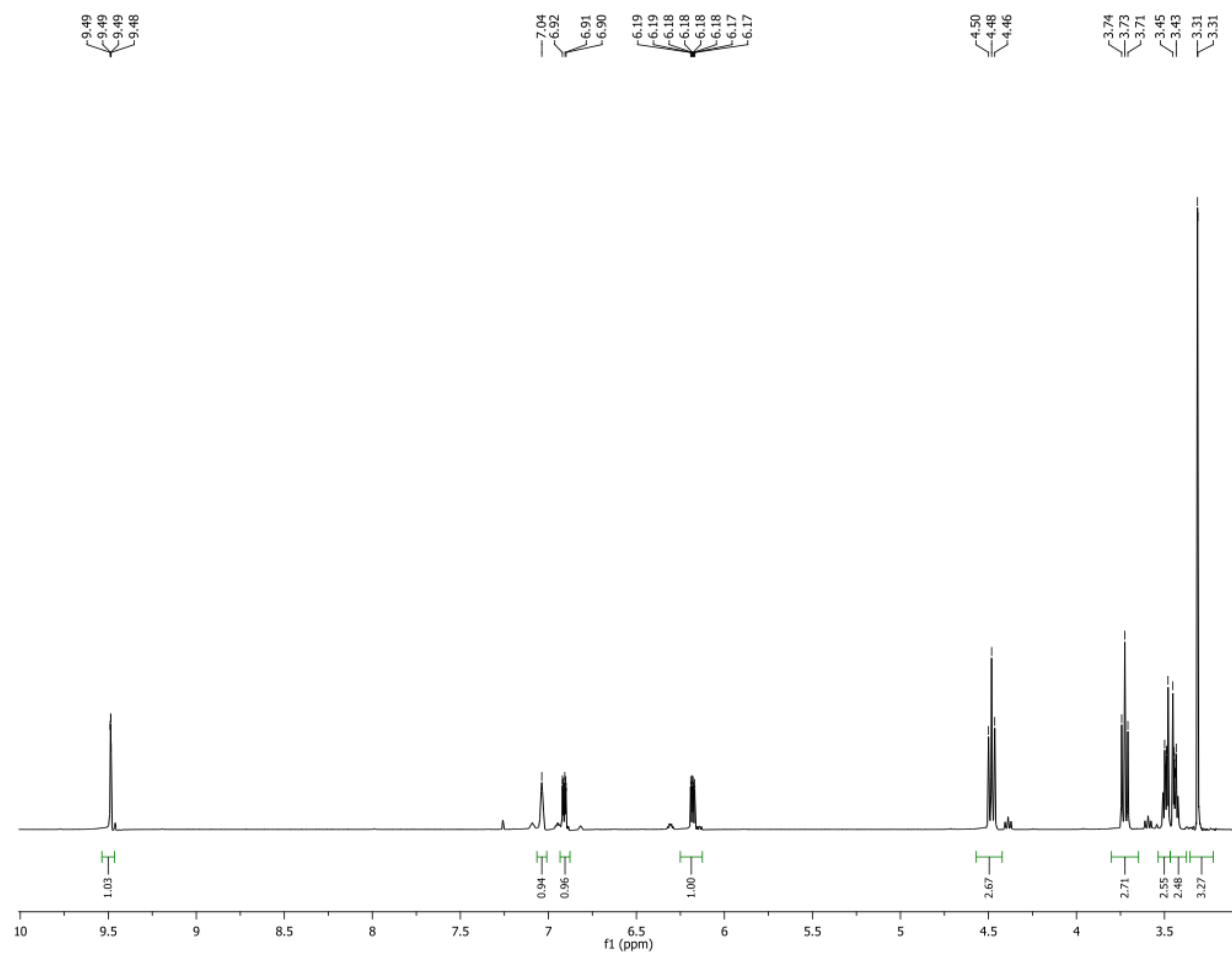


**Figure S 6.**  $^1\text{H}$  NMR spectrum of compound 3.

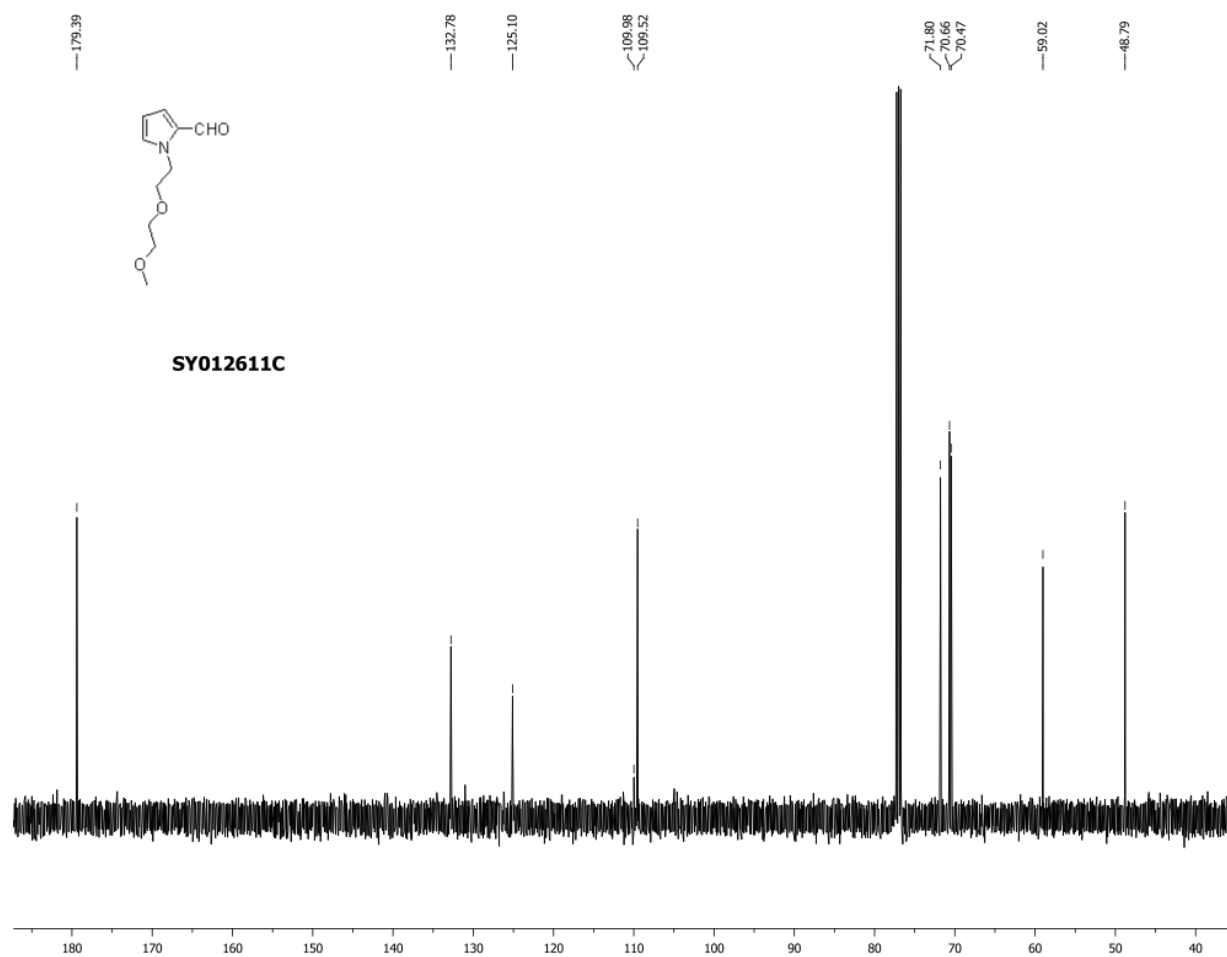


**Figure S 7.**  $^{13}\text{C}$  NMR spectrum of compound 3.

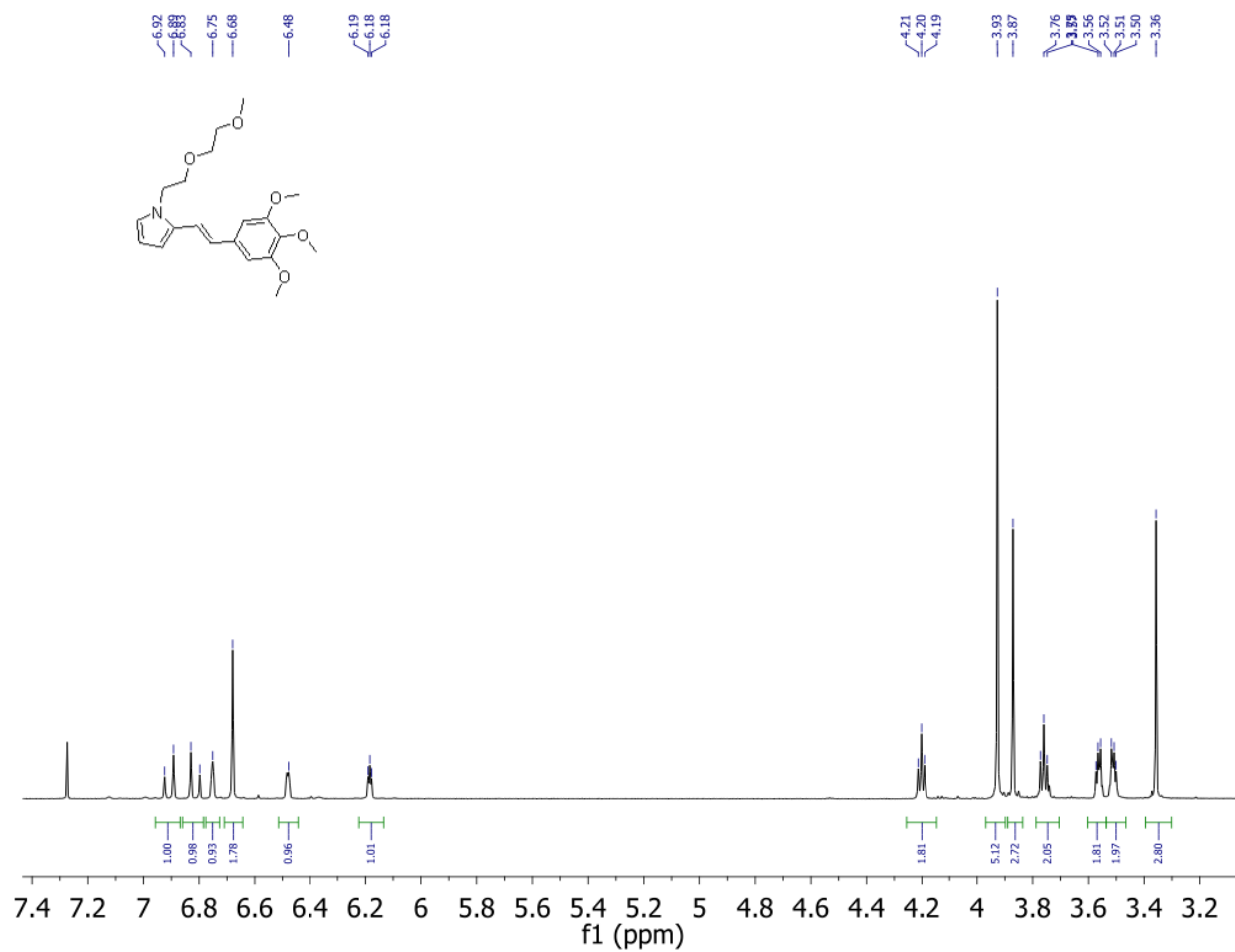


**Figure S 8.** <sup>1</sup>H NMR spectrum of compound 4.

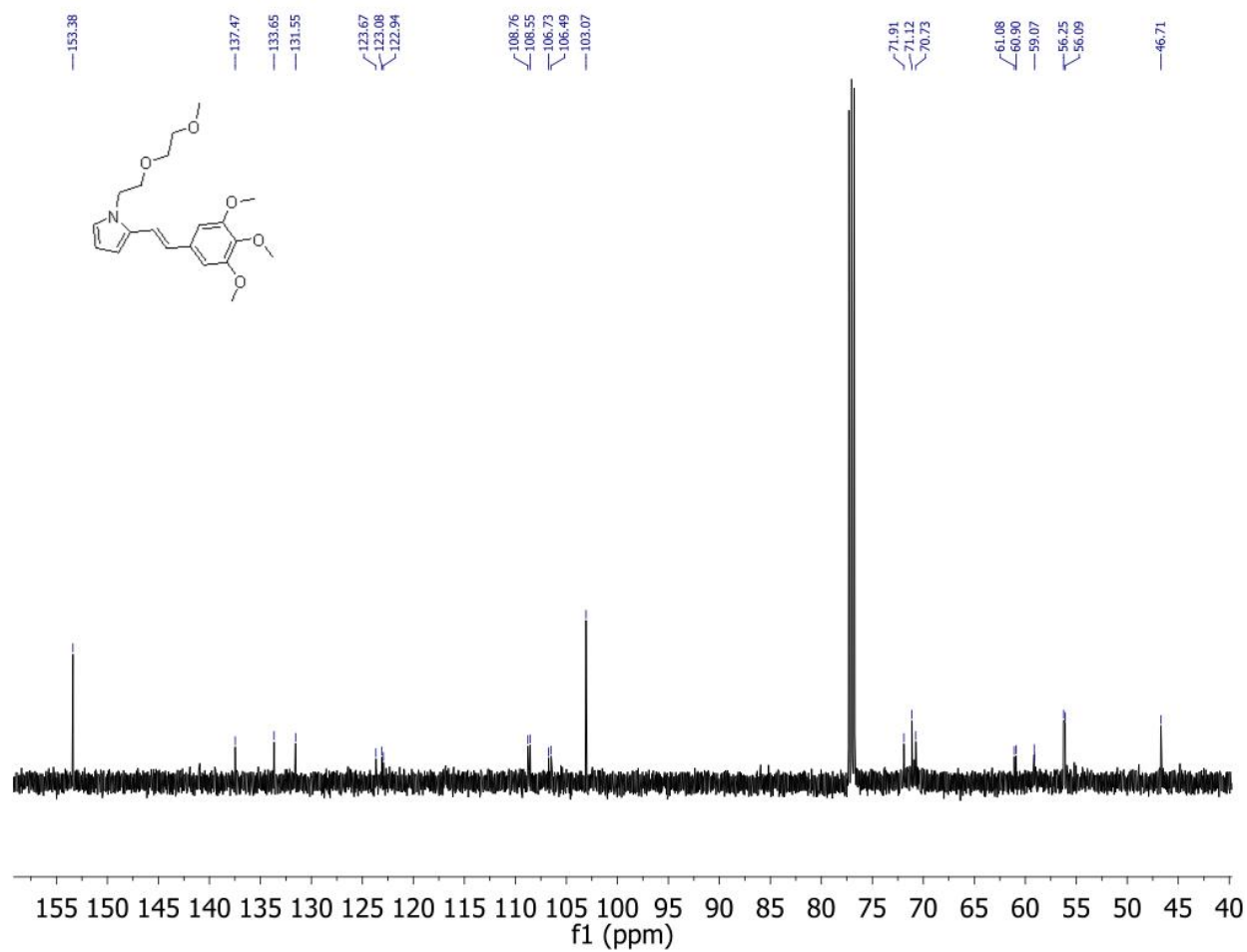


**Figure S 9.** <sup>13</sup>C NMR spectrum of compound **4**.

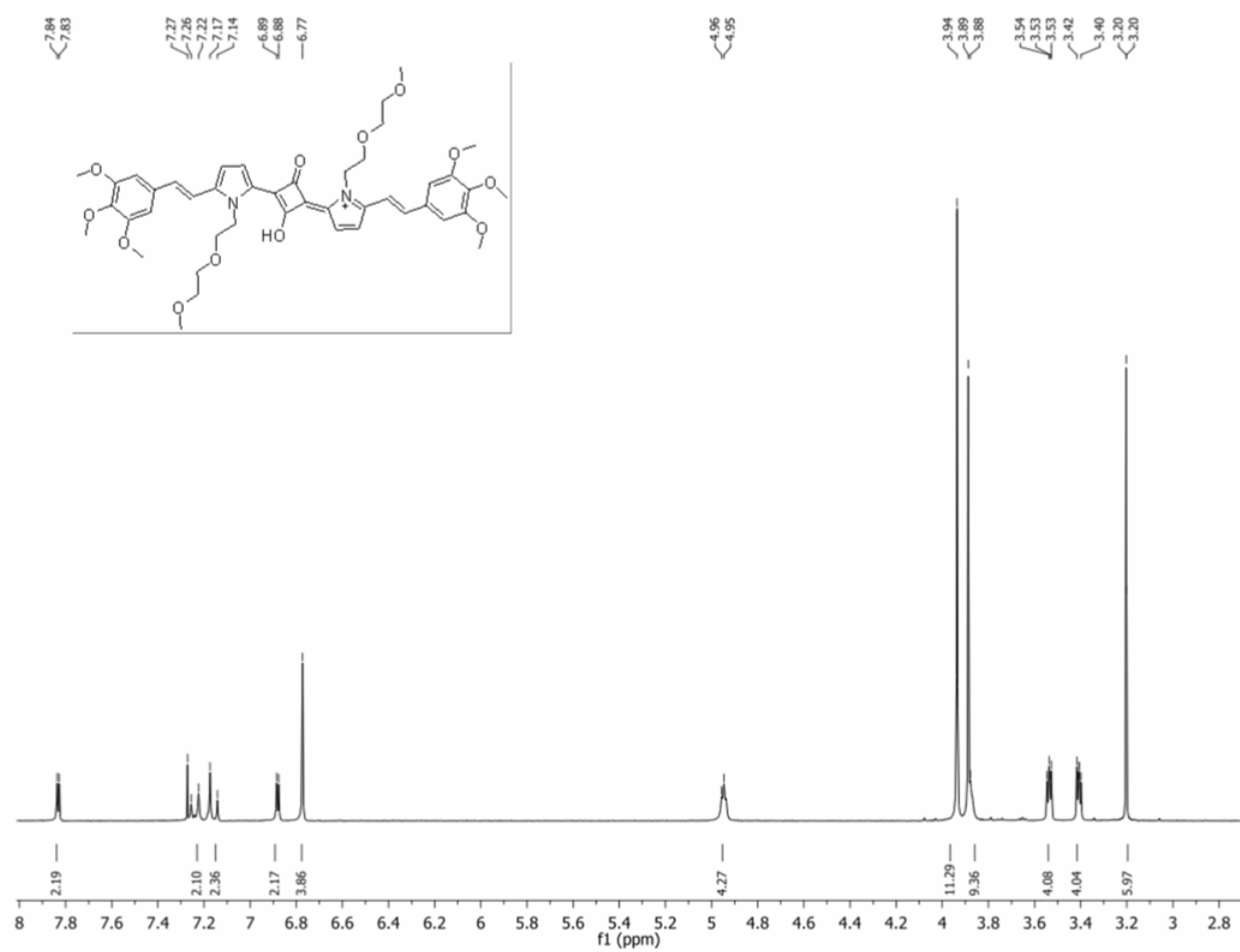


**Figure S 10.**  $^1\text{H}$  NMR spectrum of squaraine dye 1.



1. Corredor, C. C.; Belfield, K. D.; Bondar, M. V.; Przhonska, O. V.; Yao, S., One- and two-photon photochemical stability of linear and branched uorene derivatives. *J. Photochem. Photobiol., A* **2006**, *184*, 105-112.
2. Sheik-bahae, M.; Said, A. A.; Wei, T.-h.; Hagan, D. J.; Van Stryland, E. W., Sensitive Measurement of Optical Nonlinearities Using a Single Beam. *IEEE J. Quantum Electron.* **1990**, *26* (4), 760-769.

## **APPENDIX C: SUPPORTING INFORMATION OF CHAPTER 3**

## 1 Spectroscopic measurements

Steady state absorption spectra were measured with an Agilent 8453 UV-vis spectrophotometer. Fluorescence emission spectra were measured using a PTI Quantamaster Spectrofluorimeter with a Hamamatsu R928 photomultiplier tube (PMT) in cyclohexane (CHX) and CH<sub>2</sub>Cl<sub>2</sub>. All solvents were spectroscopic grade.

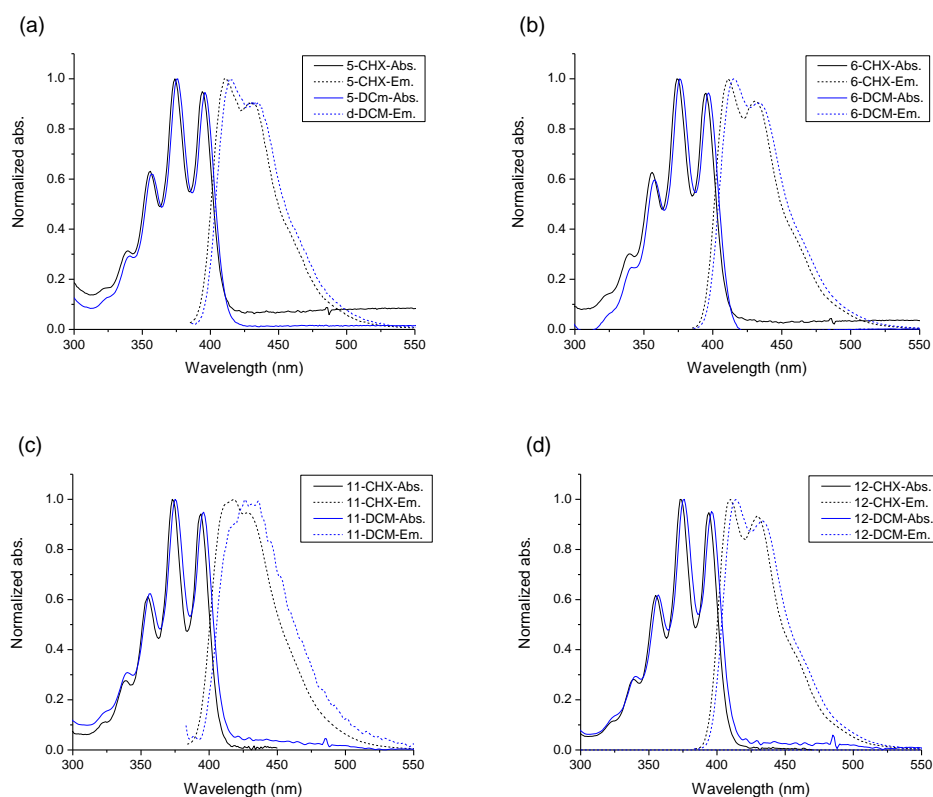


**Figure S1.** Steady state absorption and emission spectra in cyclohexane and dichloromethane of diphenylanthracene derivatives (a) **5**, (b) **6**, (c) **11**, and (d) **12**.

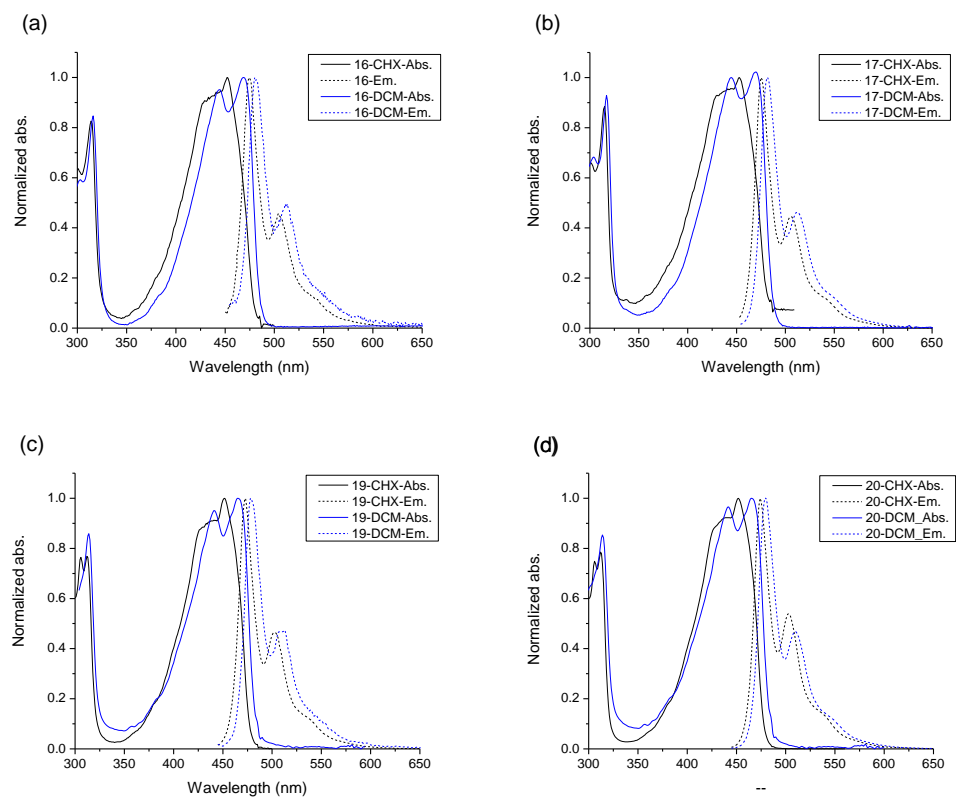


**Figure S2.** Steady state absorption and emission spectra in cyclohexane and dichloromethane of bis(phenylethynyl) derivatives (a) **16**, (b) **17**, (c) **19**, and (d) **20**.

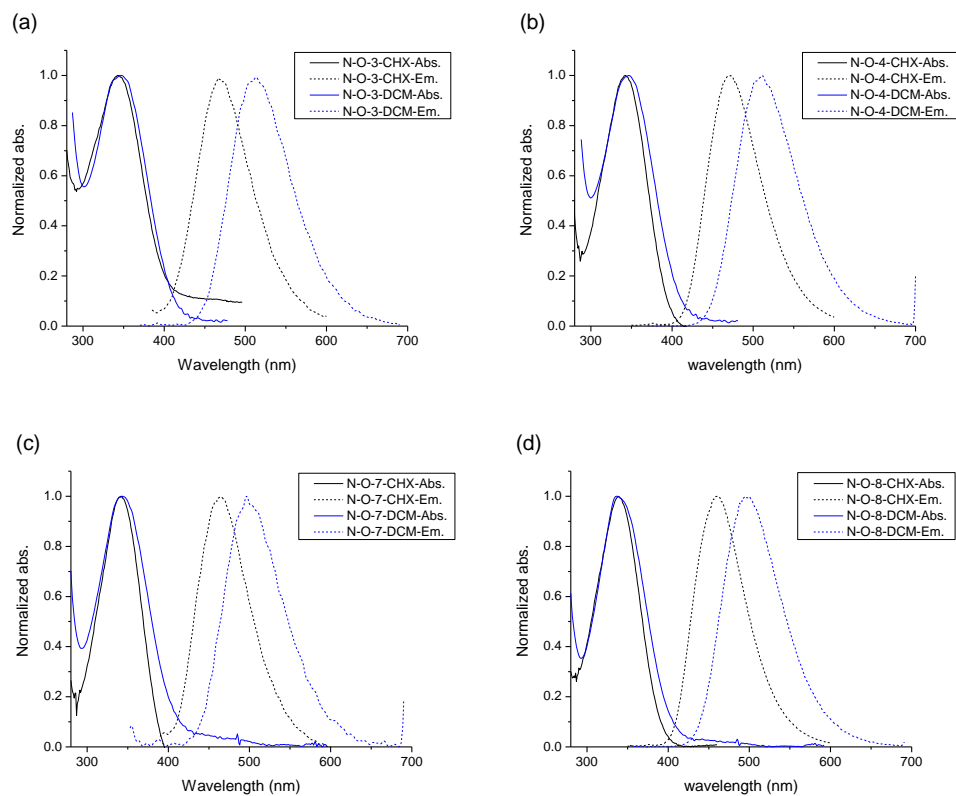


**Figure S3.** Steady state absorption and emission spectra in cyclohexane and dichloromethane of Dansyl sulfonamide derivatives DS-N- (a) **3**, (b) **4**, (c) **7**, and (d) **8**.

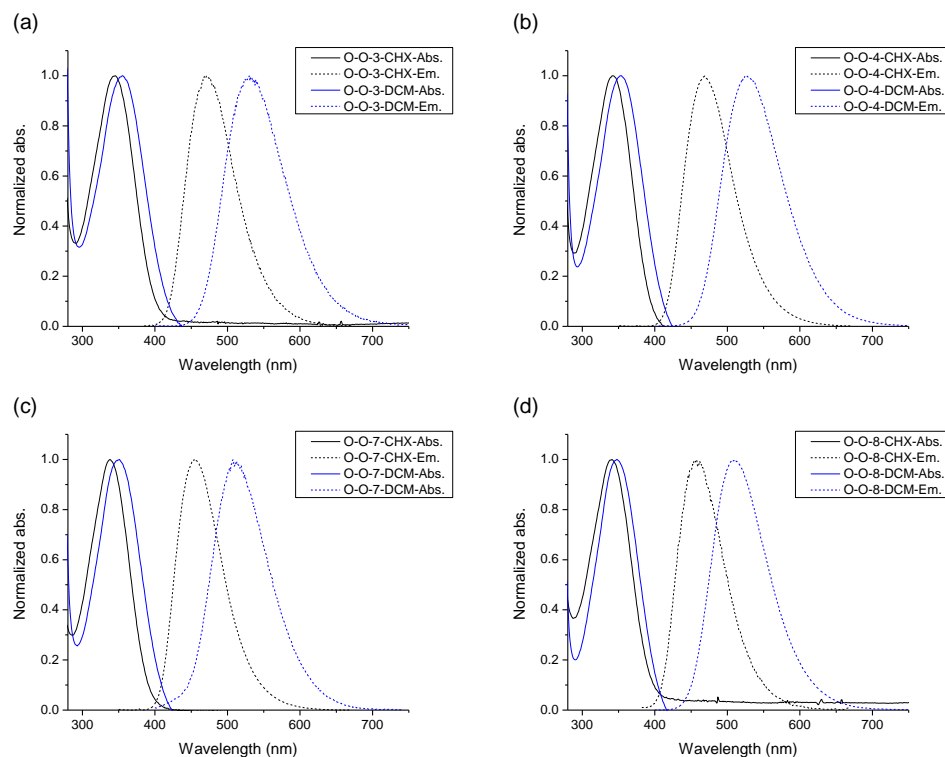


**Figure S4.** Steady state absorption and emission spectra in cyclohexane and dichloromethane of Dansyl sulfon-ester derivatives DS-O- (a) **3**, (b) **4**, (c) **7**, and (d) **8**.

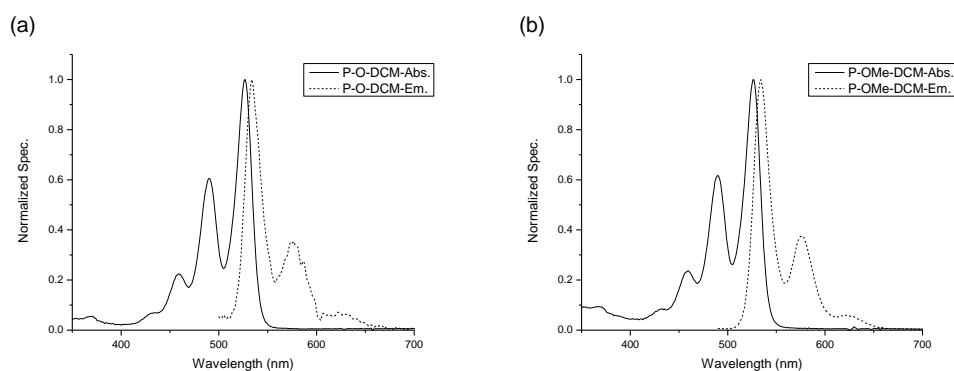


**Figure S5.** Steady state absorption and emission spectra in cyclohexane and dichloromethane of perylene (a) radical and (b) methoxy derivatives.

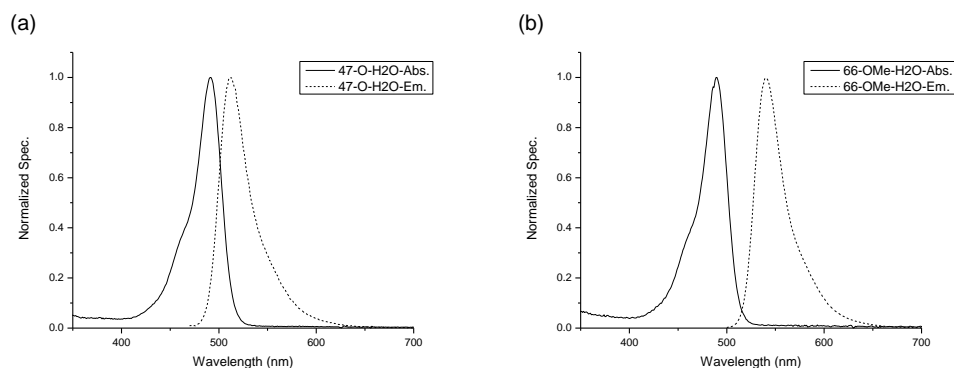


**Figure S6.** Steady state absorption and emission spectra in cyclohexane and dichloromethane of fluorescein (a) radical (**47**) and methoxy (**66**) derivatives.

## 2 1PFM images

A Leica TCS SP5 MP confocal microscope system was used for 1PFM imaging. The same microscope coupled to a Coherent Chameleon Vision S Ti:sapphire laser system (~ 70 fs (FWHM), 90 MHz repetition rate) was used for 2PFM imaging. In both 1PFM and 2PFM, a 63x (Leica 506279) objective was utilized for *in vitro* cell imaging. Figures S7-S12 are 1PFM at different concentrations of nitroxide probe and oxidative stress inducer (H<sub>2</sub>O<sub>2</sub>).

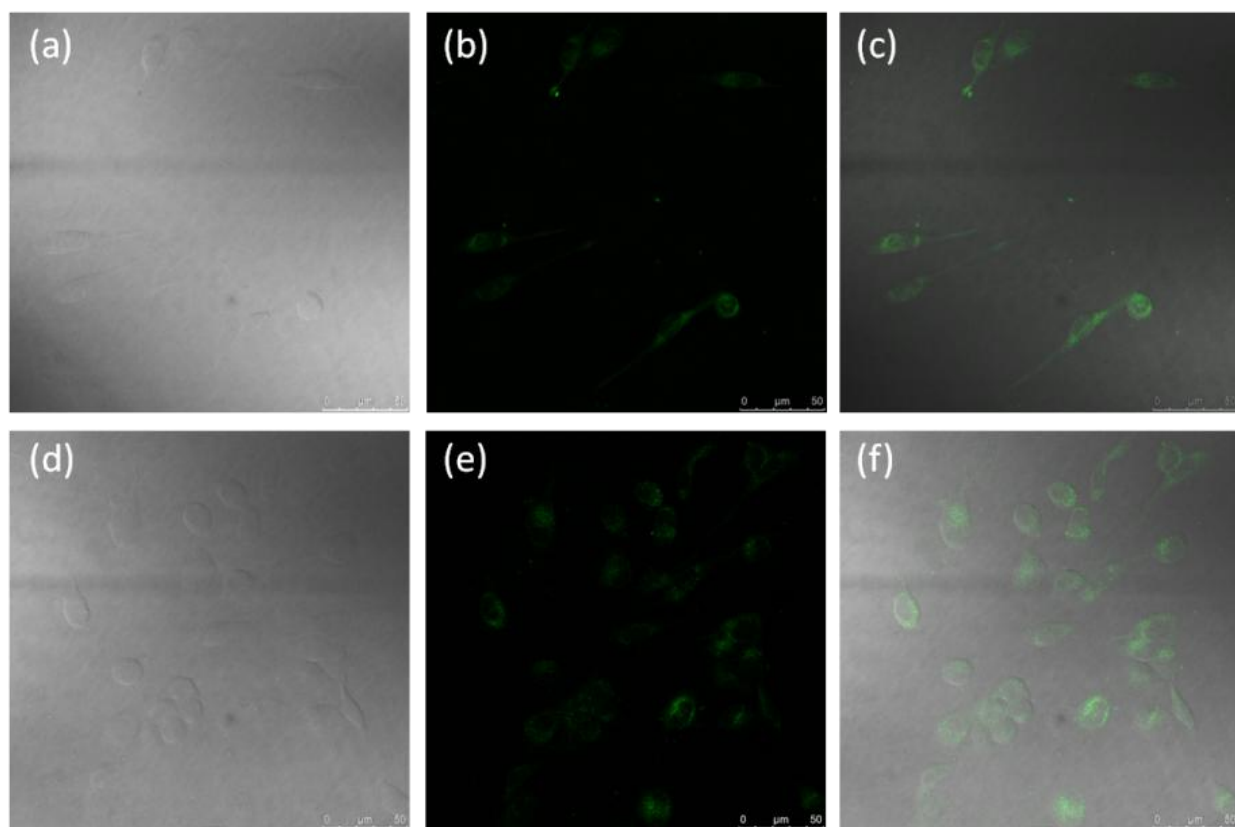


**Figure S7.** CHO cells with nitroxide 19 at 5 $\mu$ M concentration (a) DIC, (b) 1PFM image, (c) overlaid image of (a) and (b) and 10  $\mu$ M concentration (d) DIC, (e) 1PFM image, and (e) overlaid image of (d) and (e).

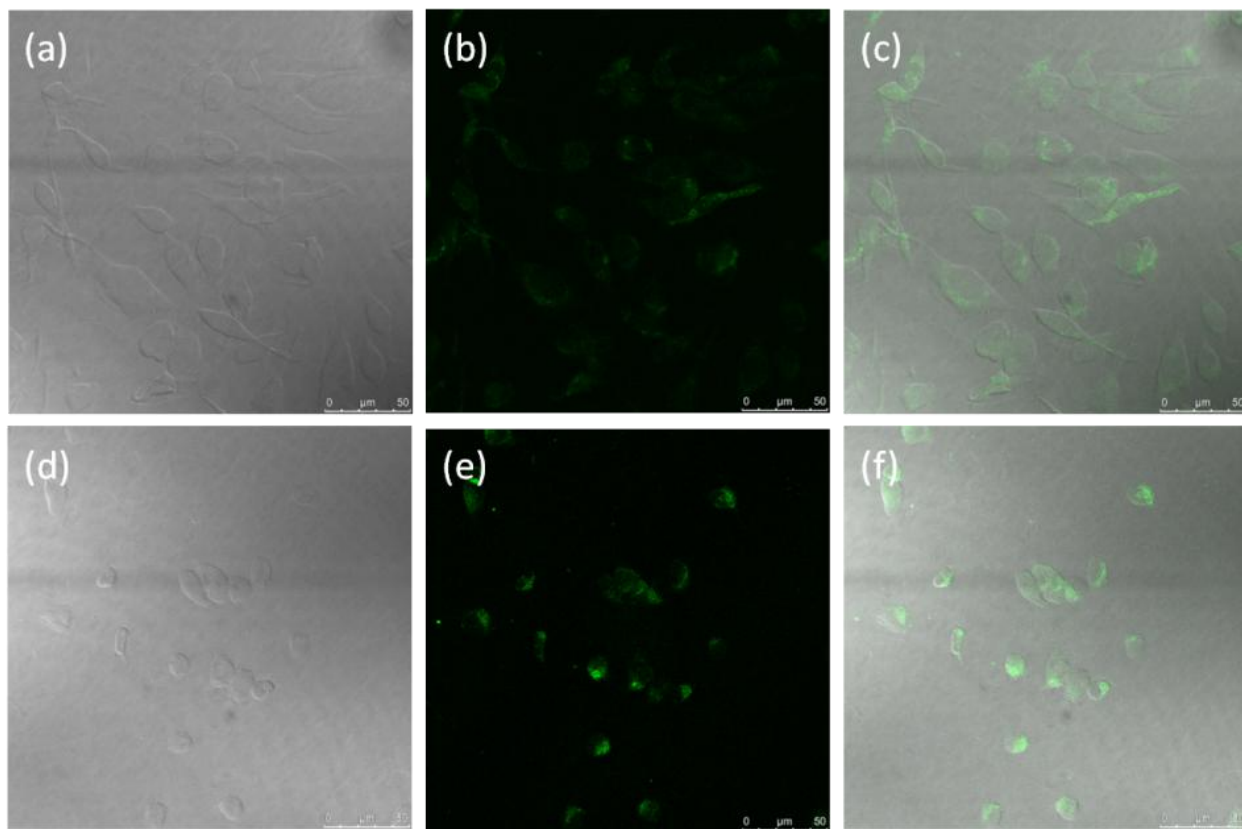


**Figure S8.** CHO cells with nitroxide **19** at 5  $\mu\text{M}$  concentration with 100  $\mu\text{M}$   $\text{H}_2\text{O}_2$  (a) DIC, (b) 1PFM image, (c) overlaid image of (a) and (b), and 5  $\mu\text{M}$  concentration with 200  $\mu\text{M}$   $\text{H}_2\text{O}_2$  (d) DIC, (e) 1PFM image, and (f) overlaid image of (d) and (e).

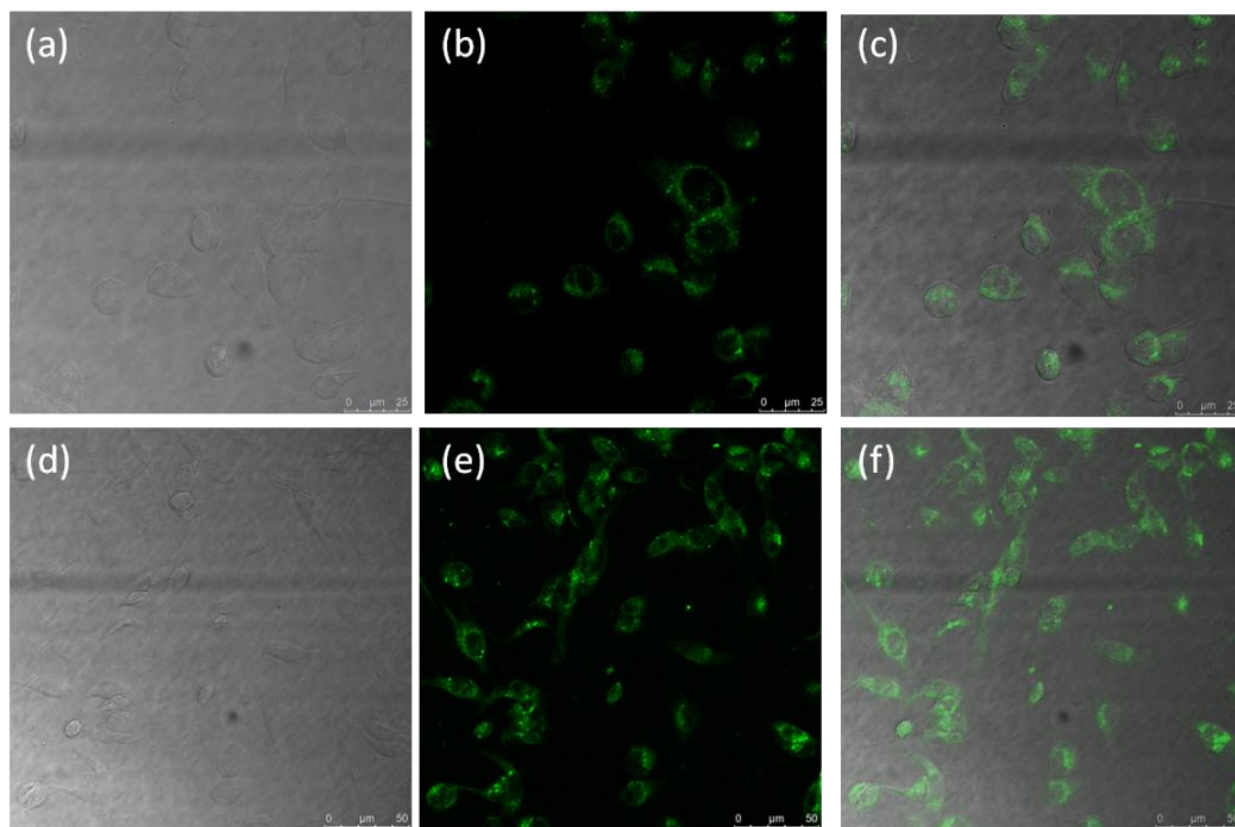


**Figure S9.** CHO cells with nitroxide **19** at 10  $\mu\text{M}$  concentration with 100  $\mu\text{M}$   $\text{H}_2\text{O}_2$  (a) DIC, (b) 1PFM image, (c) overlaid image of (a) and (b), and 10  $\mu\text{M}$  concentration with 200  $\mu\text{M}$   $\text{H}_2\text{O}_2$  (d) DIC, (e) 1PFM image, and (f) overlaid image of (d) and (e).

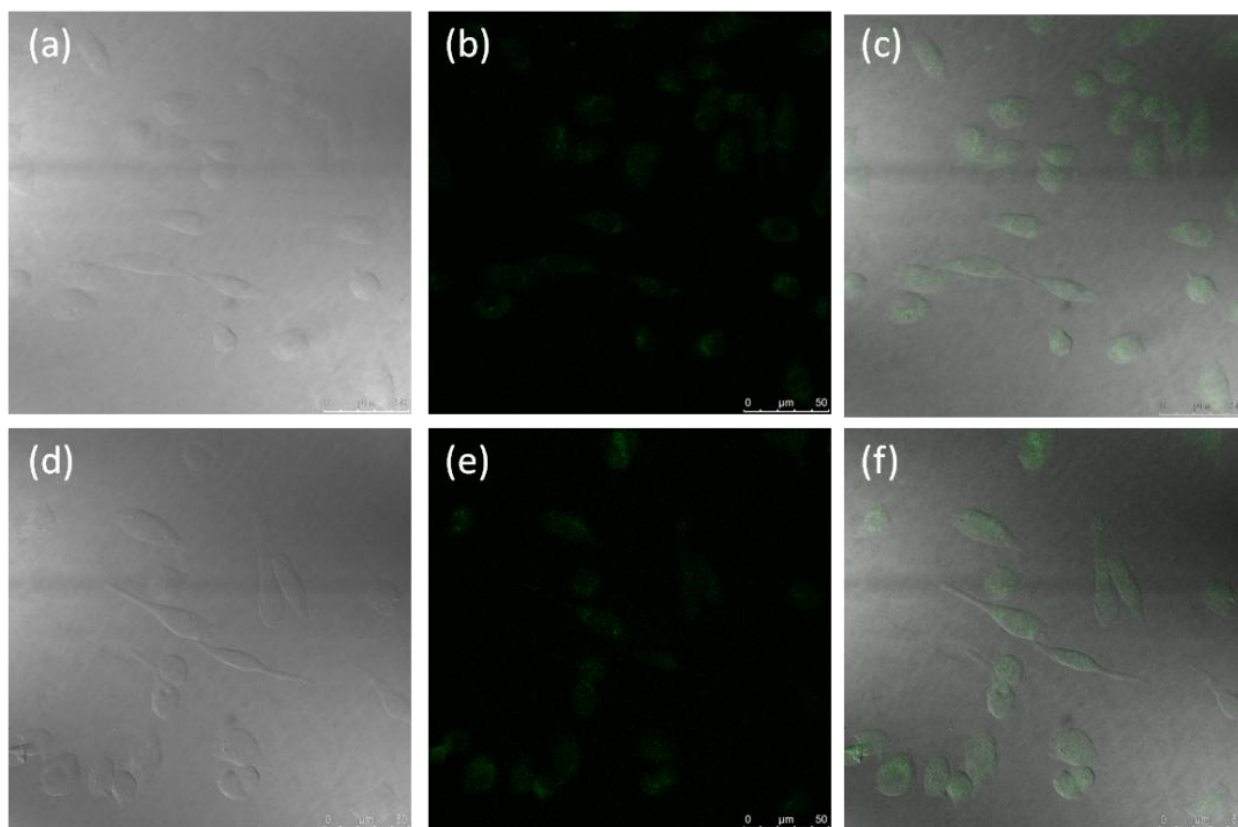


**Figure S10.** CHO cells with nitroxide **47** at 5 μM concentration (a) DIC, (b) 1PFM image, (c) overlaid image of (a) and (b) and 10 μM concentration (d) DIC, (e) 1PFM image, and (e) overlaid image of (d) and (e).

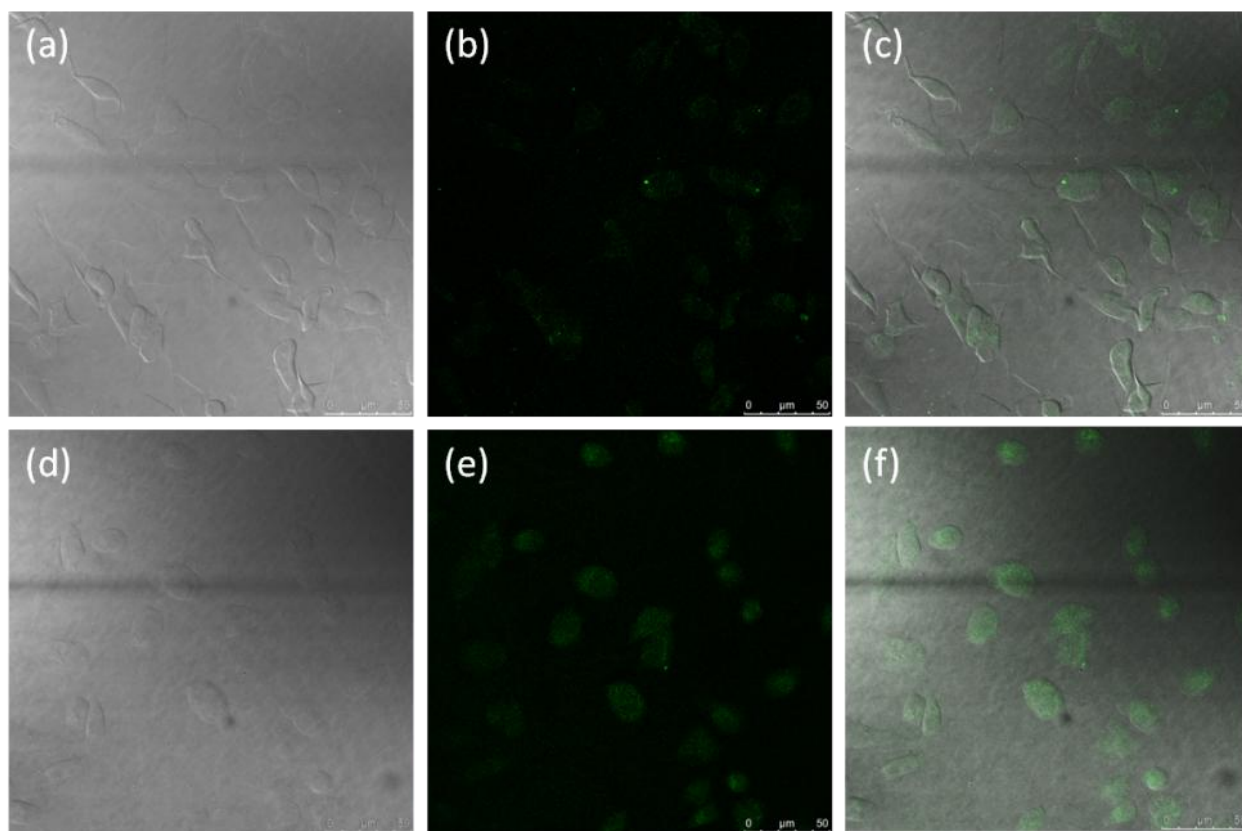


**Figure S11.** CHO cells with nitroxide **47** at 5  $\mu\text{M}$  concentration with 100  $\mu\text{M}$   $\text{H}_2\text{O}_2$  (a) DIC, (b) 1PFM image, (c) overlaid image of (a) and (b), and 5  $\mu\text{M}$  concentration with 200  $\mu\text{M}$   $\text{H}_2\text{O}_2$  (d) DIC, (e) 1PFM image, and (f) overlaid image of (d) and (e).

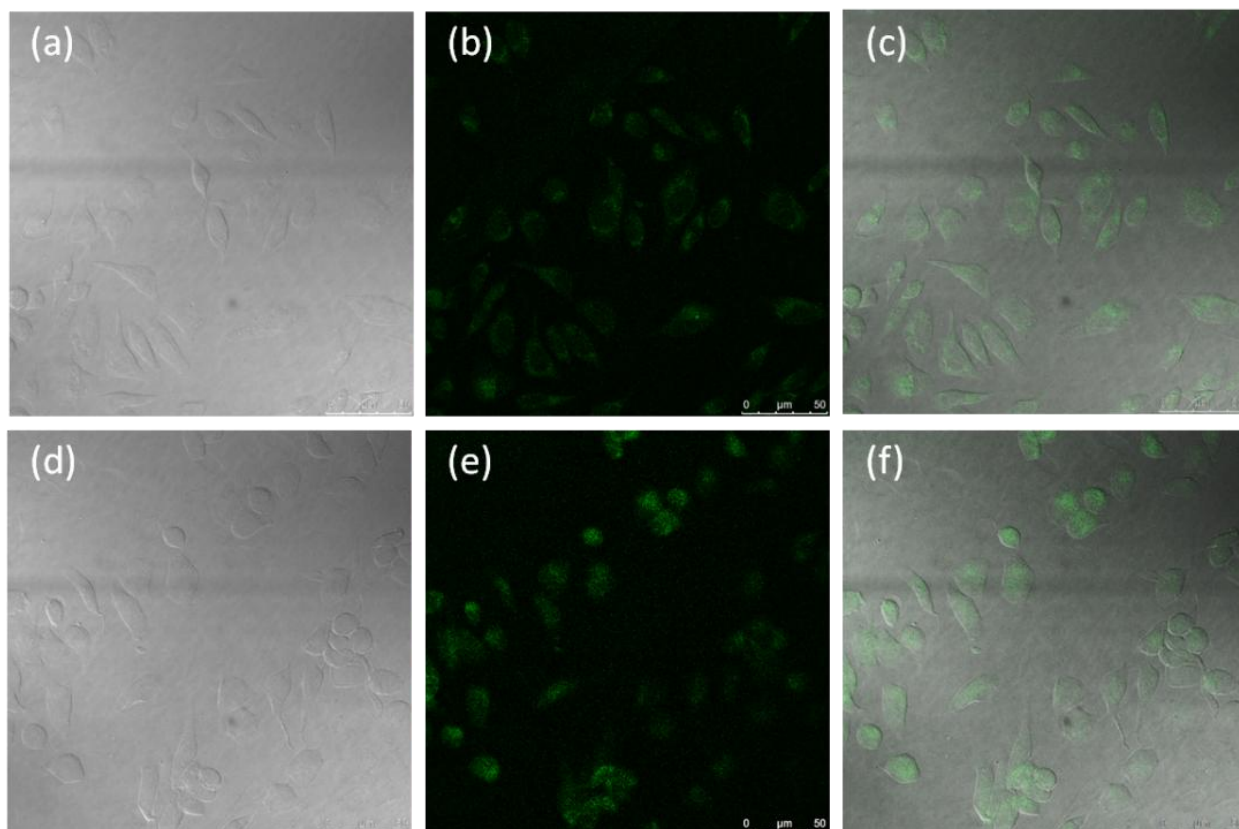


**Figure S12.** CHO cells with nitroxide **47** at 10 μM concentration with 100 μM H<sub>2</sub>O<sub>2</sub> (a) DIC, (b) 1PFM image, (c) overlaid image of (a) and (b), and 10 μM concentration with 200 μM H<sub>2</sub>O<sub>2</sub> (d) DIC, (e) 1PFM image, and (f) overlaid image of (d) and (e).

## **APPENDIX D: SUPPORTING INFORMATION OF CHAPTER 4**

### **Cell line**

The HeLa cells were purchased from ATCC (America Type Culture Collection, Manassas, VA, USA). All cells were incubated at 37 °C in a 95% humidified atmosphere containing 5% CO<sub>2</sub> in Minimum Essential Media (MEM, Invitrogen, Carlsbad, CA, USA), supplemented with 10% fetal bovine serum (FBS, Atlanta Biologicals, Lawrenceville, GA, USA), and 100 units/mL penicillin-streptomycin (Atlanta Biologicals, Lawrenceville, GA, USA).

### **Cytotoxicity Assay**

HeLa cells were prepared for the cytotoxicity test in 96-well plates  $5 \times 10^3$  cells per well that were incubated in 90 µL of MEM medium without phenol red, supplemented with 10% FBS and 100 units/mL penicillin-streptomycin. The cells were then incubated for additional 20 h with PPESO<sub>3</sub> polymer (0.01 µM, 0.1 µM, 1 µM, 5 µM, and 10 µM) and silica nanoparticles with PPESO<sub>3</sub> polymer (0.1 µg/mL, 5 µg/mL, 20 µg/mL, 30 µg/mL, and 50 µg/mL). Subsequently, 20 µL of CellTiter 96® AQueous One Solution reagent (MTS assay) was added into each well, followed by further incubation for 4 h at 37 °C. The relative viability of the cells incubated with PPESO<sub>3</sub> polymer or with PPESO<sub>3</sub> polymer silica nanoparticles to untreated cells was determined by measuring the MTS-formazan absorbance on a Kinetic microplate reader (Spectra Max M5, Molecular Devices, Sunnyvale, CA, USA) at 490 nm with subtraction of the absorbance of cell-free blank volume at 490 nm. The results from three individual experiments were averaged.

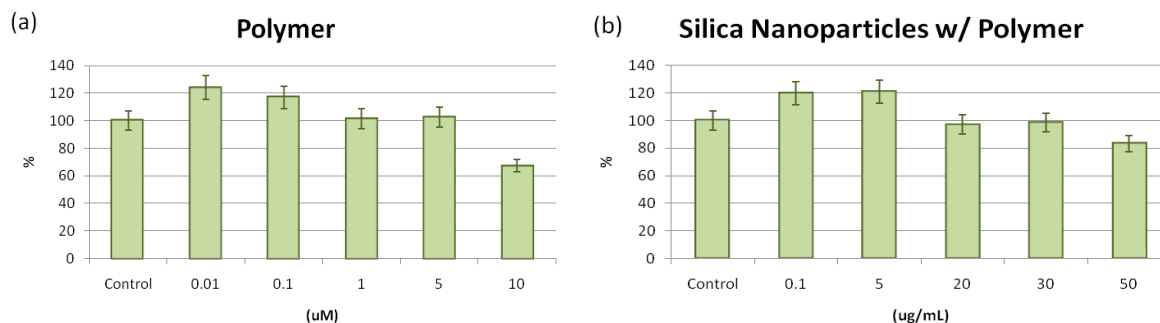


**Figure S-1.** Cytotoxicity test (A) with  $\text{PPESO}_3$  polymer and (B) with  $\text{PPESO}_3$  silica nanoparticles (error bar =  $\pm 7\%$ ).

Based on the cell viability test results (Figure S1), the all concentrations except the highest concentration were appropriate for imaging. Since  $\text{PPESO}_3^-$  silica nanoparticle 0.1  $\mu\text{g/mL}$  concentration and  $\text{PPESO}_3$  polymer 0.01  $\mu\text{M}$  concentration were too low (not enough fluorescence observed), the three mid-range concentrations were employed.

### Cell imaging

HeLa cells were placed onto poly-D-lysine coated glasses in 24-well plates (40,000 cells per well), and the cells were incubated for 48 h before incubating with the object. Stock solution of  $\text{PPESO}_3$  polymer was prepared as 1.4 mM solution in water while a stock solution of  $\text{PPESO}_3$  silica particles was prepared as 500  $\mu\text{g/mL}$  solution in water. The solution was diluted to each concentration with complete growth medium, Minimum Essential Media (MEM), and then freshly placed over the cells. After incubation for 2 h, cells were washed with PBS (3–5X) 7 times and fixed using 4% formaldehyde solution for 15 min at 37 °C and then 0.5 mL/well

NaBH<sub>4</sub> (1mg/mL) solution in PBS (pH=8.0), which was prepared by adding a few drops of 6N NaOH solution into PBS (pH=7.2), for 15 min to decrease the auto-fluorescence. The last step was repeated. The plates were then washed 3 times with PBS and twice with water. Finally, the glass coverslips were mounted using Prolong Gold mounting media for microscopy.

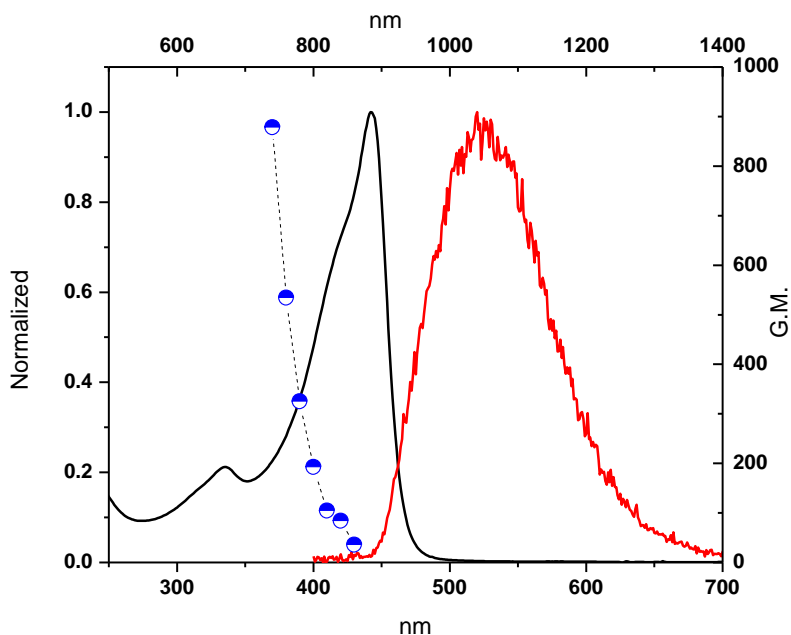


**Figure S-2.** Linear and two-photon photophysical properties of PPESO<sub>3</sub> ( $c = 20 \mu\text{M}$ ) polymer in water. Normalized one-photon absorption spectrum (black line), normalized two-photon excited emission spectrum (red line), and 2PA absorption spectrum (black line and circle symbol). Note that the units on the right hand side y-axis are G.M. per polymer repeat unit.

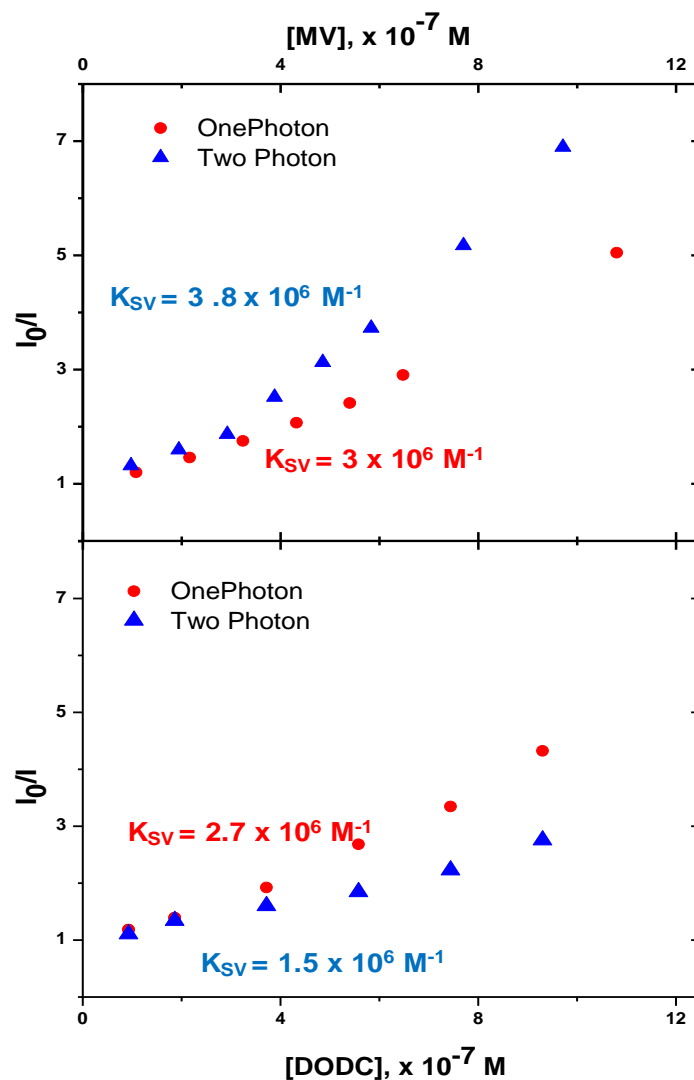


**Figure S-3:** Stern-Volmer (SV) plot for the fluorescence quenching of PPESO<sub>3</sub> (10  $\mu$ M in methanol) by DODC and MV<sup>2+</sup> under one-photon ( $\lambda_{\text{ex}} = 380$  nm) and two-photon ( $\lambda_{\text{ex}} = 740$  nm) conditions. (a) DODC [0.1 – 10  $\mu$ M] and (b) MV<sup>2+</sup> [0.1 – 10  $\mu$ M] as quenchers ( $K_{\text{SV}}$  was calculated at lower concentrations of quencher where the SV plot was a straight line).

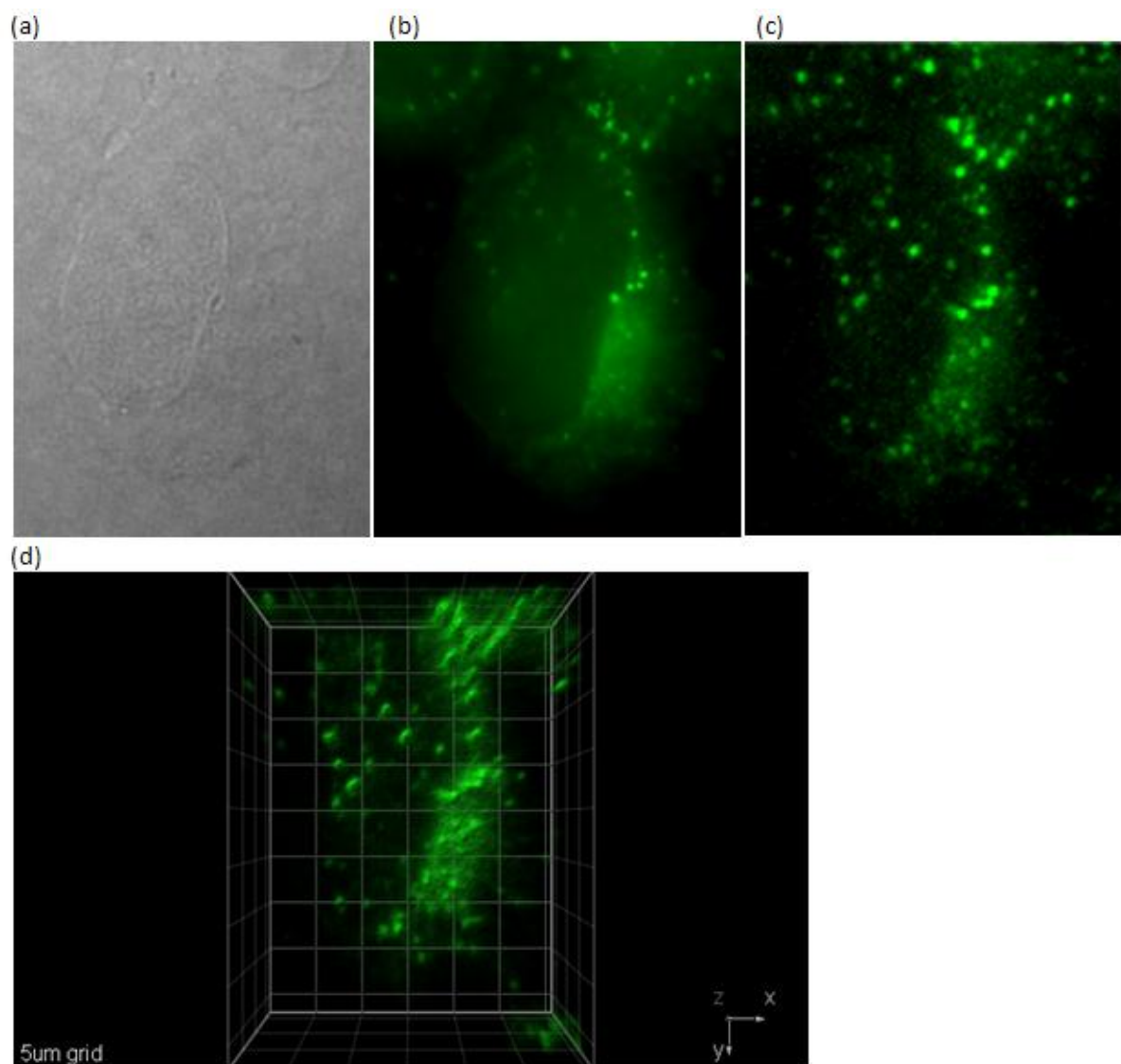


**Figure S-4.** Images of HeLa cells incubated with PPESO<sub>3</sub> polymer (5  $\mu$ M, 2 h). (a) DIC, exposure time 20 ms, (b) 1PFM image, 130 ms (filter cube Ex: 377/50 DM: 409 Em: 525/40), (c) one layer of 2PFM image (Ex: 750 nm; Power: 30mW), and (d) 3D reconstruction from overlaid 2PFM images (5  $\mu$ m grid).

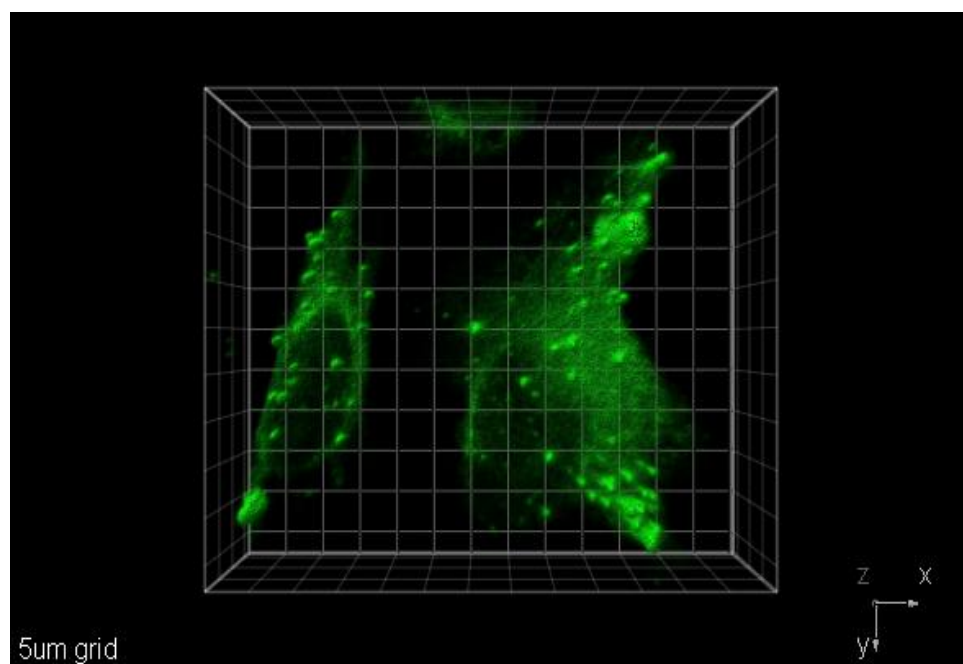


**Figure S-5.** 3D reconstruction from overlaid 2PFM images (5  $\mu\text{m}$  grid) of HeLa cells incubated with PPESO<sub>3</sub> silica nanoparticle (20  $\mu\text{g/mL}$ , 2 h).

## **APPENDIX E: SUPPORTING INFORMATION OF CHAPTER 5**

### ***1. Linear dependence of absorption max of TSPP in water***

The steady state absorption spectra of commercially available TSPP in water were shown in Figure 14. The high concentration of TSPP stock solution ( $\sim 4 \times 10^{-4}$  M) was spiked in 2 mL of ultrapure water ( $\sim 1 \times 10^{-5}$  M). TSPP in neutral aqueous condition was not showing the aggregation due to the linear dependence of absorbance. The reason is that TPPS remains as a monomeric free base form considering the electrostatic anionic repulsion from the sulfonate group.

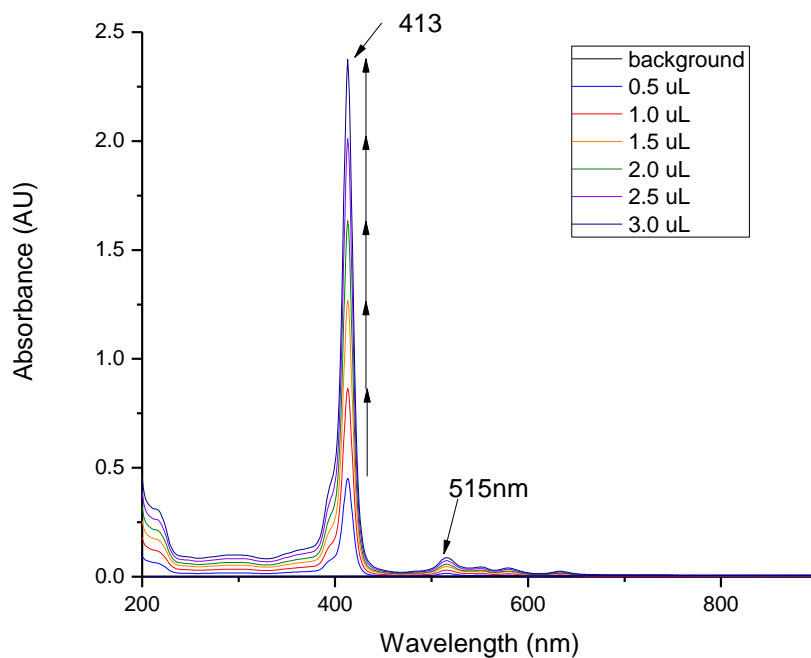


**Figure S1.** UV-Vis. absorption spectra of TSPP in water.

## 2. Molecular weight measurement

The molecular weight of the polymer was estimated by comparison of its diffusion coefficient with the diffusion coefficients of three polyethylene glycol standards. At dilute concentrations, the molecular weight of a polymer relates to its diffusion coefficient following equation 1.

$$D = kM^{-\nu} \quad (1)$$

The diffusion coefficients were measured using pulsed field gradient NMR. The experiments were performed on a Varian NMR Systems 500MHz spectrometer using the DgcsteSL\_cc (DOSY gradient compensated stimulated echo with spin lock and convection compensation) pulse sequence. The temperature was regulated at 25 °C and each sample was given a minimum of 30 minutes to equilibrate before acquiring. The gradient pulses,  $g$ , were applied for 2 ms and were arrayed in ten steps of equally spaced  $g^2$  over a range of 1.87 – 46.85 Gauss/cm (equivalent to 1000 – 25000 DAC units). The number of transients per increment was 16 for the PEG standards, and 200 for the polymer. Experiments were done in triplicate at five different diffusion times,  $t_{diff}$ , for each sample (Table 1). The calculation of  $D$  was performed by the acquisition software (VNMRJ 2.2C) using peak height. The peak at 3.61 ppm (referenced to internal  $CDCl_3$ ) was used for the PEG samples, and peaks at 1.60 and 1.37 ppm were used for the polymer.

**Table 1.** Diffusion coefficients for polymer and PEG standards.

	polymer peak 1		polymer peak 2		PEG 7100		PEG 12600		PEG 22000	
$t_{\text{diff}}$ (ms)	$D \times 10^{12}$ (m <sup>2</sup> /s)	error	$D \times 10^{12}$ (m <sup>2</sup> /s)	error	$D \times 10^{12}$ (m <sup>2</sup> /s)	error	$D \times 10^{12}$ (m <sup>2</sup> /s)	error	$D \times 10^{12}$ (m <sup>2</sup> /s)	error
100	2.462	0.025	2.371	0.046	1.122	0.009	0.641	0.004	0.343	0.002
	2.456	0.135	2.344	0.117	1.122	0.002	0.646	0.002	0.349	0.002
	2.494	0.111	2.429	0.131	1.124	0.002	0.640	0.003	0.342	0.001
200	2.260	0.184	2.098	0.189	1.111	0.002	0.632	0.002	0.339	0.001
	2.273	0.171	2.175	0.169	1.111	0.002	0.630	0.002	0.341	0.001
	2.379	0.171	2.328	0.201	1.112	0.001	0.628	0.002	0.340	0.001
300	2.354	0.215	2.178	0.208	1.107	0.002	0.626	0.002	0.334	0.001
	2.471	0.240	2.291	0.231	1.106	0.002	0.625	0.002	0.333	0.002
	2.367	0.196	2.367	0.244	1.114	0.001	0.628	0.001	0.342	0.004
400	2.479	0.209	2.379	0.244	1.105	0.002	0.623	0.002	0.329	0.002
	2.764	0.295	2.382	0.262	1.108	0.002	0.560	0.023	0.331	0.001
	2.478	0.244	2.721	0.298	1.108	0.001	0.624	0.001	0.336	0.003
500	2.561	0.260	2.517	0.262	1.106	0.003	0.686	0.028	0.318	0.002
	2.843	0.297	2.638	0.279	1.108	0.003	0.685	0.028	0.321	0.002
	2.887	0.265	2.814	0.263	1.105	0.002	0.618	0.002	0.326	0.002

A least-square regression of eq. 1 for the average values of the three PEG standards yielded  $k = 13627$  and  $\square = 1.06$ . These values and the average value of  $D$  for the two polymer peaks were plugged into eq.1 yielding a molecular weight of 3411 for the polymer (Table 2).

**Table 2.** Calculation results using the three PEG standards.

M	D <sub>meas</sub>	D <sub>calc</sub>	M <sub>calc</sub>
7100	1.111	1.127	7197
12600	0.633	0.614	12244
22000	0.335	0.34	22307
polymer	2.452		3411

The acknowledged flaw in the molecular weight estimation is in the fact that the three standard measurements were all less than the polymer diffusion coefficient.

## **APPENDIX F: SUPPORTING INFORMATION OF CHAPTER 6**

### 1. Height-height correlation functions

Standard deviations of the measured height variations are  $4.4 \pm 0.5$  nm for clean nanotubes,  $2.0 \pm 0.4$  nm for dye molecules on quartz, and  $8.8 \pm 1.6$  nm for dye molecules on nanotubes in images measuring  $5 \times 5 \mu\text{m}^2$ . Correlation lengths, determined as shown in Fig. 4, are 45 nm for as-grown nanotubes, 65 nm for dye molecules on quartz, and 133 nm for dye molecules on nanotubes. Since the correlation length is proportional to sizes of clusters or grains [1], we conclude that the presence of nanotubes enhances the size of aggregates by 104 % and this enlargement of aggregates leads to the observed enhancement of optical absorptivity at the H-band.

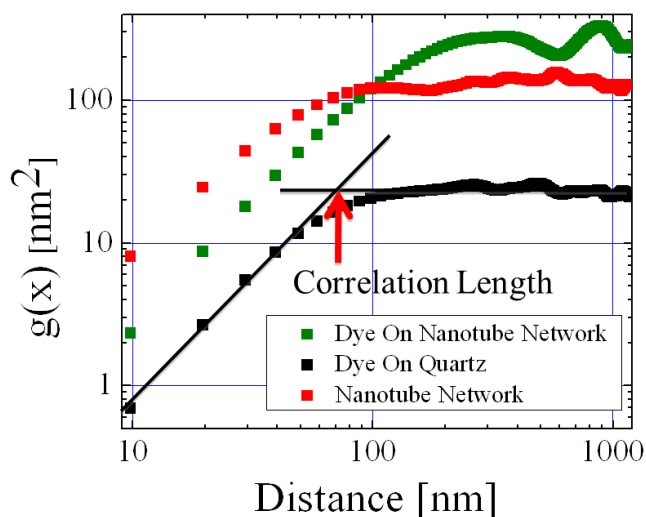


**Figure S 1.** Height-height correlation functions calculated from averaging three  $5 \mu\text{m}$  (with 512 pixels) line scans from AFM images. Interpolations shown for dye molecules on quartz show how the correlation length was determined.

## ***2. Comparison of the optical***

Figure S2. (a) and (b) compare the optical response of bare and aggregate-functionalized nanotube network devices. Only small optical response is observed for bare nanotubes: this response is not correlated with wavelength of the incoming light and is due to the voltage-induced stress by the applied gate voltage [2]. Dye molecules dope nanotubes upon functionalization as shown in Fig. 5b, making the threshold voltage higher than 35 volts for aggregate-functionalized devices. In response to light, the transfer curve shifts to even more positive values due to optical gating [3, 4]. The wavelength-dependent response of the device to light resembles the optical absorption spectrum as shown in (c). Assuming the optical response to be linear with the intensity of the incoming light, we estimate that the device is sensitive down to  $20 \mu\text{W}/\text{cm}^2$  from 620 to 760 nm with 25 volt applied to the gate electrode (using the observed noise of 1% in conductance). The observed photosensitivity is better than previous dye monomer- [5] or photoactive polymer-sensitized [6] devices by nearly an order of magnitude. Noise equivalent power of our prototype device is  $15 \mu\text{W}$  and normalized detectivity is  $10^7 \text{ cm Hz}^{1/2} \text{ W}^{-1}$ , assuming the noise bandwidth of 10 kHz. Orders of magnitude improvement of these figures of merit should be possible by using individual nanotubes with field effect mobility reaching  $100,000 \text{ cm}^2/\text{V sec}$  [7] and by improving the coupling between aggregates and nanotubes.

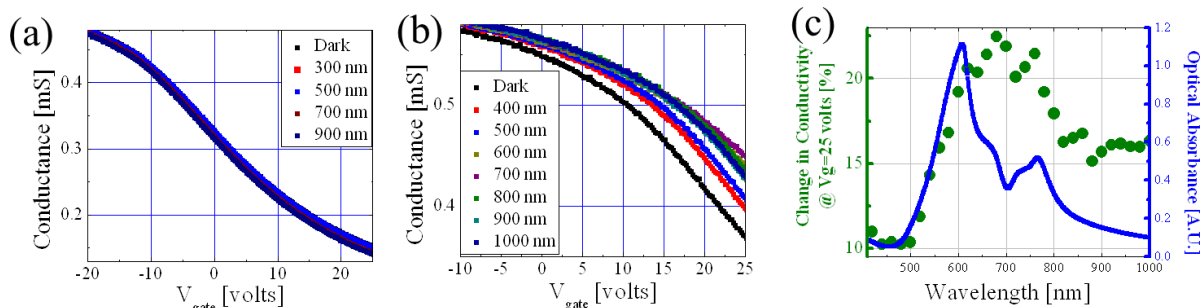


**Figure S2.** (a) Device transfer curve (conductance vs. gate voltage) for nanotube network field effect transistors in dark and in light. (b) Device transfer curve (conductance vs. gate voltage) for nanotube field effect transistors functionalized with SQ44OH in dark and in light. (c) Device response versus wavelength is compared to the absorption spectrum of SQ44OH on nanotubes. As optical spectroscopy requires a transparent substrate, the absorption and photoconductivity measurements were acquired on different dye films, delivered to nanotubes using the same spin-coating parameters.

1. K. Vanormelingen, B. Degroote, and A. Vantomme, *Quantitative characterization of the surface morphology using a height difference correlation function*. Journal of Vacuum Science & Technology B, **24**(2): p. 725-729,(2006).
2. M.S. Fuhrer, B.M. Kim, T. Durkop, and T. Brintlinger, *High-mobility nanotube transistor memory*. Nano letters, **2**(7): p. 755-759,(2002).

3. Y.M. Shi, H. Tintang, C.W. Lee, C.H. Weng, X.C. Dong, L.J. Li, and P. Chen, *Effects of substrates on photocurrents from photosensitive polymer coated carbon nanotube networks*. Applied Physics Letters, **92**(10),(2008).
4. D.S. Hecht, R.J.A. Ramirez, M. Briman, E. Artukovic, K.S. Chichak, J.F. Stoddart, and G. Gruner, *Bioinspired detection of light using a porphyrin-sensitized single-wall nanotube field effect transistor*. Nano letters, **6**(9): p. 2031-2036,(2006).
5. A. Star, Y. Lu, K. Bradley, and G. Gruner, *Nanotube optoelectronic memory devices*. Nano letters, **4**(9): p. 1587-1591,(2004).
6. Y.M. Shi, X.C. Dong, H. Tintang, C.H. Weng, F.M. Chen, C.W. Lee, K.K. Zhang, Y. Chen, J.L. Wang, and L.J. Li, *Photoconductivity from Carbon Nanotube Transistors Activated by Photosensitive Polymers*. Journal of Physical Chemistry C, **112**(46): p. 18201-18206,(2008).
7. T. Durkop, S.A. Getty, E. Cobas, and M.S. Fuhrer, *Extraordinary mobility in semiconducting carbon nanotubes*. Nano letters, **4**(1): p. 35-39,(2004).